THE CORNELL HIGH-ORDER ADAPTIVE OPTICS SURVEY FOR BROWN DWARF COMPANIONS AND RELATED INSTRUMENTATION STUDIES FOR BROWN DWARF RESEARCH

A Dissertation

Presented to the Faculty of the Graduate School

of Cornell University

in Partial Fulfillment of the Requirements for the Degree of

Doctor of Philosophy

by

Joseph Coler Carson

January 2005

THE CORNELL HIGH-ORDER ADAPTIVE OPTICS SURVEY FOR BROWN DWARF COMPANIONS AND RELATED INSTRUMENTATION STUDIES FOR BROWN DWARF RESEARCH

Joseph Coler Carson, Ph.D.

Cornell University 2005

I begin this publication with a description of the procedures and results for the Cornell High-order Adaptive Optics Survey (CHAOS) for brown dwarf companions to stellar systems. This survey consisted of near-infrared coronagraphic observations of 80 stars out to 22 parsecs. The subsequent data analysis revealed that zero systems showed conclusive evidence for a brown dwarf companion. Accompanying Monte Carlo population simulations determined a brown dwarf companion upper limit of 9.7% for the 25-100 AU semi-major axis region. Such a value indicates, at an 89% confidence level, that the "brown dwarf desert" around stellar objects extends further than has been previously reported.

Following my descriptions of the CHAOS survey, I continue with a discussion of HD150451C, a likely white dwarf companion to the binary system HD150451AB. This object, discovered in the course of the CHAOS survey, shows infrared colors and H-band spectra consistent with a white dwarf. Common proper motion measurements confirm its classification as a physical companion. A mass estimate of

0.6-1.3 $M_{\odot}$ constrains it among the population of medium to very large (i.e. approaching the Chandrasekhar mass) white dwarf stars. We discuss the implications of such a classification for the stellar system's origins and history.

I conclude with a description of my work in the design, fabrication, and commissioning of WIRC, a state of the art wide-field infrared camera for the Palomar 200-inch Hale telescope. The instrument, along with the collecting power of the Palomar 200-inch Hale telescope, is currently the most powerful system in the world for wide-field infrared surveys. It presently resides at Palomar Observatory as a full-time facility instrument.

BIOGRAPHICAL SKETCH

I was born in San Diego, California on July 25, 1977. I am the third child in a family of six. I grew up happily with my two older sisters, Rebecca and Dora, my younger brother Benjamin, and my parents, Dennis and Sandra. My father, Dennis, taught me a love for science, books, and the pursuit of knowledge. My mother Sandra taught me a love for art and to always be patient with people. I attended a Jewish day school through junior high and played every sport I could find. Through high school I played a great deal of soccer and got tan on the San Diego beaches and surf. At the same time I began a close friendship with my high school classmate, Nicolle Robinson, who I fell in love with and married ten years later.

I left San Diego in the Fall of 1995 to attend Pomona College, just outside of Los Angeles. I majored in physics and planned to work as an engineer someday. In the Fall of 1997, I spent a semester at the University of Edinburgh in Scotland, one of the most beautiful places I have ever visited. The following summer I worked in an astronomy internship at Harvey Mudd College with Professor Alex Rudolph, who became a strong mentor for me. I had always been mesmerized staring at the stars, but never before imagined it as a career path. At the end of the summer I decided that I would apply to astronomy and astrophysics graduate programs. Several months later I accepted an offer to join the astronomy PhD program at

Cornell University. I packed my belongings and drove to Ithaca, New York. There I studied and gained many friendships with people who settled there from all over the globe. Shortly after settling there, I began conducting research with Professor Stephen Eikenberry. I view my choice to work with Professor Eikenberry as one of the best decisions of my professional career. In particular I learned from him how to be fearless in research and to always keep a broad vision. Later on, I also came to value him strongly as a friend who is direct, passionate, and wears his heart on his sleeve.

The ultimate best decision of my time in graduate school was my engagement to Nicolle. We married August, 2003 in San Diego, California.

To all of my teachers.

ACKNOWLEDGEMENTS

During my graduate career, I had the fortunate experience of learning from a diverse array of people. I cannot possibly list everyone right here, but I hope to mention a few people to whom I am especially thankful.

First and foremost, I thank my thesis advisor Steve Eikenberry who helped guide me these last five years and provided me with opportunities to work in instrumentation, observation, and theoretical modeling. While mentoring me as I waded into foreign waters, he also gave me the freedom and independence to choose my own directions. He taught me to be fearless and ambitious in research, and capture opportunity wherever it may arise.

I also thank many other people who helped me through my graduate career. In particular, the second floor faculty and staff were always very patient and helpful when I would wander into their offices or labs to ask for help or advice. I thank Chuck Henderson for navigating me through Mechanical Desktop and teaching me the secrets of "junkyard engineering". I thank John Wilson for his advice and guidance in infrared instrumentation and graduate academia in general. I thank Don Barry for his care and tenderson toward my computer and for providing our lab with lively political discussion. I thank Bernhard Brandl for being patient with me as I hung around his office seeking scientific advice. I am thankful to Bruce Pirger

for his guidance in electronics and for teaching me about the dangers of the "magic smoke". I also thank Sarah and James Higdon who were kind enough to use part of their own awarded Palomar observing time to collect last-minute observational data for me. Finally, I thank all of the other engineers and faculty who helped guide me through pitfalls and challenges.

I am immensely indebted to the talented Cornell graduate students with whom I interacted over the years. Arriving from all over the world, they enriched my graduate life both socially and academically; I thank my labmates Dae-Sik Moon and David Rothstein for providing excellent company and fine words of wisdom. I also owe thanks to Matija Cúk, Karen Masters, Nick Mathew, Tom Lorusso, and Rich Belfield for countless insightfull conversations and many innane ones as well. I doubt that I would have survived four years of Ithaca without them. At the University of Florida, I thank all of my officemates, including Michelle Edwards, Dave Clark, Mike Barker, Ashley Espy, Iley Vass, Margaret Moerchen and all of the other UF people for making me feel so welcome in Gainesville.

I thank my thesis committee for trusting me to handle an ambitious thesis project while working toward a minor in both physics and english literature. In particular, I thank James Houck for agreeing to head my thesis committee following Steve Eikenberry's move to the University of Florida. Outside of my committee, I thank James Cordes for providing advice and guidance in the population modeling aspects of my thesis.

I am of course indebted to all of the Palomar Observatory staff who offered guidance and provided company to me through scores of observing nights. I am especially thankful to Jean Mueller, Karl Dunscombe, and Rick Burress, who helped me navigate through the challenges of adaptive optics observing. At JPL, I thank

Mitch Troy for using his observing time to take observations for me. I also thank him for guiding me through my first adaptive optics observing run when, at the last minute, my advisor was unable to make the trip. At CalTech I thank Keith Matthews for taking time from his allotted observing nights to take observations for me.

Additionally, I thank my undergraduate thesis advisor, Alex Rudolph, for peaking my interest in astronomy studies. Without his advice and guidance, I doubt that I would have advanced so far.

But most of all, I am indebted to the support of my wife Nicolle as well as my parents and siblings. Nicolle gave me the confidence and support to withstand cold winters and sometimes colder publication referees. My family instilled in me the importance of pursuing knowledge and wisdom. To all of these people, and many others that I failed to mention, I am forever greatful.

TABLE OF CONTENTS

LIST OF TABLES

LIST OF FIGURES

Chapter 1

Introduction

This thesis reports the results of the CHAOS coronagraphic Adaptive Optics survey for brown dwarf companions 25-100 AU from nearby stars. Detecting zero systems with positive evidence of brown dwarf companions, we find, at a high confidence level, that the "brown dwarf desert" extends to further orbital separations than has previously been reported (Marcy & Butler 2000). Our associated Monte Carlo population simulations evaluate a brown dwarf companion upper limit of 9.7%. Along with these results, we present the discovery of a probable white dwarf companion to the binary system HD150451AB. Finally, I describe my involvement in the design, fabrication, and commissioning of WIRC, a state of the art wide-field infrared camera for the Palomar 200-inch Hale Telescope.

1.1 What is a Brown Dwarf?

What exactly is a brown dwarf? In simplest terms, a brown dwarf is an object that is more massive than a planet and less massive than a star. If we are looking for a more rigorous definition, we may choose to rely on one of the following descriptions:

A brown dwarf is a non-nuclear burning object (at least no sustained nuclear burning) which, unlike a planet, forms from the gravitational self-collapse of a cloud, as opposed to forming in a circumstellar disk. Or instead, we might use the definition that a brown dwarf is a non-nuclear burning object which, unlike a planet, has the ability to fuse deuterium. These different definitions coincide closely as far as evolutionary tracks are concerned, but they illustrate the persistent difficulties in defining strict boundaries for these objects. One of the purposes therefore of this Ph.D. thesis is to help provide more rigorous constraints to brown dwarf classifications. Population analyses such as the brown dwarf companion study presented here are powerful tools in this endeavor because they connect brown dwarf characteristics with stellar and planetary origin and evolution. For instance, they may answer the question, "do brown dwarf companions exist with the same frequency as hydrogen-burning M-dwarf companions?" If not, then it is likely that a specific characteristic of brown dwarfs must dictate these strict evolutionary tracks. Does mass alone dictate this frequency? Is there a more complicated relationship that depends on composition or primary star spectral type? The survey described in the following pages does not answer all of these questions. However, by providing astronomers with a thorough census of the consequences of evolutionary processes (i.e. population statistics), it gives us the tools to better understand what exactly we imply when we term an object a brown dwarf.

1.2 Brown Dwarf Origins

As stated in the previous section, definitions of brown dwarfs closely associate with the evolutionary tracks of these objects: Brown dwarfs form from self gravity; Planets form in circumstellar disks; Brown dwarfs burn deuterium; Planets do not. On

the more specific level however, these criterion may not coincide. Low and Lynden-Bell (1976), for instance, determine that the minimum mass necessary for a cloud to self-collapse may be as low as 7 Jupiter masses. They contrast this value with the estimated deuterium burning mass minimum of 13 Jupiter masses. In a more extreme case, Boss (2001) argues that, when magnetic field tensions play an important role, cloud masses as low as 1 Jupiter mass may be able to self-gravitate.

Reipurth and Clarke (2001) propose that, rather than developing from simple self-collapse, brown dwarfs may actually be stellar embryos ejected from newborn multiple systems. In this scenario, the system member that forms the slowest would be ejected through gravitational interaction with the other members. While some simulations support this scenario (Bate, Bonnell & Bromm 2002), the presence of known brown dwarf binaries (Martín et al. 2003, for instance) may be inconsistent with such evolutionary paths. Brown dwarf pairs, especially ones with larger separations, would likely be torn apart in such environments.

Connecting brown dwarfs with traditional sun-like evolutionary tracks, some groups (Liu et al. 2003, for instance) have discovered signs of circumstellar disks around many young brown dwarfs. As a further connection, high-resolution optical spectroscopic studies (Jayawardhana, Mohanty, & Basri 2002; Jayawardhana, Mohanty,& Basri 2003; Muzerolle et al. 2003) have shown evidence for gas flow from the inner disk onto the brown dwarf surfaces. The timescales for this gas flow is consistent with timescales of young sun-like stars, strengthening their similarities with sun-like evolutionary paths.

Overall, astronomers have leaned toward solar-like formation processes for brown dwarfs: Brown dwarfs form through traditional gravitational self collapse, not more complicated ejection scenarios. They also may form in binary pairs and with cir-

cumstellar disks, characteristics more consistent with traditional gravitational self collapse. Despite these leanings, a more complete census of brown dwarf populations is necessary before either scenario can be ruled out.

1.3 Brown Dwarf Interiors

To summarize the interior physics of brown dwarfs, we begin at the original formation from cool molecular clouds. This historical approach helps us define interior physics partly by illustrating where interior properties deviate from their higher mass stellar cousins. Barring a more exotic formation scenario (e.g. brown dwarf formation and ejection from inside a circumstellar disk), brown dwarfs and stars begin their formations as a dense pocket of cloud fragments and contracts adiabatically into a protostellar mass (see Shu, Adams, & Lizano, 1987 for a more complete discussion). Compressing with a roughly constant effective temperature, the core temperature and density increase, scaling roughly with the inverse of the object radius (Stahler, 1988). For objects destined to become stars (eventual masses $\gtrsim 0.1$ $M_{\odot}$ [Burrows & Liebert 1993]), core temperatures and pressures reach high enough levels for pp-I fusion to begin. This fusion coincides with an ignition temperature $\sim 3 \times 10^6$ Kelvin (Burrows & Liebert, 1993). Soon after this ignition, the hydrogen fusion delivers a pressure high enough to halt further contraction. The star thus begins its Main Sequence lifetime. For brown dwarfs, however, a different scenario occurs. Since the contracting protostellar masses are smaller, the core temperatures and pressures increase more slowly. One result of this is that higher densities are required to reach ignition temperatures (see review in Burgasser, 2002). The core pressure therefore increases until electron degeneracy pressure halts contraction and hydrostatic equilibrium commences. The pressure regime for these electron-pressure

dominated objects is believed to range from $\sim$ 10 to 1000 gm/cm^3 (Burrows & Liebert, 1993). Acknowledging that these objects are virtually entirely convective, except for a thin outer radiative layer, we may model the internal pressure via the polytropic relationship:

$$P = K'\rho^{1+1/n} \tag{1.1}$$

where we set the traditional polytropic index n to a value of 1.5 (Burrows & Liebert, 1993). In this equation, P is the pressure, ρ is the mass density, and K' is a constant depending on composition and specific entropy. The specific composition will depend on the particular object, but metallic hydrogen and helium will form the main constituents (Burrows & Liebert, 1993). Combining the previous polytropic equation with the general equation for hydrostatic equilibrium,

$$\frac{dP}{dR} = \frac{GM(r)\rho}{r^2} \tag{1.2}$$

can be found to yield the following results for radius, central density, and central pressure. (See Burrows & Liebert, 1993 for a more complete derivation.)

$$R = \sqrt{\frac{\pi}{2}} \left(\frac{K'}{G}\right)^{\frac{n}{3-n}} M^{\frac{1-n}{3-n}} \tag{1.3}$$

$$\rho_{cent} \propto M^{\frac{2n}{3-n}} \tag{1.4}$$

$$P_{cent} \propto M^{\frac{2(1+n)}{3-n}} \tag{1.5}$$

In equations 1.2 through 1.5, P is the pressure, R is the object's total radius, G is the gravitational constant, r is a variable radius, ρ is density, K' is the same as in equation 1.1, M is the mass of the object, and n is the polytropic index,

1.4 Brown Dwarf Atmospheres

To first order, when we observe brown dwarfs, we observe their atmospheres. Thus, any brown dwarf observational program which hopes to decipher underlying physics must take advantage of the most advanced knowledge of the atmospheric physics of these objects. Giving far-reaching descriptions of brown dwarf atmospheres can be complicated since striking differences occur across the brown dwarf regime. For the purposes of clarity, I will divide my discussion into two categories of brown dwarfs, the L subtype and the T subtype. I begin with a discussion of L-dwarfs.

1.4.1 L-Dwarf Atmospheres

As a general rule, we may define L-dwarf atmospheres as ones which are cool enough to possess Lithium, unlike most warmer M-stars, and warm enough that the vast majority of their atmospheric carbon is locked in CO rather than CH_4.[1] Figure 1.1 (Kirkpatrick et al. 1999) displays the notable Lithium absorption line in L-dwarf spectral types ranging from L1 V to L8 V. The presence of this line was one of the earliest tools used to identify brown dwarf candidates (Basri, Marcy, & Graham, 1996). The majority of L-dwarf flux, though, emits in the 1-2.5 μm range. Figure 1.2 displays this rich portion as well as the long-optical region, comparing a late M, early L, and late L dwarf (Kirkpatrick et al. 1999). One strong change as we move from M-dwarf to L-dwarf atmospheres is the weakening of the TiO and VO bands[2]. The weakening of these features is accompanied by the strengthening of

[1] While this is a useful guideline, there are some noticeable exceptions. For instance, Noll et al. (2000) have have found evidence of the 3.3 μm CH_4 band in the latest-type L dwarfs. Lithium has also been seen in nuclear-burning stars, often associating with a very young age and/or unusually high chromospheric activity. See Zboril, Byrne, & Rolleston (1997) for a more complete discussion.

[2] VO actually strengthens slightly in the earliest subtypes, but quickly weakens toward later subtypes (Burgasser, 2002)

CrH and FeH as well as resonance lines such as K I, Rb I, and Cs I. Towards the latest L-dwarfs, the CrH and FeH bands weaken while the H_2O bands strengthen. Astronomers combine observational spectra such those in Figure 1.2 with theoretical models to derive characteristics such as composition and temperature. Fegley & Lodders (1996) chemical equilibrium calculations determine that the most abundant molecules in these atmospheres include H_2, H_2O, CO, N_2, and H_2S. The metal oxides that are spectrally active in M dwarf atmospheres, such as VO and TiO, have been replaced in these cooler atmospheres by condensible types (Fe, VO, $CaTiO_3$, for example) and hydrides like FeH, CrH, CaH, and MgH (as described in Burgasser, 2002). With regards to temperature, Leggett et al. (2001) use models by Chabrier et al. (2000) to estimate an L-dwarf temperature regime of 2200-1400 K.

Another defining characteristic of L-dwarf atmospheres is the believed existence of a dusty atmosphere. Theoretical models by Allard et al. (1996) show that L-dwarf spectra and colors are most consistent with atmospheres where dust particles such as corundum (Al_2O_3), iron (Fe), and enstatite ($MgSiO_3$) distribute throughout the atmosphere. At the brown dwarf/low mass star boundary though, these objects appear less and less like a grey body, showing more molecular absorption features. This suggests that dust particles are able to condense more easily as we move from the low mass star regime to the cooler brown dwarf regime (see figures 1.3 and 1.4). Moving further along the spectra to cooler and cooler temperatures, observers begin to see evidence of another strong transformation in atmospheric characteristics, the beginning of atmospheric methane formation. This transformation, described below, heralds the the T-dwarf classification.

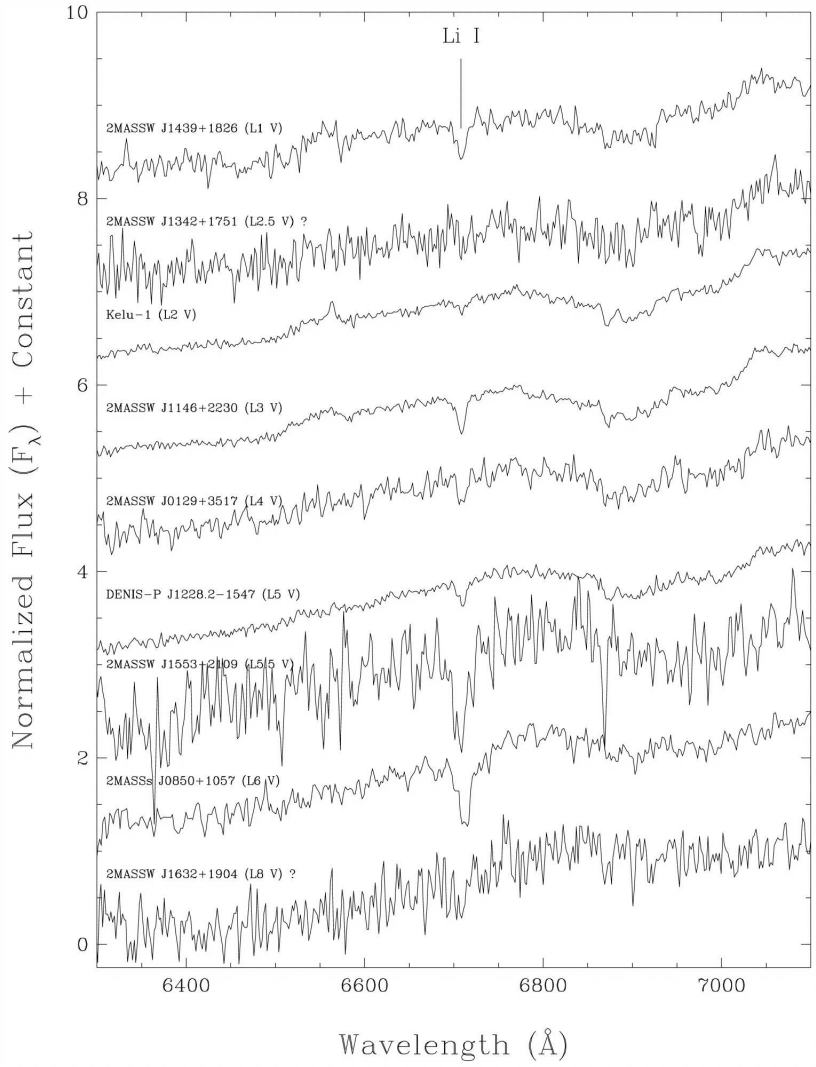

Figure 1.1: Kirkpatrick et al. (1999) L dwarf spectra illustrating the 6708 $\AA$ Li line. The image was reproduced with permission from J. Kirkpatrick.

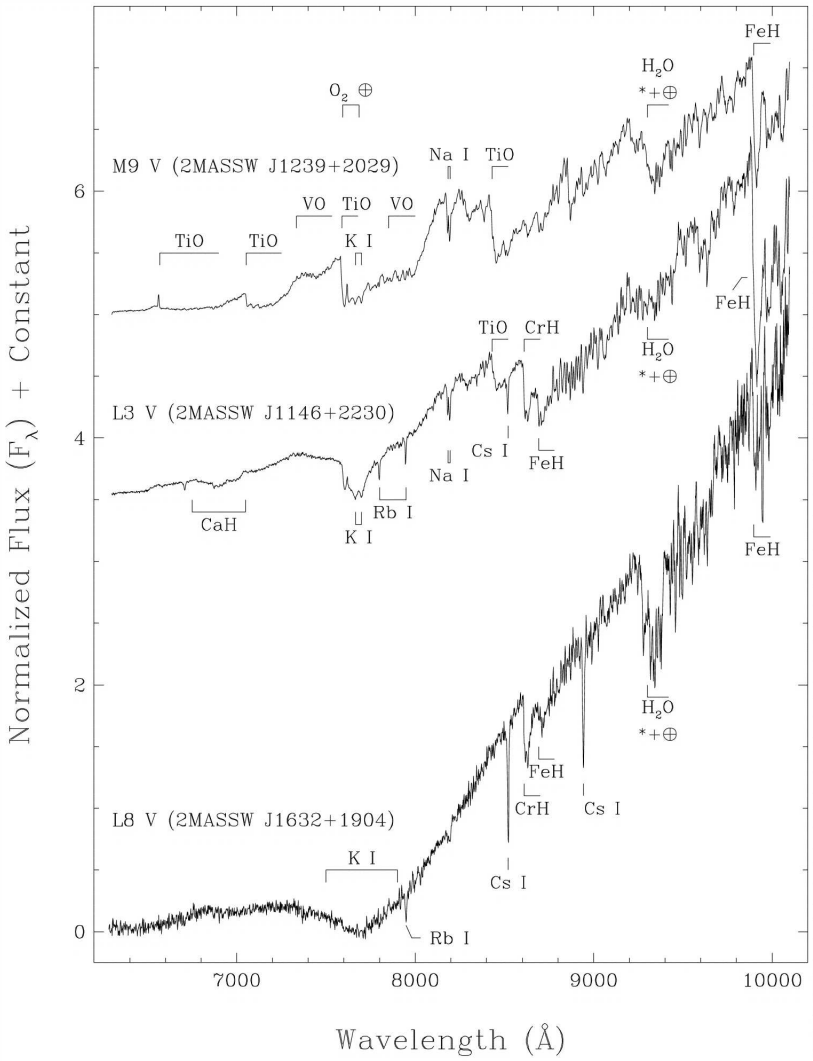

Figure 1.2: Kirkpatrick et al. (1999) spectra of a late-M, early-L, and late-L dwarf, covering the 6300-10100 $\AA$ region. Reproduced here with permission from J. Kirkpatrick.

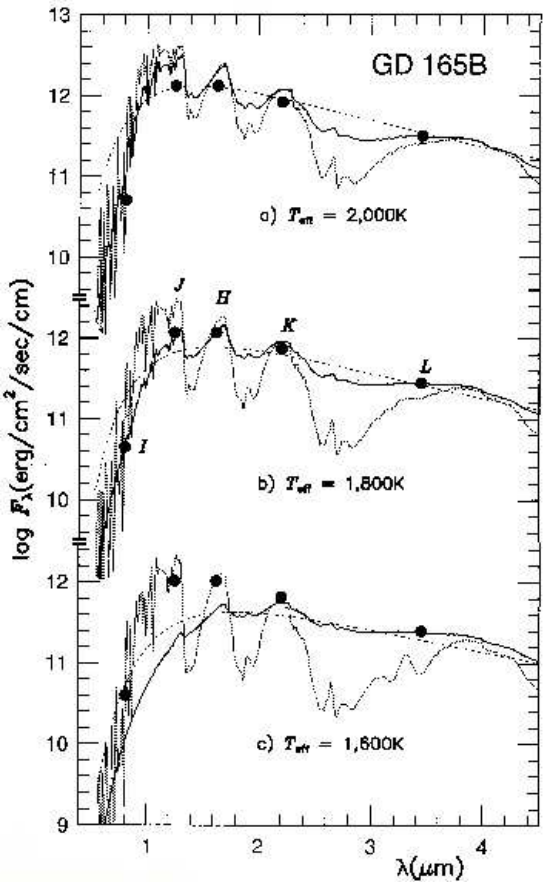

Figure 1.3: Tsuji et al. (1996) model spectra of brown dwarfs with T_{eff} = 2,000 (a), 1,800 (b), and 1,600 K (c). Solid lines represent dusty models. Dotted lines represent dust-free models. Smooth curves are blackbodies for $T = T_{eff}$ for each model. The spectra are compared with photometric fluxes (filled circles) from the L-dwarf GD 165B. The authors find that the L-dwarf fluxes agree best with a dusty atmosphere. The image was reproduced with permission from T. Tsuji.

1.4.2 T-Dwarf Atmospheres

As brown dwarfs cross the boundary from L to T, carbon changes from being locked in CO to forming into CH_4 molecules. Fegley & Lodders (1996) determine that this change occurs around 1300-1500 K. The resulting strong methane absorption lines, shown in Figure 1.4, provide the defining features of these $\lesssim$ 1300K brown dwarfs, also described as "methane" brown dwarfs. Another sharp change from L to T, as supported by Tsuji (2002) theoretical data and Burgasser et al. (2002b) observational data, is a rapid clearing of dust clouds as particulates may collect and sink to greater depths. Conversely, the lighter, more volatile molecules continue to remain homogenous in the upper atmosphere where they produce the strong absorption lines displayed in Figure 1.4. Continuing into the lower temperature regimes, Fegley & Lodders (1996) describe N_2 converting to NH_3 at 700 K and H_2O and NH_3 condensing out of the photosphere at about 350 K and 200 K respectively.

A clearcut understanding of T-dwarf atmospheres, and all brown dwarfs for that matter, is complicated by the known presence of atmospheric variability in these objects (Enoch, Brown, & Burgasser, 2003). Burgasser et al. (2002b) speculates that T-dwarf variability might result from the aforementioned clearing of dust clouds, especially around the T dwarf/L dwarf boundary. However, present statistical data (such as Enoch et al. 2003), though somewhat limited, have yet to confirm that premise. Tsuji & Nakajima (2003) theoretical models refute the Burgasser et al. (2002b) description of a rapid clearing of dust clouds and instead predict that this phenomenon results from the migration of a thin dust cloud from an optically thin to an optically thick layer of the atmosphere. For certain brown dwarf observations, the existence of phenomena such as star spots and weather patterns have been invoked as possible alternate explanations for variability (Allard et al. 1997). Even

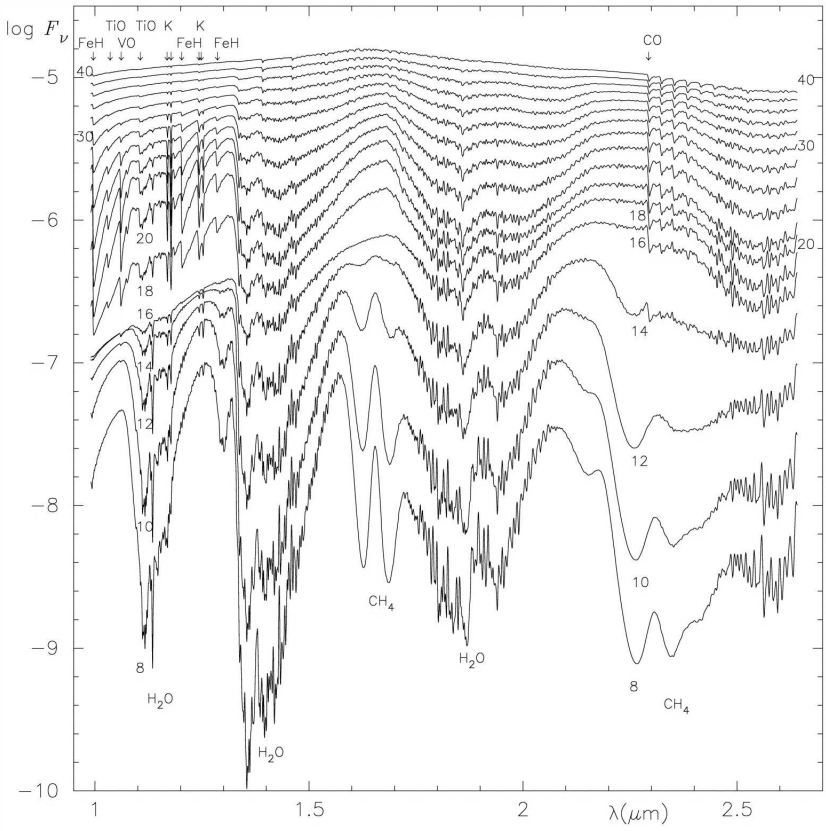

Figure 1.4: 1.0-2.6 μm spectra predicted by Tsuji (2002) for T_{eff} = 800-2600 K cloudy models and T_{eff} = 2800-4000K dust-free models. Each successive curve represents T_{eff} steps of 200 K. The numbers labeled on the curves represent temperatures in units of 100 K. This image was reproduced with permission from T. Tsuji.

further complications in our understanding of brown dwarf atmospheres include the presence of magnetic fields and deviations from thermodynamic equilibrium (Allard et al. 1997). As observers continue to discover and monitor a larger sample of brown dwarfs, theoretical models will be in better position derive more comprehensive descriptions.

1.5 Observational Identification of Brown Dwarfs

Here I provide a summary of a few prominent characteristics by which brown dwarfs may be identified.

1.5.1 Luminosity and Temperature

One of the most straightforward methods of distinguishing stars from brown dwarfs is the measurement of luminosity. Since stars, for the most part, maintain a constant luminosity through their main sequence lifetime, there is a minimum luminosity below which nuclear burning cannot sustain. Accordingly, objects of solar metallicity with luminosities below $\sim 10^{-4}\ L_{\odot}$ (Burrows et al. 2001) can be ruled out as main sequence stars. This tool is useful for brown dwarf companion searches such as CHAOS, where intrinsic luminosity can be derived given the known distances of the parent systems. As long as we can conclude that an object is a physical companion, via common proper motion[3] for instance, we may measure its luminosity to find if

[3]Common Proper Motion is a technique by which physical associations may be tested via astrometrical measurements taken over some length of time, typically several months for nearby objects. This technique takes advantage of the fact that nearby objects ($\lesssim 20$ parsecs for instance) tend to have high projected proper motions compared to background stars. Therefore, one may conduct astrometry of a parent system and candidate companion over several months and measure if they maintain a constant separation from each other. Candidate companions whose separations change significant amounts, say several arcseconds, can generally be deemed as non-associated field stars.

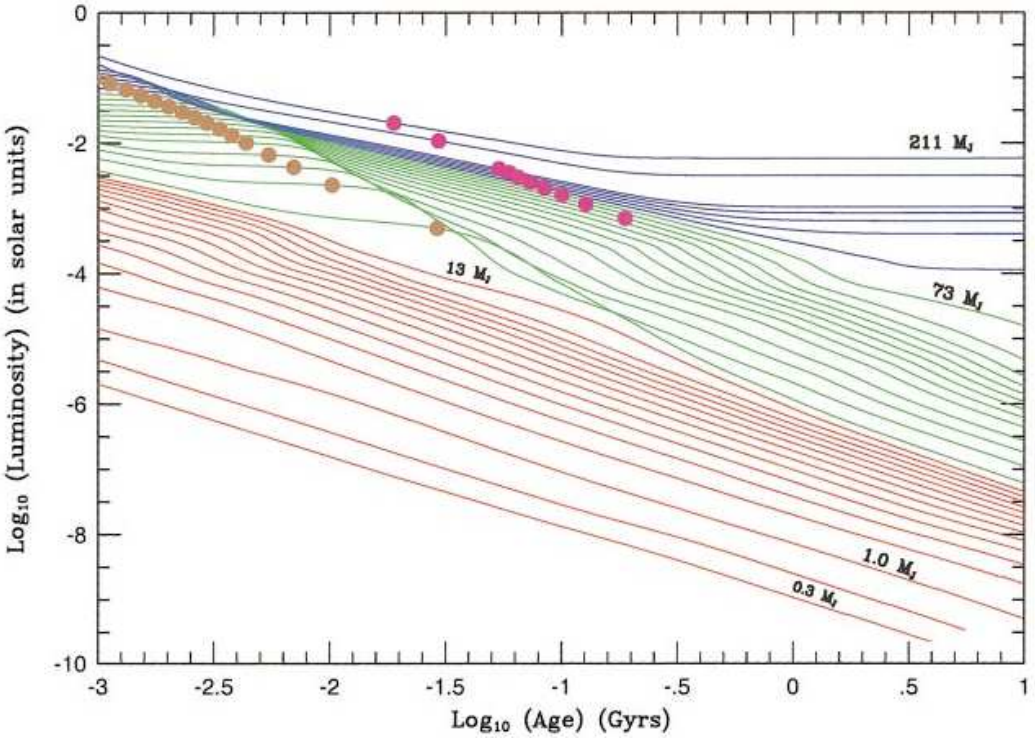

Figure 1.5: This plot from Burrows et al. (2001) describes the evolution in luminosity of isolated low-mass stars and substellar objects as a function of age. Blue curves represent stars; Green curves represent brown dwarfs; Red curves represent planets. The gold dots mark the points along the evolutionary tracks when 50% of the deuterium has burned. Magenta dots mark when 50% of lithium has burned. This image was reproduced with permission from A. Burrows.

we may rule out a stellar object.

While luminosity is a useful general guideline, there are many cases where it fails to provide a definitive identification. For example, an object of solar metallicity with a luminosity $> 10^{-4}\ L_{\odot}$ may still be consistent with a brown dwarf classification, depending on the age of the system. Figure 1.5 shows a plot of cooling curves predicted for a selection of stars, brown dwarfs, and planets. The plot demonstrates how, in many cases, we must have an estimate of a system's age before we can make a conclusive brown dwarf identification.

In the case where a system has no known distance to help determine a luminosity,

one may derive an effective temperature from spectral analysis. Spectral synthesis models such as those by Tsuji (2001) can generally constrain effective temperatures to better than 10%. Since radius is effectively constant for objects ranging from the largest brown dwarfs to Jupiter-sized planets (Burrows et al. 2001), we may then use the Stefan-Boltzman law to derive a luminosity, $L = 4\pi R^2 \sigma T_{eff}^4$. In this case, R is the brown dwarf radius (constant at $\sim$ 1 Jupiter radius), σ is the Stefan-Boltzman constant, and T_{eff} is the effective temperature. With the luminosity and temperature in hand, we can then often conclude a brown dwarf or stellar classification.

1.5.2 Molecular Absorption Features

In section 1.4 I described a range of absorption features unique to substellar objects. In particular, below $\sim$ 1500 K, CH_4 produces a number of absorption features easily observable in the 1 to 5 μm regime. Below $\sim$ 700 K, NH_3 forms along with a myriad of other molecules as we move to cooler and cooler temperatures (Burgasser 2002). Thus, a spectral snapshot of a brown dwarf candidate can often let us determine a brown dwarf or stellar classification as well as allow us to estimate a temperature.

Recently, astronomers have begun to take advantage of absorption features to identify T-dwarfs through narrow band photometry. In the case of methane band imaging, observers may identify atmospheric methane by taking narrow band photometry just on and off the 1.7 μm methane absorption window (Rosenthal, Gurwell, & Ho 1996). Figure 1.6 displays filter curves for methane filters installed in the Palomar 200-inch PHARO science camera (Hayward et al. 2001). A comparison with the underlying T dwarf spectrum shows that a flux reduction on order of 50% should

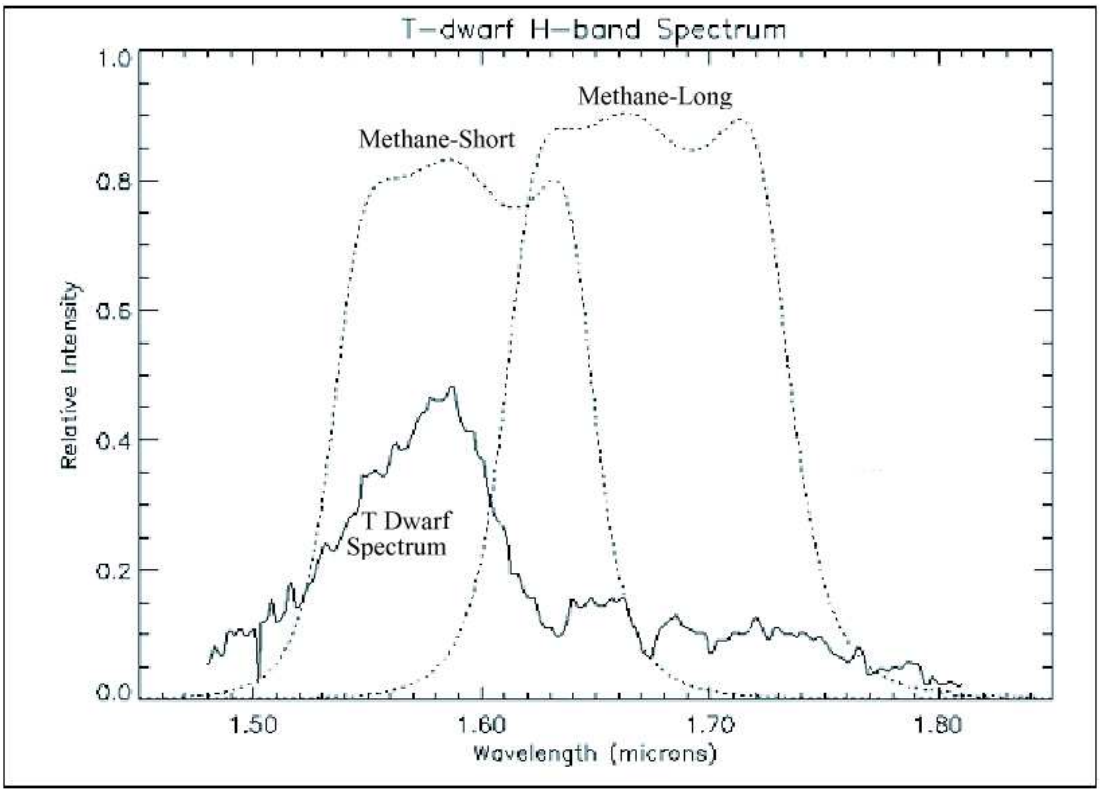

Figure 1.6: Methane filter transmission curves plotted over a late T-dwarf spectrum (Leggett et al. 2000). Our methane filters were fabricated by NDC Infrared Engineering and purchased through the MKO consortium (Simons & Tokunaga 2002; Tokunaga, Simons, & Vacca 2002). The Leggett et al. (2000) spectrum was reproduced with permission from S. Leggett.

be detected between the methane-short and methane-long bands.[4]

1.5.3 Lithium

As mentioned in section 1.4, brown dwarfs may also be identified through the existence of the lithium absorption line. This test, proposed by Rebolo et al. (1992), takes advantage of the fact that objects with nuclear burning destroy their initial lithium abundances while objects without nuclear burning retain them indefinitely.

[4]We had originally considered using such a technique for the entire CHAOS brown dwarf companion search. However, the late arrival of the filters ($\sim$ two years after our survey was underway) and the ineffectiveness of this technique to identify the warmer L dwarfs convinced us to instead conduct our search with a K_s filter.

As shown in Figure 1.5, low mass stars destroy their lithium within 300 million years, making the presence of lithium a good indicator of a brown dwarf classification in all but the youngest cases. An exception lies in the most massive brown dwarfs (> 0.065 $M_\odot$) which have some hydrogen fusion when they are young (< 250 Myrs) (D'Antona and Mazzitelli 1994). For the vast majority of scenarios though, the presence or absence of a lithium line makes an ample signature for classification.

1.5.4 Deuterium

In section 1.1, we distinguished brown dwarfs from planets through formation processes and the presence or lack of deuterium burning. While formation processes cannot be inferred directly, we may rely on the abundance of deuterium as as an observational dividing line between a planet and a brown dwarf. Since brown dwarfs are accepted to be fully convective, we expect that even in brown dwarf atmospheres, deuterium should have been removed. Therefore, an observer trying to distinguish a brown dwarf from a planet could look for deuterium absorption features. This could include HDO absorption features between 1.2 and 2.1 μm (Irwin et al. 1998) or various CH_3D features between 1 and 8 μm (Noll 1993, Krasnopolsky et al. 1997). Conclusive absence of these molecular components would provide strong evidence that deuterium burning had occurred, providing a brown dwarf classification. In contrast, deuterium abundances have been positively identified for several planets in our solar system (Krasnopolsky et al. 1997). The presence of deuterium therefore would mark a planetary classification for all but the youngest systems, where brown dwarfs could still be in the process of burning deuterium. (See Figure 1.5 for more information on deuterium burning timescales.)

1.6 History of Brown Dwarf Companion Imaging Searches

In table 1.1 I list brown dwarf companion searches conducted over the last twenty years or so. I omit brown dwarfs discovered through radial velocity and brown dwarfs discovered around other brown dwarfs. While this list may not be 100% complete (especially for some of the most recently begun unpublished surveys), it should provide a good idea of the different types of brown dwarf companion searches. Inspecting the list, one can see that the greatest number of successful discoveries have occurred at large projected separations (i.e. several hundred AU). These objects lend themselves to discoveries by all-sky surveys such as the Two Micron All-Sky Survey (2MASS; Skrutskie et al. 1997), Deep Near Infrared Survey (DENIS; Epchtein et al. 1997), and Sloan Digital Sky Survey (SDSS; Gunn and Weinberg 1995). Other than all-sky survey discoveries, we see a small handful of discoveries made at close separations to nearby stars. For a further review, please see Burgasser (2002), Basri (2000), and Oppenheimer, Kulkarni, & Stauffer (1999), as substantial portions of this list were compiled from their reviews.

Table 1.1: Direct Imaging Searches for Brown Dwarf Companions

Reference	Description	Results
Probst & O'Connell (1982)	NIR imaging of white dwarfs	0 detections
Probst (1983a,b)	NIR imaging of white dwarfs	0 detections
Jameson, Sherrington, & Giles (1983)	NIR imaging of nearby stars	0 detections
McCarthy, Probst, & Low (1985)	NIR speckle interferometry of nearby stars	False detection VB 8B
Krishna Kumar (1985, 1987)	NIR imaging of nearby stars	0 detections
Shipman (1986)	IRAS search of white dwarfs	0 detections
Winglee, Dulk, & Bastiran (1986)	Radio search for cyclotron maser radiation	0 detections
Becklin & Zuckerman (1988)	NIR imaging of white dwarfs	Identified GD 165B
Leggett & Hawkins (1988, 1989)	IR photometry of Hyades candidates	0 detections
Skrutskie, Forrest, & Shure (1989)	NIR Imaging of nearby stars	Identified Gliese 569B
Henry & McCarthy (1990)	NIR speckle interferometry of nearby M stars	0 detections
Bryja et al. (1992, 1994)	Proper motion measurements of Hyades candidates	0 detections
Henry & McCarthy (1992)	NIR speckle interferometry	0 detections
Leinert et al. (1994)	NIR speckle interferometry of M stars	Found potential substellar companions LHS 1070B and LHS 1070C
Simons, Henry, & Kirkpatrick (1996)	NIR imaging of nearby stars	0 detections
Macintosh et al. (1996)	NIR imaging of Hyades M stars and white dwarfs	0 detections
Reid & Gizis (1997)	NIR imaging of Hyades M stars	0 detections

Table 1.1. (Continued)

Reference	Description	Results
Patience et al. (1998)	NIR imaging of stars possessing planets	0 detections
Rebolo et al. (1998)	Optical/NIR imaging of nearby stars	Identified G196-3
Goldman et al. (1999)	Optical/IR Proper Motion	Identified LHS 102B
Burgasser et al. (2000a)	2MASS Proper Motion Study	Identified Gliese 570D
Oppenheimer et al. (2001)	NIR imaging of nearby stars	Identified Gliese 229B
Els et al. (2001)	NIR imaging of stars possessing planets	Identified Gliese 86B
Wilson et al. (2001)	2MASS Proper Motion Study	Identified Gliese 337C, Gliese 618.1B, and HD 89744B
Kirkpatrick et al. (2001)	2MASS Proper Motion Study	Identified Gliese 417B and Gliese 584C
Gizis, Kirkpatrick, & Wilson (2001)	2MASS Proper Motion Study	Identified GJ 1048B
Hinz et al. (2002)	NIR imaging of nearby stars	0 detections
Potter et al. (2002)	NIR imaging of nearby stars	Identified brown dwarf binary companion to HD 130948
Scholz et al. (2003)	2MASS Proper Motion Study	Identified Epsilon Indi B
Albert, Doyon, & Nadeau (2003)	NIR imaging of nearby stars	0 detections
Farihi, Becklin, & Zuckerman (2003)	NIR imaging of white dwarfs	0 detections
Itoh et al. (2003)	NIR imaging of T Tauri stars	0 detections
Lowrance (2003)	NIR imaging of young stars	0 detections
Marois et al. (2003)	NIR imaging of nearby stars	0 detections
McCarthy & Zuckerman (2004)	NIR imaging of nearby stars	0 detections

The first indisputable brown dwarf companion, and indeed the first indisputably identified brown dwarf by most estimations, was the methane brown dwarf Gliese 229B (Nakajima et al., 1995), identified in the course of Ben Oppenheimer's coronagraphic survey of nearby stars (Oppenheimer et al. 2001). While other groups (Latham et al. 1989 and Stauffer et al. 1994, for example) had identified excellent brown dwarf candidates, Gliese 229B's methane abundant properties placed it firmly in the substellar regime. In the following years a number of other brown dwarf companion detections were made, though the number remains small. Table 1.2 lists known brown dwarf companions, as of the time of this writing.

Table 1.2: Known Brown Dwarf Companions to Stellar Objects

Discovery Name	Spectral Type	Approximate Mass (M_J)	Parent Spectral Type(s)*	Projected Separation (AU)	Reference
GL 86B	$\sim$ L0	$\leq$70	K0	19	Els et al. (2001)
GL 229B	T6.5	35	M1-M2	46	Nakajima et al. (1995)
HD 130948B	L2	$\leq$79	G2	47	Potter et al. (2002)
HD 130948C	L2	$\leq$68	G2	47	*Ibid*
LHS 102B	L5	69	M4	194	Goldman et al. (1999)
GJ 1048B	L1	69	K2	250	Gizis, Kirkpatrick, & Wilson (2001b)
G 196-3B	L2	25	K	300	Rebolo et al. (1998)
GL 337C	L7	57	G8, G8	881	Wilson et al. (2001b)
GL 618.1B	L4	70	M0	1090	*Ibid*
ε Indi B	T2.5	50	K5	1459	Scholz et al. (2003)
GL 570D	T8	50	K5, M1, M3	1530	Burgasser et al. (2000a)
GL 417B	L4.5	37	G0	1950	Kirkpatrick et al. (2001)
HD 89744B	L1	78.5	F7 IV-V	2460	Wilson et al. (2001)
GL 584C	L8	63	G1, G3	3620	Kirkpatrick et al. (2001)

*Spectral types refer to main sequence stars unless otherwise noted.

Chapter 2

CHAOS Observations

2.1 Target Sample

We began our candidate selection process with a careful review of the Third Catalogue of Nearby Stars (Gliese & Jahreiss 1995). Beginning with northern stars, we prioritized targets by their closeness to our solar system. Next we discarded all stars that exist in known multiple systems, as this scenario would prevent us from effectively hiding the entire parent system behind our 0.″9 coronagraphic mask. We double-checked for the presence of stellar companions using Hipparcos data (Perryman et al. 1997) as well as on-telescope preliminary imaging. As our next step, we removed all stars with a V magnitude fainter than $\sim$ 12 mags. Our previous experience using Palomar Adaptive Optics (PALAO) indicated that stars fainter than this limit were unable to serve as effective natural guide stars for the PALAO system. Next we searched the USNO-A2.0 Catalogue (Monet et al. 1998) for a corresponding point spread function (PSF) calibration star for each targeted star. For choosing a PSF calibration star, we required the following restrictions: 1) A separation less than a couple degrees from the target star; 2) A difference in V magnitude, relative

to the target star, $\lesssim 1$ mag; 3) An absence of any known companions. These restrictions ensured that the calibration star would deliver a measured PSF similar to the target star's PSF. Any target star which did not have a corresponding calibration star meeting this criterion was removed from the sample. We expanded our search region further and further south from the original northern positions until our list included a total of 80 stars extending as far south as -10 degrees. This final target sample included 3 A stars, 8 F stars, 13 G stars, 29 K stars, 25 M stars, and 2 stars with ambiguous spectral types. A complete list of the target set is given in Table 2.1.

Table 2.1: The CHAOS Target List

Parallax	Position (J1991.25)		Proper Motion		V	
(mas)	RA (H:M:S)	Dec (D:M:S)	RA (mas/yr)	Dec (mas/yr)	(mag)	Name
549.01	17:57:48.97	04:40:05.8	-797.84	10326.93	9.54	Gliese 699
392.4	11:03:20.61	35:58:53.3	-580.2	-4767.09	7.49	Gliese 411
310.75	03:32:56.42	-09:27:29.9	-976.44	17.97	3.72	Gliese 144
280.27	00:18:20.54	44:01:19.0	2888.92	410.58	8.09	Gliese 15
263.26	07:27:24.16	05:14:05.2	571.27	-3694.25	9.84	Gliese 273
206.94	11:05:32.13	43:31:28.1	-4410.79	943.32	8.82	Gliese 412
205.22	10:11:23.36	49:27:19.7	-1361.55	-505	6.6	Gliese 380
204.6*	10:19:36.28	19:52:12.0	-505**	-62**	10.0***	Gliese 388
198.24	04:15:17.64	-07:38:40.4	-2239.33	-3419.86	4.43	Gliese 166
194.44	19:50:46.68	08:52:02.6	536.82	385.54	0.76	Gliese 768
184.13	13:45:42.70	14:53:42.2	1778.46	-1455.52	8.46	Gliese 526
175.72	05:31:26.95	-03:40:19.7	82.86	-3.67	7.97	Gliese 205
174.23	16:55:29.24	-08:20:03.1	-829.34	-878.81	9.02	Gliese 644

Table 2.1: (Continued)

Parallax	Position (J1991.25)		Proper Motion		V	
(mas)	RA (H:M:S)	Dec (H:M:S)	RA (mas/yr)	Dec (mas/yr)	(mag)	Name
173.41	19:32:20.59	69:39:55.4	598.43	-1738.81	4.67	Gliese 764
170.26	19:16:55.60	05:10:19.7	-578.86	-1331.7	9.12	Gliese 752
167.51	23:49:11.95	02:24:12.9	995.12	-968.25	8.98	Gliese 908
153.24	23:13:14.74	57:10:03.5	2074.37	294.97	5.57	Gliese 892
150.96	11:00:04.53	22:50:01.1	-426.31	-279.94	10.03	Gliese 408
141.95	20:53:19.79	62:09:22.6	1.08	-774.24	8.55	Gliese 809
134.04	00:48:22.53	05:17:00.2	758.04	-1141.22	5.74	Gliese 33
132.4	01:08:12.92	54:55:27.2	3421.44	-1599.27	5.17	Gliese 53
131.12	13:29:59.12	10:22:47.2	1128	-1074.3	9.05	Gliese 514
129.54	17:25:45.57	02:06:51.5	-580.47	-1184.81	7.54	Gliese 673
119.46	12:33:45.09	41:21:24.4	-705.06	292.93	4.24	Gliese 475
119.05	17:46:27.72	27:43:21.0	-291.42	-750	3.42	Gliese 695
116.92	11:51:07.53	35:16:17.0	-271.97	254.93	9.76	Gliese 450

Table 2.1: (Continued)

Parallax	Position (J1991.25)		Proper Motion		V	
(mas)	RA (H:M:S)	Dec (H:M:S)	RA (mas/yr)	Dec (mas/yr)	(mag)	Name
115.43	05:54:23.08	20:16:35.1	-163.17	-98.92	4.39	Gliese 222
113.46	05:00:46.68	-05:45:03.5	550.74	-1109.3	6.22	Gliese 183
109.95	11:20:09.03	65:50:45.7	-2946.7	184.52	9.31	Gliese 424
109.23	13:11:52.92	27:52:33.7	-801.94	882.7	4.23	Gliese 502
109.23	08:16:08.20	01:18:08.7	124.03	1.30	10.08	GJ2066
109.21	11:52:55.82	37:43:58.1	4003.69	-5813.00	6.42	Gliese 451
104.81	11:41:03.03	34:12:09.2	-13.95	-380.46	5.31	Gliese 434
102.35	16:45:06.38	33:30:29.9	-39.18	383.41	8.1	Gliese 638
102.27	16:36:21.18	-02:19:25.8	455.22	-307.63	5.77	Gliese 631
100.24	01:47:44.06	63:51:11.2	582.05	-246.83	5.63	Gliese 75
99.44	01:02:37.95	62:20:41.4	730.1	89.27	9.56	Gliese 49
98.97	13:57:32.10	61:29:32.4	-32.32	216.48	6.49	HIP 68184****
98.26	14:01:03.67	-02:39:22.8	-824.78	599.52	9.71	Gliese 536

Table 2.1: (Continued)

Parallax	Position (J1991.25)		Proper Motion		V	
(mas)	RA (H:M:S)	Dec (H:M:S)	RA (mas/yr)	Dec (mas/yr)	(mag)	Name
98.12	04:37:40.64	52:53:41.2	305.2	-475.59	8.62	Gliese 172
96.98	22:02:10.54	01:24:03.3	-455.08	-280.37	9.17	Gliese 846
94.93	03:09:02.88	49:36:48.6	1262.29	-91.53	4.05	Gliese 124
93.81	22:06:11.82	10:05:28.8	-6.56	-5.69	10.2	HIP 109119****
93.79	16:16:43.50	67:14:19.1	-497.89	85.88	8.61	Gliese 617
93.36	17:39:17.02	03:33:19.7	-179.67	-98.24	6.53	Gliese 688
92.98	17:05:03.93	-05:03:49.5	-916.86	-1137.91	7.7	Gliese 653
92.75	12:50:43.58	-00:46:01.8	-28.77	-397.85	8.49	Gliese 488
92.2	02:17:02.42	34:13:29.4	1151.61	-246.32	4.84	Gliese 92
91.74	11:50:41.29	01:45:55.4	740.96	-271.18	3.59	Gliese 449
90.11	18:09:37.65	38:27:32.1	-316.17	-468.33	6.38	Gliese 706
90.03	00:39:22.09	21:15:04.9	-461.07	-370.88	5.88	Gliese 27
90.02	18:58:00.25	05:54:39.9	-194.47	-1221.78	9.22	Gliese 740

Table 2.1: (Continued)

Parallax	Position (J1991.25)		Proper Motion		V	
(mas)	RA (H:M:S)	Dec (H:M:S)	RA (mas/yr)	Dec (mas/yr)	(mag)	Name
89.92	15:56:26.99	15:39:53.0	311.2	-1282.17	3.85	Gliese 603
89.7	17:05:14.32	-05:05:29.3	-921.19	-1128.23	10.08	Gliese 654
88.17	13:54:41.12	18:23:54.9	-60.95	-358.1	2.68	Gliese 534
87.17	04:29:00.17	21:55:20.2	-65.14	175.55	8.30	Gliese 169
86.69	14:53:24.04	19:09:08.2	-442.75	216.84	6.00	Gliese 567
85.48	15:00:55.38	45:25:31.1	241.12	370.51	9.15	Gliese 572
85.08	15:46:26.75	07:21:11.7	-225.51	-68.52	4.42	Gliese 598
85.06	22:07:00.47	25:20:42.2	296.73	26.93	3.77	Gliese 848
83.85	11:11:04.77	30:26:47.4	592.12	-197.1	8.31	HIP54646****
81.69	05:41:20.33	53:28:56.4	2.7	-523.61	6.21	Gliese 211
80.13	05:41:30.73	53:29:27.8	3.16	-517.26	9.78	Gliese 212
80.07	10:25:11.25	-10:13:44.4	-689.12	120.68	10.15	Gliese 390

Table 2.1: (Continued)

Parallax	Position (J1991.25)		Proper Motion		V	
(mas)	RA (H:M:S)	Dec (H:M:S)	RA (mas/yr)	Dec (mas/yr)	(mag)	Name
79.8	08:52:36.13	28:19:53.0	-485.48	-234.4	5.96	Gliese 324
78.87	09:29:55.12	05:39:17.5	-504.1	110	7.2	Gliese 349
78.14	17:25:00.90	67:18:24.1	-531	3.65	6.44	Gliese 675
78.07	22:33:01.91	09:22:39.5	537.93	140.05	10.36	Gliese 863
77.82	10:30:37.76	55:58:50.2	-177.02	-33.45	4.82	Gliese 395
76.26	20:02:47.10	03:19:33.2	-92.28	120.76	7.46	Gliese 775
74.45	01:43:41.25	63:49:29.3	-394.18	-581.75	8.42	Gliese 69
73.58	05:59:37.74	58:35:37.1	8.61	-248.72	10.25	NN3371
69.73	20:45:17.27	61:50:12.5	86.08	817.89	3.41	Gliese 807
68.63	14:25:12.02	51:51:06.2	-236.06	-399.07	4.04	Gliese 549
60.8	17:30:23.87	-01:03:45.0	-126.64	-172	5.31	Gliese 678
58.5	08:54:18.19	-05:26:04.3	-413.14	30.44	6.01	Gliese 327

Table 2.1: (Continued)

Parallax	Position (J1991.25)		Proper Motion		V	
(mas)	RA (H:M:S)	Dec (H:M:S)	RA (mas/yr)	Dec (mas/yr)	(mag)	Name
54.26	09:48:35.18	46:01:16.4	222.07	-92.62	5.08	Gliese 368
53.85	00:53:04.28	61:07:24.8	-68.45	169.72	4.8	Gliese 41
50.71	22:58:15.54	-02:23:43.2	-6.05	-16.03	6.17	HIP113421****
45.43	00:45:04.92	01:47:12.9	-49.04	-573.07	8.03	Gliese 31.4

Notes. — All numerical values from Hipparcos (Perryman et al. 1997) unless otherwise noted. All names follow the Gliese catalogue system (Gliese & Jahreiss 1995) unless otherwise noted.

*Yale Trigonometric Parallaxes (van Altena, Lee, & Hoffleit 2001)

**AGK3 Catalogue (Bucciarelli et al. 1996)

***Brorfelde Meridian Catalogues (Laustsen 1996)

****Hipparcos (Perryman et al. 1997)

For a comprehensive classification of our target stars, we also seeked to get an idea of the range of ages of our systems. To accomplish this we examined Fe/H line strengths published in Cayrel de Strobel et al. (1997).[1] We then used the following relation from Rocha-Pinto et al. (2000) to estimate stellar ages.

$$t = 0.1(0.44 - [Fe/H]) \tag{2.1}$$

t is the age in Gyrs. A quarter of our sample had known Fe/H line strengths. In particular, many of the fainter M-dwarfs lacked published Fe/H lines. However, since system age does not correlate strongly with spectral type (with the exception of the rarer short-lived early-type stars), we may approximate that the stars with known Fe/H line strengths should be roughly representative of the other stars' age distributions and median values. Table 2.2 lists the target stars with published Fe/H line strengths.

2.2 Observing Hardware

To conduct our survey, we used the Palomar Adaptive Optics system (PALAO) and accompanying PHARO science camera installed on the Palomar 200-inch Hale Telescope. PALAO provided us with the high resolution (FWHM typically $\sim 0''.25$ in K-short) necessary for resolving close companions. The accompanying PHARO science camera provided us with a coronagraphic imaging capability along with a field of view ($\sim 30''$) substantially larger than any competitive adaptive optics system, at the time of the survey's commencement.

[1] The one exception is Gliese 15, whose line strength we took from Cayrel de Strobel, Soubiran, & Ralite (2001).

Table 2.2: CHAOS Target Star Iron Line Strengths

Star Name	Fe/H	Star Name	Fe/H
Gliese 53	-0.62	Gliese 211	-0.20
Gliese 15	-0.20	Gliese 166	-0.19
Gliese 27	-0.32	Gliese 205	0.60
Gliese 144	-0.31	Gliese 327	-0.02
Gliese 33	-0.29	Gliese 475	0.02
Gliese 411	-0.20	Gliese 764	-0.23
Gliese 434	-0.40	Gliese 388	-0.22
Gliese 631	0.01	Gliese 368	-0.04
Gliese 488	0.10	Gliese 395	-0.23
Gliese 75	0.36	Gliese 451	-1.50
Gliese 222	0.25	Gliese 534	0.44
Gliese 183	0.02	Gliese 502	0.19
Gliese 212	-0.20	Gliese 549	-0.05
Gliese 848	-0.10	Gliese 449	0.33
Gliese 92	-0.43	Gliese 603	-0.40
Gliese 892	0.00	Gliese 678	0.02
Gliese 673	0.40	Gliese 807	0.13
Gliese 41	0.10	Gliese 706	-0.30
Gliese 324	-0.15	Gliese 695	0.10
Gliese 380	0.28	Gliese 598	-0.04

Notes. — Fe/H values are from Cayrel de Strobel et al. (1997, 2001)

2.2.1 Palomar Adaptive Optics (PALAO)

The Palomar Adaptive Optics system (Troy et al. 2000) was designed and built at the Jet Propulsion Laboratory (JPL) in Pasadena, California. It is a facility adaptive optics (AO) system installed at the Cassegrain focus of the Palomar 200" Hale Telescope. The system uses visible light from a natural guide star to correct the near-infrared light from a science target in the same field of view. The system achieved its first high order lock on a natural guide star in December 1998. PALAO was fully commissioned as a facility instrument in May 2000. The Cornell High-Order Adaptive Optics Survey observational phase began that same month. Through the course of the survey's observational phase, PALAO achieved typical strehl ratios[2] of 50% in K-band, for 1 arcsecond seeing (0.5 μm), guide stars brighter than 8^{th} magnitude, and wind velocities 5-10 m/s (Troy et al. 2000). Figure 2.1 displays a sample image contrasting an AO exposure (otherwise known as closed-loop) with a natural seeing exposure (or open-loop exposure).

[2]The strehl ratio is a value which reflects the ratio of flux in the central core of the point spread function compared to the total flux in an equivalent non-AO point spread function.

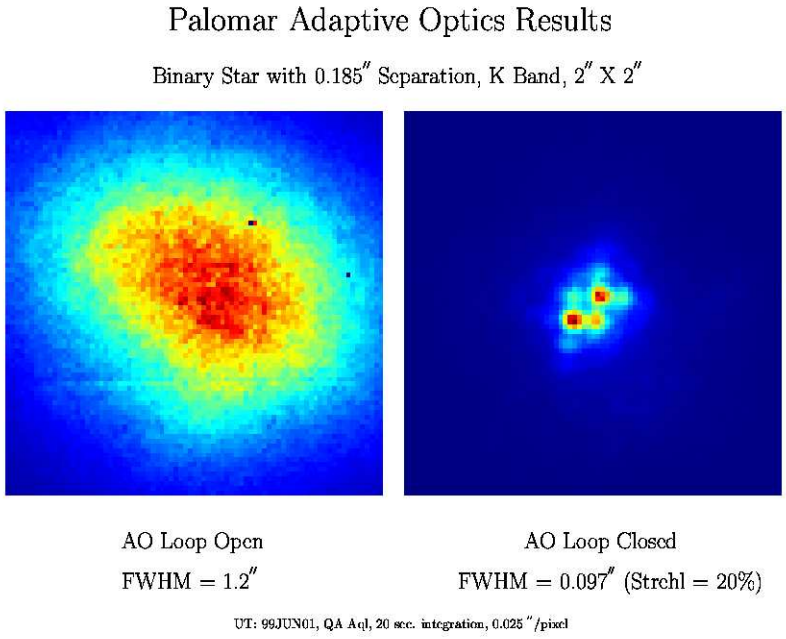

Figure 2.1: Comparison between PALAO closed and open loop on June 1, 1999. Image taken from http://ao.jpl.nasa.gov/. The image was reproduced with permission from M. Troy.

Figure 2.2 displays the optical layout of the PALAO system. As described at the JPL adaptive optics website (http://ao.jpl.nasa.gov/), the light first enters the system at the fold mirror marked "From Telescope". There the F/15.7 beam reflects to a collimating off-axis parabolic mirror. From here the collimated beam reflects to the fast steering mirror (FSM). The FSM corrects for errors in the wavefront tilt, or the angle that a plane wave makes with the surface of the primary mirror. Next the beam encounters the deformable mirror (DM). The DM corrects for errors in the phase of the incoming beam. Next, a fold mirror diverts the light back onto a second collimating off-axis parabolic mirror. Here the light converts back to the F/15.7 beam after which it moves on to the dichroic. Wavelengths shorter than 1050 nanometers deflect to the Guide Star Selection Mirrors, which allow for star selection and pupil steering. From there the light continues on to the Shack-Hartmann camera, which collects the information which will direct subsequent adjustments of the DM and FSM. Wavelengths longer than 1050 nanometers transmit through the dichroic to pass on to the PHARO science camera.

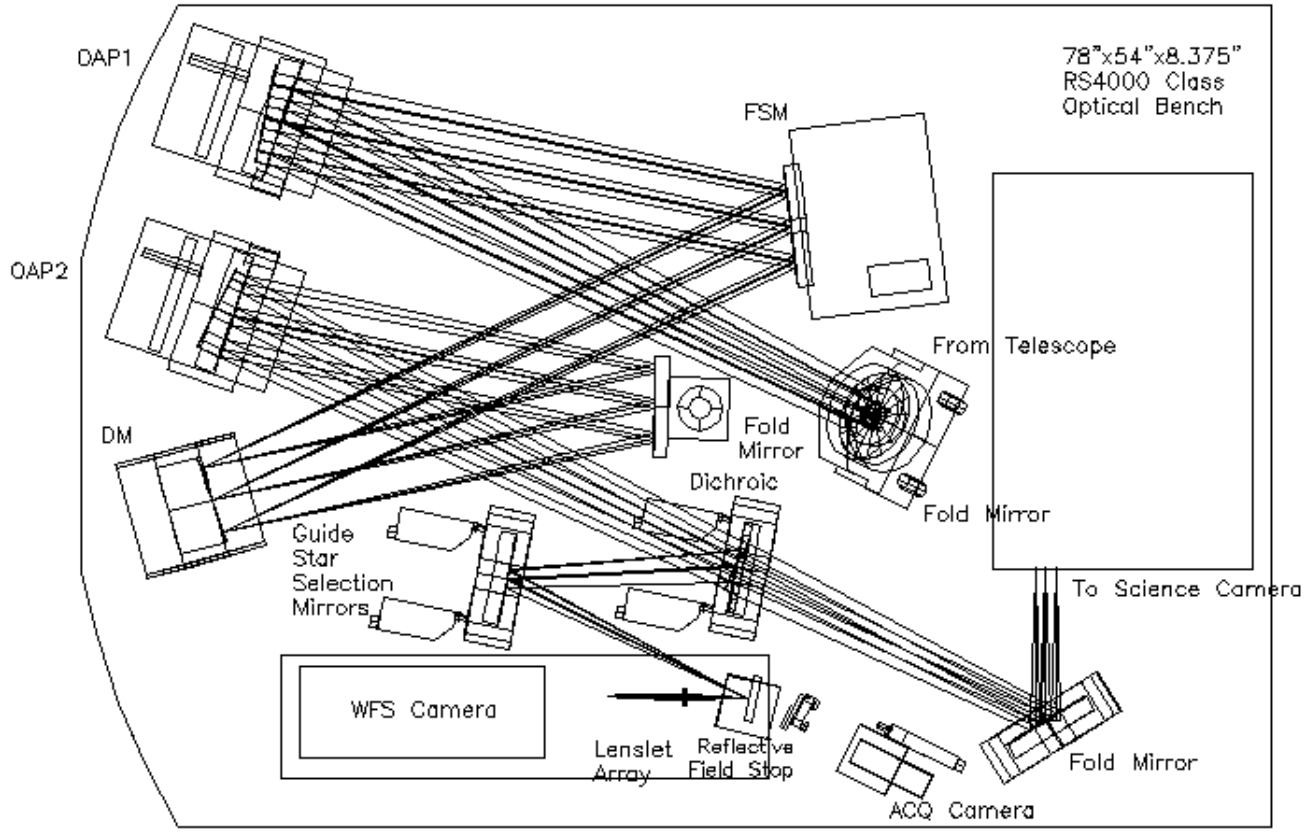

Figure 2.2: PALAO Optical Bench. Picture taken from http://ao.jpl.nasa.gov. Reproduced with permission from M. Troy and T. Hayward.

2.2.2 The Palomar High Angular Resolution Observer (PHARO)

PHARO, the Palomar High Angular Resolution Observer (Hayward et al. 2001), serves as the Palomar AO facility science camera. The instrument was designed and built at Cornell University in Ithaca, New York. It mounts along with PALAO at the Cassegrain focus of the Palomar 200" Hale Telescope. Table 2.2 summarizes the instrument specifications and capabilities. Shown there are a range of coronagraphic masks, Lyot stops, and filters which allow us to maximize high-contrast observing. In Figure 2.3 we present a schematic of the PHARO instrument. In that diagram, the light enters from PALAO and first encounters the slit wheel. For our observations we select here a 0."91 coronagraphic spot to suppress light from the parent star. Studies by Oppenheimer et al. (2000) have shown that the 0."91 spot, corresponding to 11 airy rings at 2.2 μm, provides the optimal results for high-contrast imaging in K-band. Next the beam encounters the trio of Lyot wheel, filter wheel, and grism wheel. For the Lyot wheel we select the large cross, which, using an image of the telescope pupil, suppresses light arriving from the boarders of the primary mirror, the secondary mirror's "spider" support beams, and obscurations from the secondary mirror. We note that the use of the large cross reduces the total incoming flux by a full 76%. But again, tests by Oppenheimer et al (2000) have demonstrated that this allows for maximum sensitivity at the high contrast ratios we desire. For the filter wheel, we select the K_S filter (1.99-2.30 μm), a type of K-band filter optimized for observatories with Palomar-type atmospheric absorption. We set the grism wheel to open, except for calibration imaging of brights stars, when we sometimes use the 0.1% and 1.0% neutral density filters. After passing through these three optics, the beam deflects to the carousel wheel, where we select the 40 mas/pixel setting

Table 2.3: The PHARO Science Camera

Detector Chip

- Rockwell 1024×1024 HAWAII GgCdTe
- 1 to 2.5 μm
- Read noise < 10 electrons

Imaging Scales

- 0.040 arcsec/pixel
- 0.025 arcsec/pixel

Filters

- J, H, K, K', K_S
- Various narrow-band (1%)

Coronagraphic Capabilities

- Focal plane occulting masks (0.″13, 0.″26, 0.″43, 0.″52, and 0.″97 coronagraphic spots, 2″ occulting bar)
- Pupil Plane Stops (Standard, medium, and large crosses to reduce diffraction from telescope structures)

to allow for Nyquist sampling at K-band. Thereafter the beam continues to the infrared detector.

2.3 Our Observing Protocol

2.3.1 General Observing Strategy

Our general observing strategy is to align our coronagraphic spot on a target star and take a series of short exposures as to not saturate the pixels in our detector.

Table 2.3: (Continued)

Resolving Power (Grism Mode, 0.040 arcsec/pixel)
• 1500 (J, H, or K bands) with narrow slit
Slits
• 0.”1
• 0.”2
• 0.”3

Notes. — This information follows descriptions given in Hayward et al. (2001).

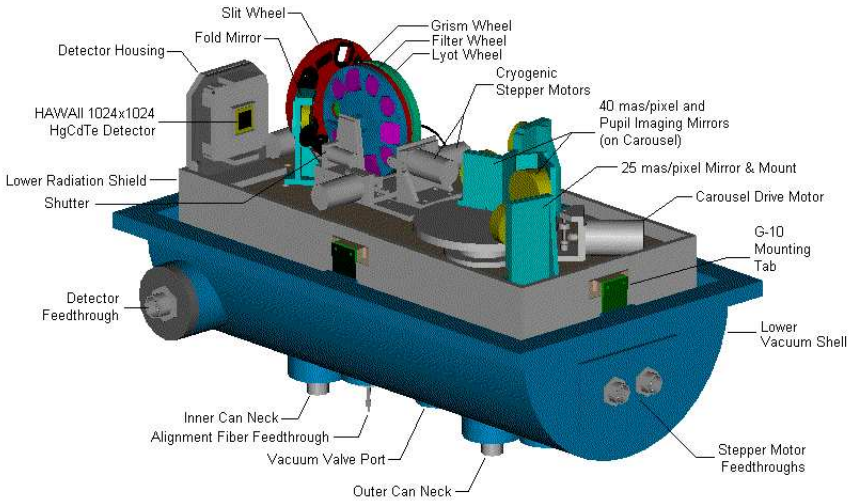

Figure 2.3: PHARO Optical Bench. Picture taken from http://astrosun2.astro.cornell.edu/research/projects/PHARO//pharo.html. Reproduced with permission from T. Hayward.

We typically conduct these exposures for no longer than $\sim$ 8 minutes of wall clock time in order to ensure that sky conditions do not significantly change between our target exposures and PSF calibration star exposures. When target star exposures are complete, we spend a similar amount of time taking coronagraphic images of our PSF calibration star. The calibration star is selected on the basis of its close proximity ($\lesssim$ 2 degrees) and similar brightness (ΔV $\lesssim$ 1.0) to the target star. Immediately flanking these two sets, we take dithered images of a nearby empty sky region. We repeat this process as many times as necessary to reach our desired signal to noise. Once we complete these image sets, we insert a neutral density filter in our optical path and conduct dithered exposures of our target star. These images allow us to characterize and record instrument and site observing conditions. Table 2.3 displays all of our surveyed stars along with observation dates and net target exposure times.

2.3.2 A Sample Observing Set

To explain this observing strategy in greater detail, I summarize a typical observational set from start to finish: At twilight, we point the telescope to a set position and begin taking our calibration flatfields. For these calibration images we make sure that all possible PHARO settings are identical to settings that we will be using during our target observations: The slit wheel is set to 0."91 coronagraphic spot; The Lyot wheel is set to big cross; The filter wheel is set to K_S filter and the carousel is set to a 40 mas/pixel platescale. While we often change the grism wheel and filter wheel during the night, the slit, Lyot, and carousel generally remain at their initial settings throughout the night. With our AO system disengaged, we take a dozen or so images as the sky fades to darkness. We space these images appropriately to achieve pixel counts which span the range between minimum and maximum

Table 2.4: List of CHAOS Observations

Parallax (mas)	V (mag)	Name	Dates of Coronagraphic Observations	Net Exposure Time (sec)
549.01	9.54	Gliese 699	6/02	363
392.4	7.49	Gliese 411	5/00	218
310.75	3.72	Gliese 144	8/00	545
280.27	8.09	Gliese 15	8/00	482
263.26	9.84	Gliese 273	11/00	291
206.94	8.82	Gliese 412	12/02	600
205.22	6.6	Gliese 380	12/01	291
204.6*	10.0**	Gliese 388	12/02	291
198.24	4.43	Gliese 166	12/01	581
194.44	0.76	Gliese 768	6/02	291
184.13	8.46	Gliese 526	6/01	654
175.72	7.97	Gliese 205	12/01	581
174.23	9.02	Gliese 644	6/02	636
173.41	4.67	Gliese 764	6/01	799
170.26	9.12	Gliese 752	9/00; 6/01	1247

Table 2.4: (Continued)

Parallax (mas)	V (mag)	Name	Dates of Coronagraphic Observations	Net Exposure Time (sec)
167.51	8.98	Gliese 908	8/00	654
153.24	5.57	Gliese 892	9/00; 11/00	1126
150.96	10.03	Gliese 408	2/02	580
141.95	8.55	Gliese 809	8/00	654
134.04	5.74	Gliese 33	8/00	594
132.4	5.17	Gliese 53	8/00	908
131.12	9.05	Gliese 514	5/00; 6/01	1199
129.54	7.54	Gliese 673	9/00; 6/01	1145
119.46	4.24	Gliese 475	6/01	872
119.05	3.42	Gliese 695	6/02	581
116.92	9.76	Gliese 450	2/02; 12/02	1708
115.43	4.39	Gliese 222	11/00	273
113.46	6.22	Gliese 183	11/00; 12/01	1163
109.95	9.31	Gliese 424	6/01	618
109.23	4.23	Gliese 502	2/02	545

Table 2.4: (Continued)

Parallax (mas)	V (mag)	Name	Dates of Coronagraphic Observations	Net Exposure Time (sec)
109.23	10.08	GJ2066	12/01	600
109.21	6.42	Gliese 451	2/02; 6/02	1708
104.81	5.31	Gliese 434	5/00	654
102.35	8.1	Gliese 638	5/00	273
102.27	5.77	Gliese 631	5/00	654
100.24	5.63	Gliese 75	11/00	297
99.44	9.56	Gliese 49	8/00	908
98.97	6.49	HIP 68184***	5/00	864
98.26	9.71	Gliese 536	5/00	320
98.12	8.62	Gliese 172	11/00; 12/01	1160
96.98	9.17	Gliese 846	8/00	900
94.93	4.05	Gliese 124	11/00; 12/02	872
93.81	10.2	HIP 109119***	6/02	900
93.79	8.61	Gliese 617	6/02	1090
93.36	6.53	Gliese 688	6/02	600

Table 2.4: (Continued)

Parallax (mas)	V (mag)	Name	Dates of Coronagraphic Observations	Net Exposure Time (sec)
92.98	7.7	Gliese 653	5/00	981
92.75	8.49	Gliese 488	5/00	899
92.2	4.84	Gliese 92	9/00; 11/00	545
91.74	3.59	Gliese 449	2/02	818
90.11	6.38	Gliese 706	6/02	818
90.03	5.88	Gliese 27	8/00	908
90.02	9.22	Gliese 740	5/00; 8/00	1200
89.92	3.85	Gliese 603	2/02	872
89.7	10.08	Gliese 654	6/02	581
88.17	2.68	Gliese 534	2/02; 6/02	854
87.17	8.30	Gliese 169	11/00	1090
86.69	6.00	Gliese 567	2/02	872
85.48	9.15	Gliese 572	5/00	727
85.08	4.42	Gliese 598	6/02	1163
85.06	3.77	Gliese 848	11/00	1090

Table 2.4: (Continued)

Parallax (mas)	V (mag)	Name	Dates of Coronagraphic Observations	Net Exposure Time (sec)
83.85	8.31	HIP54646***	5/00	928
81.69	6.21	Gliese 211	12/01	1090
80.13	9.78	Gliese 212	12/02	1163
80.07	10.15	Gliese 390	2/02	1163
79.8	5.96	Gliese 324	12/01	2616
78.87	7.2	Gliese 349	12/01; 12/02	2117
78.14	6.44	Gliese 675	5/00	1090
78.07	10.36	Gliese 863	8/00	1200
77.82	4.82	Gliese 395	2/02	1163
76.26	7.46	Gliese 775	5/00	981
74.45	8.42	Gliese 69	11/00	1226
73.58	10.25	NN3371	11/00	1199
69.73	3.41	Gliese 807	6/02	1163
68.63	4.04	Gliese 549	2/02	1090

Table 2.4: (Continued)

Parallax (mas)	V (mag)	Name	Dates of Coronagraphic Observations	Net Exposure Time (sec)
60.8	5.31	Gliese 678	6/02	872
58.5	6.01	Gliese 327	12/01	1272
54.26	5.08	Gliese 368	12/02	1163
53.85	4.8	Gliese 41	12/01	2326
50.71	6.17	HIP113421***	9/02	1272
45.43	8.03	Gliese 31.4	12/01	1744

Notes. — All numerical values from Hipparcos (Perryman et al. 1997) unless otherwise noted. All names from Gliese catalogue (Gliese & Jahreiss 1995) unless otherwise noted.

*Yale Trigonometric Parallaxes (van Altena, Lee, & Hoffleit 2001)

**Brorfelde Meridian Catalogues (Laustsen 1996)

***Hipparcos (Perryman et al. 1997)

measurable fluxes.

Using a neutral density filter to avoid pixel saturation, we next align on a bright standard star and make sure that our adaptive optics system is working as expected. At this stage we may also measure seeing and get a rough idea how weather/sky conditions are affecting our AO system (i.e. wind, clouds, airborne particulates, etcetera). We are then ready to begin our target exposures.

Still using our neutral density filter to safeguard against pixel saturation, we point the telescope at our target object and engage the AO system lock. After optimizing our AO settings to ensure a narrow stable PSF, we make adjustments to telescope positioning to align our star behind the coronagraphic spot. Figure 2.4 displays a sample coronagraphic star image. With the majority of the target star flux suppressed, we remove our neutral density filter and estimate an optimal exposure time. Typically we look for a happy median between our desire to avoid pixel saturation while still maximizing the exposure time of a given image. Taking longer exposures, as opposed to more numerous shorter exposures, helps reduce the total readout time. We record the optimal exposure time as well as the telescope's final position. Disengaging our adaptive optics lock, we then move to the corresponding PSF calibration star and repeat this procedure. Since we desire our calibration star to have a PSF resembling our target star, we do not alter any of our AO system settings from the target star setup. We next select an exposure time which makes the PSF star measured flux roughly equivalent to the target star's flux. While the PSF star exposure times may differ from our target star's, we make sure that the net exposure time is roughly identical. Next we disengage our lock and move $120''$ away from the calibration star to take dithered images of the sky. The number of sky images here and the length of the exposures are identical to the calibration star

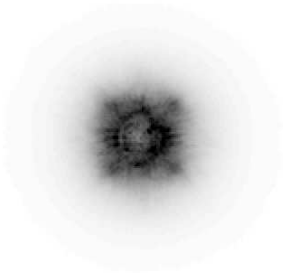

Figure 2.4: A close-up of a Gliese 183 coronagraphic image taken by J. Carson in December, 2001 using Palomar 200-inch Adaptive Optics and accompanying PHARO science camera. The image reduction process included sky subtraction, flatfielding, bad pixel filtering, and median combination. While the star remains covered with a $0\farcs91$ spot, residual starlight can still be seen leaking out from the edges. The square-like point spread function is characteristic of the AO-reconstructed PSF.

set. When these "skys" are complete, we return to the calibration star and close our AO loop. After fine-tuning our coronagraphic spot positioning, we commence with our exposures. When these are complete, we disengage our AO lock and return to the target star. Engaging our AO lock and fine-tuning the coronagraphic spot positioning, we begin our exposure set of the target star. Once this is complete we move $120''$ away from the target and take an equal number (with identical exposure times) of dithered sky images. The complete cycle typically takes about twenty-five minutes of wall-clock time. We repeat the procedure (sky, calibration star, target star, sky) until we achieve desired net exposure times.

At the end of all of our sets, we select a neutral density filter and adjust the telescope so that our target star resides in the field, but avoids the coronagraphic spot. Here we take a dozen or so closed-loop images of the parent star at different positions on the detector. These allow us to record the quality of our PSF as well as gauge the instrument throughput. Figure 2.5 displays a sample image with the

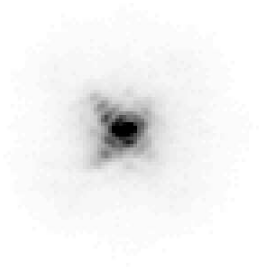

Figure 2.5: A close-up of a Gliese 183 non-coronagraphed image taken by J. Carson in December, 2001 using Palomar 200-inch Adaptive Optics and accompanying PHARO science camera. The image reduction process included sky subtraction, flat-fielding, bad pixel filtering, and median combination. The cross-like point spread function is characteristic of the AO-reconstructed PSF.

star moved off the coronagraphic spot.

2.3.3 Common Proper Motion Observations

For candidate companions detected in the previous procedures, we may check for a physical companionship by using common proper motion observations. The nearby stars we observe tend to have high proper motions (like a few hundred mas/year). The vast majority of false candidate companions are background stars which tend to have very small proper motions compared to the parent star. Therefore, after recording our initial measurement, we wait for a timespan long enough for the parent star to move a detectable distance. We then repeat our observing set so that we may check to see if the candidate maintains the same position with respect to the parent star. Target stars reobserved to check for common proper motion include Gliese 740, 75, 172, 124, 69, 892, 752, 673, 41, 349, 412, 451, 390, 678, 768, 809, 49, and 688. Due to instrument scheduling constraints, Gliese 412, 49, 41, 390,

678, 688, 809, and 768 were all re-observed using the Palomar 200-inch Wide-field Infrared Camera (WIRC) rather than PALAO and the accompanying Pharo science camera. These near-IR WIRC follow-up observations were conducted in May, 2004 by Sarah Higdon and James Higdon (Cornell University). Since the WIRC camera possesses no coronagraphic mode, the observations were instead conducted using standard dithered exposure sequences of the candidate objects.

Chapter 3

CHAOS Data Analysis

3.1 Introduction

We began our data reduction by median-combining each of the dithered sky sets. We then took each coronagraphed star image and subtracted the median-combined sky taken closest in time to the star image. (The typical separation in time between target and sky images was ∼5.5 minutes.) We divided each of the sky-subtracted star images by a flatfield frame that we created, using standard procedures, from twilight calibration images taken that same night. Next we median-combined each sequence of coronagraphed star frames. For this median-combination, we used the images' residual parent star flux (which leaked from around the coronagraph) to realign any frames that may have shifted due to telescope drift. Next we applied a bad pixel algorithm to remove suspicious pixels (like dead pixels or ones affected by cosmic rays) and replace them with the median of their neighbors. After we completed this procedure for both target star and calibration star image sets, we scaled the calibration star PSF to most closely resemble the target star PSF. We then centered the scaled PSF on the target star PSF and subtracted. In the cases

where we had multiple target star/calibration star observing set pairs, we co-added the final images. Finally, we applied a Fourier filter to help remove non-point-like features such as unwanted internal instrument reflection and residual parent star flux. Figures 3.1 through 3.7 display sample target images at different stages of image reduction. We note that the contrast levels remain constant for figures 3.1 through 3.5 and 3.6 through 3.7. (In other words, we have two sets of settings, one for figures 3.1 through 3.5 and another for 3.6 through 3.7.) After completing all of the data reduction procedures, we concluded that no target systems provided positive evidence of having a brown dwarf companion. In the following sections, we describe some of the more complicated parts of our procedures in greater detail.

3.2 Image Reduction

3.2.1 Creating Twilight Flats

Section 2.3.2 described our twilight flat observing protocol. To create a single twilight flat from those exposures we did the following: First we took each twilight image and subtracted the preceding twilight image. (We omitted this step for the first image which, of course, had no preceding image.) The resulting arrays represented the difference between images of different uniform illumination. Next we normalized our difference arrays so that non-vignetted portions of the array had a median value of one. We set all zero values equal to a value of one in order to avoid any subsequent division by a value of zero. It is acceptable to neglect properly correcting these pixels since our bad pixel filter will correct these pixel values later on. Next we median-combined our differenced images and again re-normalized the final array to one, just to be safe. The resulting array reflected variations in pixel

sensitivity for all working pixels (i.e. ones not flagged by our bad-pixel algorithm).

3.2.2 Applying Bad Pixel Filters

For this filter, we looped through the un-vignetted portion our image and, for every pixel, calculated the standard deviation of the eight neighboring pixels. If the central pixel differed from the average of the surrounding pixels by more than 5-sigma, then we replaced the central value with that average. Clusters of bad pixels were sometimes resistant to this technique, but running the filter multiple successive times helped break down these clusters.

3.2.3 Median-Combining Coronagraphed Star Images

The reader is likely aware that median-combining involves taking a sequence of images and creating a final image where each pixel value represents the median flux value at that pixel position. This, of course, helps remove unwanted effects such as cosmic rays or anomalous pixel values. In our version, the only deviation from this standard technique was our re-aligning of images that shifted due to telescope drift; In a typical 5-8 minute observing sequence, we found that the telescope drifted anywhere from 0-3 pixels (one pixel equals 40 mas).[1] For the re-alignment procedure, we designated the first image of the sequence as our reference array. All subsequent images were compared to this one to see if a shift was necessary. We applied our bad pixel algorithm to all of the compared images so our shift would not be influenced by cosmic arrays or anomalous pixel values. Next we used a trial and error method to determine any necessary shifts: We shifted each array through a range of ± 5

[1]The phrasing "telescope drift" might be somewhat of a misnomer. A dominant portion of this drift likely derives from differential flexure between the AO and PHARO science camera (M. Troy, private communication, July 2004).

pixels in the up, down, left, and right directions. To determine the best of these positions, we used a least squares fit to measure the differences between our reference PSF and the compared PSF. As the coronagraphic spot covered a radius about 12 pixels, we used 20-100 pixel radius from the spot center as our area to conduct the least squares fit. We selected this region since it contained a significant amount of star flux (leaking from behind the coronagraph) while remaining separated from the region closest to the coronagraphic spot, where diffraction effects caused high noise. We recorded the best fit-position and shifted the designated array accordingly.

3.2.4 Subtracting the Calibration Star PSF

Our PSF subtraction procedure allowed us to increase sensitivity in regions close to the coronagraphic spot. Our technique accordingly aimed to subtract a calibration star PSF which most closely resembled the target star PSF. On the data reduction side, we achieved this goal by scaling and shifting our calibration star PSF to most closely resemble the target star PSF. We began by first estimating the residual sky flux, in both the target and calibration images, by measuring the median flux in a parent star-centered sky annulus extending 250 to 280 pixels. After subtracting this residual sky flux, we made a first-run attempt at scaling our calibration PSF: We measured the median value, for both the target star and the calibration star, in an annulus ranging 50 to 90 pixels from the coronagraphic spot center; We then divided our calibration star frame by the ratio of calibration star to target star. This action roughly scaled the calibration star flux to the target star flux. Next we fine-tuned this scaling by multiplying the calibration PSF by values ranging from 0.20 to 1.76 at intervals of 0.04. For each of these scaled PSFs, we also sampled shifts in the up, down, right, and left directions out to 7 pixels. For each sample combination,

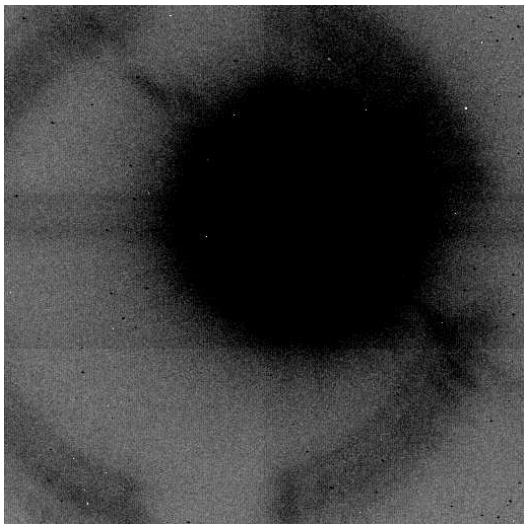

Figure 3.1: A closeup of a raw coronagraphic image of Gliese 183 taken by J. Carson in December, 2001 using Palomar 200-inch Adaptive Optics and accompanying PHARO camera. The image represents a $20'' \times 20''$ field of view.

we conducted a least squares fit between the target and calibration PSF for all cells 50 to 90 pixels from the coronagraphic spot center. The best-fit parameters were then used for our PSF subtraction. In figures 3.4 and 3.5 we display a sample target image before and after the calibration PSF subtraction.

3.2.5 Combining Multiple Observing Sets

In the cases where we took multiple, consecutive image sets for a given target, we summed all of our final PSF-subtracted images to form a single final image. At the same time we summed all of our pre-PSF-subtracted images to form a single non-subtracted image. We preserved these non-subtracted images in addition to the PSF-subtracted versions because they displayed better sensitivities for potential companions significantly separated (say $\gtrsim 5$ arcseconds) from the parent PSF. For image sets of a single target, but taken on different nights, we summed all of the PSF-subtracted final images together, making sure to correct for any differences in

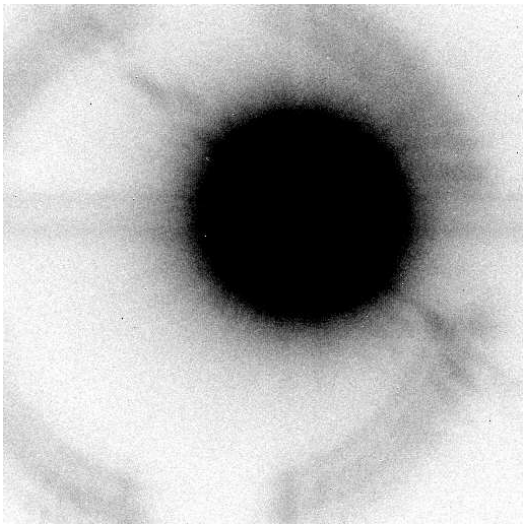

Figure 3.2: This frame represents the image shown in Figure 3.1 after a sky frame has been subtracted. Note that the background flux has diminished noticeably along with many of the bad pixels (e.g. dead pixels or those affected by cosmic rays).

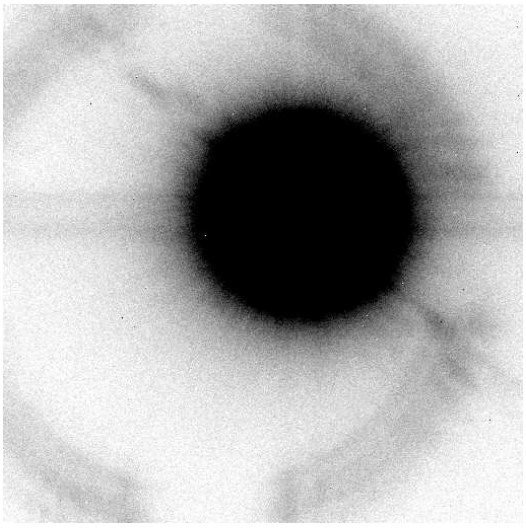

Figure 3.3: This frame represents the image shown in Figure 3.2 after a flatfield has been applied.

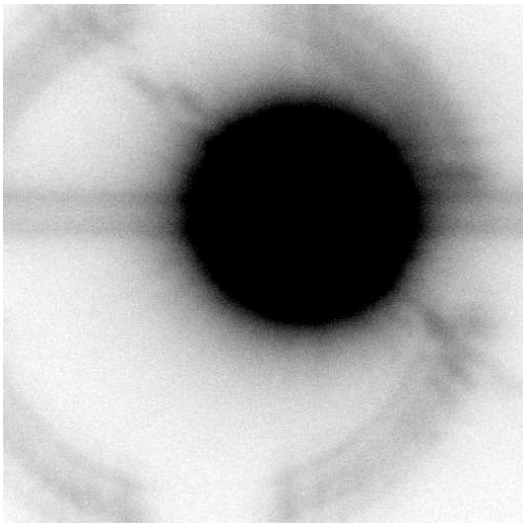

Figure 3.4: This frame represents the image shown in Figure 3.3 after applying a median combination and bad pixel filter. Note that the residual parent star flux displays a smoother PSF, making it easier for us to subsequently model and subtract it. The image also displays fewer bad pixels.

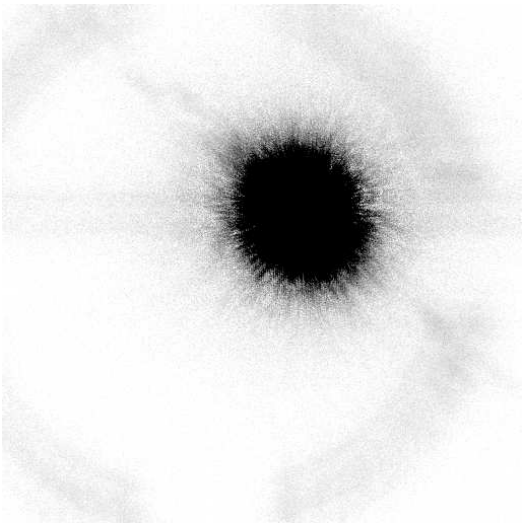

Figure 3.5: This frame represents the image shown in Figure 3.4 after the subtraction of a processed calibration PSF. Note the significant reduction in the parent system's residual PSF.

exposure times. We used visual inspection to correct for position differences between the different images. For the non-PSF-subtracted images taken on different nights, we used the median-combination technique described in section 3.2.3. We chose to use this median-combination technique since, unlike the case of PSF-subtracted images, we had a well-defined parent star PSF residual to correct for any changes in coronagraphic spot positions between the two nights.

3.2.6 Fourier Filtering

A Fourier filter application made up the final stage of our data reduction. This served to reduce residual parent star flux and remaining internal instrument reflection (see figures 3.6 and 3.7). For these algorithms, we took advantage of the fact that point-like stars appear at high frequencies in Fourier space while the more shallow-sloping internal instrument reflection and coronagraphic leakage reside at lower frequencies. Therefore, we designed our fourier filter to de-emphasize lower frequency flux and maximize higher frequency flux.

To perform this task, we begin using IDL's FFT routine to conduct a two-dimensional fast-Fourier transform of the image array so that the lowest frequency flux resided at the center of the transformed array while higher frequency flux resided further and further toward the edges. We then multiplied each pixel in the transformed array, out to a radius of r_{max} pixels from the center, by a value given by the following exponential equation.

$$F = e^{\frac{r - r_{max}}{\sigma}} \tag{3.1}$$

While F is the value we multiply each pixel by, r is the distance, in units of pixels, between a given pixel and the center of the image (which corresponds to zero

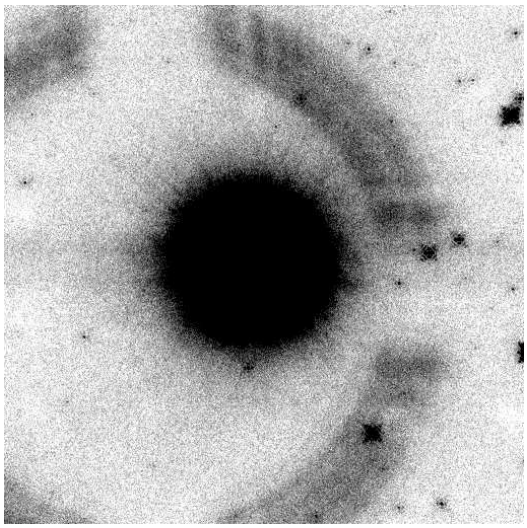

Figure 3.6: Coronagraphic image of Gliese 740 taken by J. Carson in August 2000 on the Palomar 200-inch. The image represents a $20'' \times 20''$ field of view.

frequency). σ is a characteristic constant which we set to 34.0. r_{max} is the maximum distance, again in units of pixels, out to which we apply our function. In our case we set r_{max} to 23.0 pixels. After applying this function to the Fourier array, we ran a reverse Fourier transform to restore our image. Figures 3.6 and 3.7 display the before and after stages of the Fourier-altered image.

How Did We Choose Our Fourier Algorithm?

Before deciding on Equation 3.1, we used a trial and error method to test a wide variety of parameters. With the goal of de-emphasizing the power at lower frequencies, we tested both an exponential function, shown in Equation 3.1, as well as a Gaussian version of the form:

$$F = e^{\frac{r - r_{max}}{\sigma^2}} \tag{3.2}$$

F, r, r_{max}, and σ represent the same parameters as those described with equation 3.1. Inspection of the frequency space image led us to narrow our parameters to r_{max}

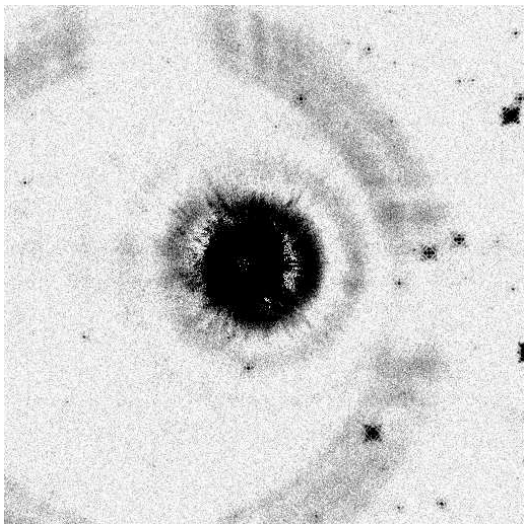

Figure 3.7: A Fourier filtered version of the image in Figure 3.6. Notice the reduction in internal instrument reflection (represented by the large truncated ring) as well as the reduction in leakage from behind the coronagraphic spot. For 24 field stars measured in the full uncropped image, the signal-to-noise ratio improved by a median value of 24% compared to the unfiltered image.

= 5 - 49 pixels and $\sigma = 1$ - 39. We then sampled these parameters for both Gaussian and exponential versions at integer intervals for r_{max} and σ. As our test-case image, we selected the crowded field image of Gliese 740, a region close to the galactic plane (see Figure 3.6). Then, for each sampled parameter combination, we applied our Fourier algorithm and measured the signal-to-noise for 24 different field stars. The chosen field stars covered the range from the very faint to the easily visible, at positions ranging from close-in to the coronagraphic spot to the outer edges of our field. Since we wanted to make sure that our Fourier algorithm improved signal-to-noise at a range of brightnesses and field positions, our first analysis selected parameters that improved the signal-to-noise for the greatest number of stars. (For our selected best cases, 22 stars exhibited improvement; 2 stars exhibited a decrease in signal to noise.) This narrowed our options down to a relatively small subset. Secondly, we searched for the parameters which maximized the median improvement in signal-to-

noise. By this procedure, we settled on equation 3.1, with the parameters described immediately following that equation. This function improved typical signal-to-noise levels by $\sim 24\%$.

3.3 Detection Algorithms

Our first step in identifying brown dwarf companions was individually inspecting each final image for any potential companions. The characteristic Adaptive Optics waffle pattern (see Figure 2.5) helped distinguish real objects from false ones. Practically, we found that this individual inspection was the most effective method of identifying candidate companions. However, for the purpose of creating eventual population models, we chose to use a more quantifiable detection system as well.

Our automated detection algorithm began by first selecting the non-vignetted region and array and rebinning the pixels so the total number of pixels reduced by a factor of four. This rebinning allowed us to conserve computing time. Since we eventually used a flux photometry aperture of 4 pixels (measured in units of non-rebinned pixels), we lost very little relevant information in this rebinning. Next our algorithm sampled each rebinned pixel (excepting a 10-pixel boundary along the edges) and performed aperture photometry (4 pixel aperture width, 15-20 pixel sky annulus) centered on the sampled pixel position. Along with each signal measurement was recorded a corresponding noise value based on the standard deviation of the sky annulus pixel values as well Poisson noise associated with the measured signal. In the end, we arrived at a final array with a signal to noise value for each sampled pixel. Next, the program selected the pixel with the highest signal to noise value, using a minimum signal to noise criterion of five. We recorded the pixel position and then moved on to record the next highest signal to noise value greater

than five. After each detection, we voided a five pixel radius (rebinned pixel units) around the detected candidate object. Thus, we effectively voided any detection within 0.4 arcsec of a brighter candidate object. We continued this procedure until there were no more positions with signal to noise values greater or equal to five. (Of course, for many images, no positions possessed signal to noise levels greater than five.) After identifying the candidate sources we re-examined the original final image to ensure that the algorithm had indeed detected a true source as opposed to a systematic effect. Again, we searched for the Adaptive Optics signature waffle pattern to ensure a true physical source. We also made comparisons to images taken at other sources to ensure that our feature was indeed unique to our target image.

3.4 Testing Brown Dwarf Candidates

Upon first discovering a potential brown dwarf companion to our parent star, we calculate an estimate of its apparent K_s magnitude. We do this by first conducting aperture photometry on the candidate object. We then use our "strehl" data to arrive at a relationship between measured ADU and apparent K_s magnitude. (Our "strehl" images consist of non-coronagraphed images of the parent system taken immediately after conducting the target observing sets.) Since our parent stars have well-defined K_s magnitudes, thanks to observing surveys like 2MASS (Skrutskie et al. 1997), we can easily arrive at a relationship between counts and magnitude. For the cases where our "strehl" images are taken with neutral density filters in place, we correct for this effect using neutral density filter transmission values determined by J. Carson with data collected over the course of the CHAOS survey. Having included all necessary corrections, we arrive at an equation to convert our candidate brown dwarf aperture counts to an apparent K_s magnitude.

Once we establish an apparent K_s magnitude, we derive a corresponding absolute K_s magnitude, assuming the candidate has a distance equal to the parent system. Thanks to observational surveys such as Hipparcos (Perryman et al. 1997), all of our parent stars have well-defined parallaxes and therefore distances. With an approximate absolute K_s magnitude in hand, we combine published brown dwarf observational data (Leggett et al. 2000, Leggett et al. 2002, Burgasser et al. 1999, Burgasser et al. 2000b, Burgasser et al. 2002a, Burgasser, McElwain, & Kirkpatrick 2003, Geballe et al. 2002, Zapatero et al. 2002, Cuby et al. 1999, Tsvetanov et al. 2000, Strauss et al. 1999, and Nakajima et al. 1995) with theoretical data from Burrows et al. (2001) to extrapolate constraints on the object's mass. An object whose potential mass falls within acceptable brown dwarf restrictions is designated for common proper motion follow-up observations.

For our follow-up observations, we use Hipparcos published common proper motion values (Hipparcos catalogue; Perryman et al. 1997) to determine the expected movement of the parent system. Since background and field stars are unlikely to possess proper motions identical to the parent system's, we may use common proper motion as a strong support for a physical companionship. To determine the candidate companion's relative position in different epoch images, we fit a gaussian profile to the candidate companion flux position. For the parent star, we determine position from an extrapolated gaussian profile created from the flux leaking from behind the coronagraphic spot. Measuring the candidate companion's relative position over the two epochs, we are able to distinguish physical companionships from chance alignments.

As mentioned in section 2.3.3, Gliese 412, 49, 41, 390, 678, 688, 809, and 768 were all re-observed using the Palomar Wide-field Infrared Camera (see chapter 6

for a complete discussion of the WIRC instrument). While WIRC, with its non-AO-corrected point spread function and lack of a coronagraphic spot, makes a poorer probe of astrometry than our Pharo camera, the systems in question all possessed large expected proper motions (>400 mas [1 WIRC pixel ∼250 mas]) and large separations (>10 arcseconds) from the parent system, making them acceptable WIRC observing targets. But despite WIRC's adequacy, for the cases of Gliese 412, 768, 688, and 809, our available net exposure times were too short for us to positively confirm or reject common proper motion. 2MASS field density data does give us some information on the odds of each of these companions being a background star. According to that survey, our chances of having a non-associated field star within our Pharo field of view are 1%, 14%, 76%, and 86% for Gliese 412, 768, 688, and 809, respectively. For Gliese 768, 688, and 809, the likelihood of there being a field star is therefore very substantial. For Gliese 412, however, the field is uncrowded enough that the likelihood of it being a true brown dwarf companion rises. (For a real companionship, its magnitude would place it somewhere around an L9 dwarf classification.) However, in a survey of 80 target stars, we would expect a 1% chance alignment to occur in one of our target systems. In the end though, these speculations cannot confirm or reject the presence of a true brown dwarf companion. For the cases of subsequent population simulations therefore, we treat these candidates as non-brown dwarf companions until a time when we may confirm their substellar companion nature.

3.5 Measuring Survey Sensitivities

3.5.1 Creating Noise Maps

For each target star observing set, we create a noise map from the information contained in the final PSF-subtracted and non-subtracted target frame. Selecting the non-vignetted portions of each of the two frames, we rebin the selected regions' pixels so that each dimension reduces by a factor of two. This rebinning helps us save computing time and is allowable since our flux apertures for photometry have diameters larger than this size. We next determine a noise estimate for each pixel using the procedures described in section 3.3. In the end we have two arrays representing a noise map for each of the final PSF-subtracted and non-PSF-subtracted image. To consolidate these two arrays into a single noise map, we sample each pixel position and select the lesser of the noise values between the two maps. By doing this we, in effect, recognize that the PSF-subtracted final image has greater sensitivity for certain positions (in particular, close to the parent star) while the non-subtracted image has greater sensitivity for other regions (like large separations from the parent stars). Figure 3.8 displays a subtracted and non-subtracted target image along with the corresponding consolidated noise map.

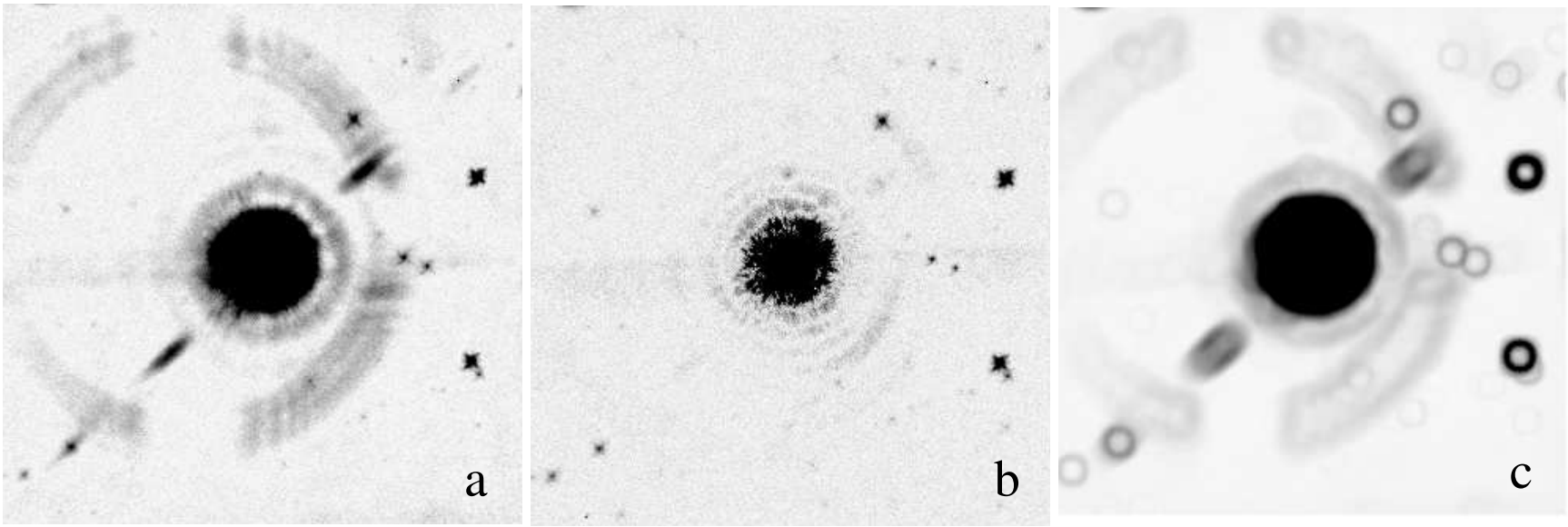

Figure 3.8: Gliese 740 Final Images and Noise Map. a) Gliese 740 Non-PSF-Subtracted Final Image. b) Gliese 740 PSF-Subtracted Final Image. c) A composite noise map created from (a) and (b). The doughnut-shaped rings toward the outskirts in (c) represent high-noise regions caused by the detection algorithms' difficulty in identifying sources in close proximity to field stars.

3.5.2 Determining Limiting Magnitudes

To quantify detection sensitivities from these noise maps, we look to determine the faintest detectable magnitude as a function of angular separation from each parent star. We begin by declaring an array of sample apparent K-magnitudes extending from 8 to 23 mags at intervals of 0.3 mags. This selection includes all potential brown dwarf magnitudes that we are likely to encounter. We do note that some of the lowest luminosity brown dwarfs may have magnitudes dimmer than our 23-magnitude limit. However, since 23 magnitudes is effectively beyond even the most optimistic sensitivity estimates, we do not need to consider anything fainter than that. We next transform our apparent magnitudes to instrument counts (ADU) using the method described in section 4.2.

Returning to our noise map, we determine the median values in a series of concentric $0''.16$-thick rings centered on the noise map center. Our median values therefore represent typical noise as a function of distance from our central star. For each noise value, we then determine the minimum apparent K-magnitude where signal exceeds the combined Poisson noise and ring noise by a factor greater or equal to 5. In Figure 3.9 we plot, as examples, the resulting measurements for Gliese 638 (K_s = 4.7), Gliese 75 (K_s = 4.0), Gliese 222 (K_s = 3.0), and Gliese 768 (K_s = 0.1). Refer to Table 3.1 for a summary of minimum detectable magnitudes for the complete survey target list.

Another commonly used statistic for describing sensitivities for high-contrast companion surveys is the limiting differential magnitude according to angular separation from the parent star. In other words, how many times dimmer may a companion object be before we lose it in the parent star noise? Figure 3.10 plots these limiting differential magnitudes for the target stars displayed in Figure 3.9.

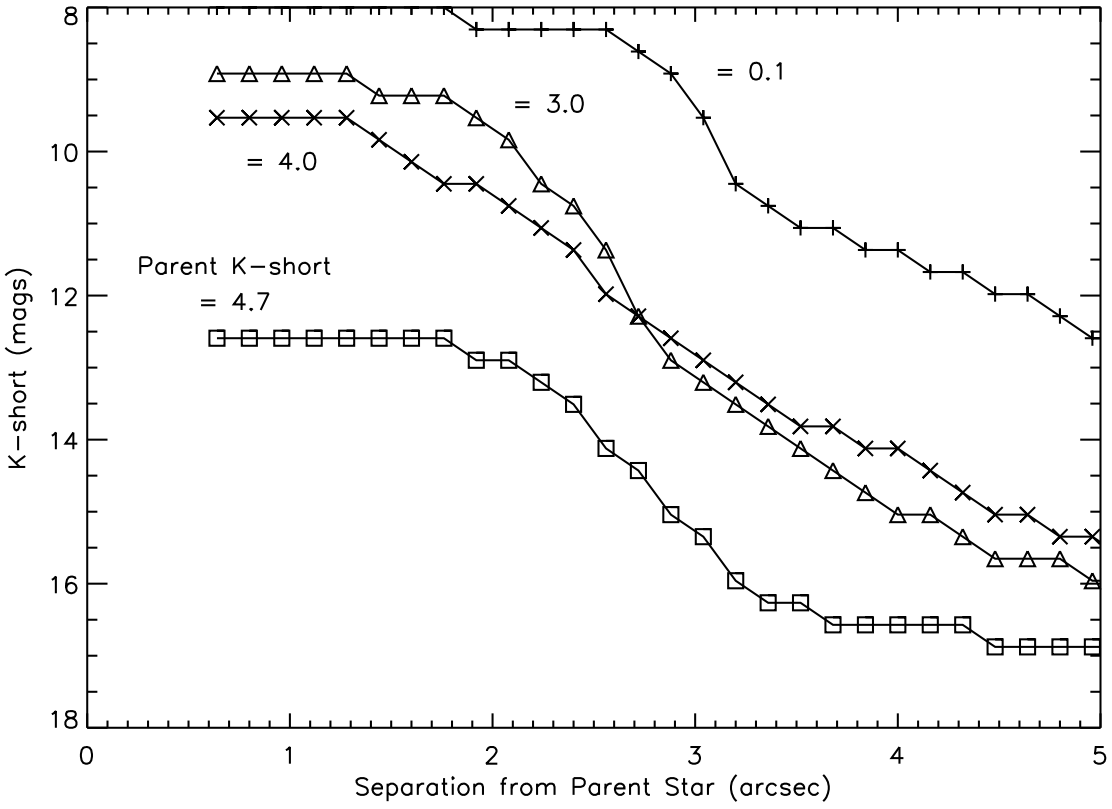

Figure 3.9: K_s-band sensitivity curves displaying limiting magnitude as a function of separation from the parent star. Individual plots represent curves derived from CHAOS data for Gliese 638 ($K_s = 4.7$), Gliese 75 ($K_s = 4.0$), Gliese 222 ($K_s = 3.0$), and Gliese 768 ($K_s = 0.1$). Limiting magnitudes represent 5-sigma detections in $\sim$ 5-minute integration times.

Table 3.1: CHAOS Target Sensitivities

	Faintest Detectable Apparent K_s-magnitude by Separation			
Target Name	0.″96	1.″92	3.″04	4.″96
Gliese 53	8.6	10.4	13.5	15.3
HIP 109119	13.2	14.1	16.6	16.6
Gliese 809	10.8	12.3	15.3	16.9
Gliese 15	12.6	13.2	16.6	18.7
HIP 111313	16.0	16.0	16.3	16.3
Gliese 846	12.3	12.9	15.7	16.6
Gliese 27	10.4	11.1	13.2	15.7
Gliese 144	11.4	12.0	14.7	17.2
Gliese 49	11.7	11.7	14.7	16.3
Gliese 908	17.5	17.5	17.5	17.8
Gliese 33	11.4	11.7	14.7	16.9
HIP 73470	8.9	10.8	13.2	14.7
HIP 54646	11.1	11.7	14.4	16.0
HIP 68184	11.4	12.0	14.4	16.6
HIP 98698	16.0	16.0	16.0	16.3
Gliese 638	12.6	12.9	15.3	16.9
Gliese 411	12.3	12.9	15.3	17.5
Gliese 434	9.5	10.4	12.6	15.3
Gliese 653	8.0	8.3	11.1	13.2
Gliese 631	8.0	8.6	11.4	14.1

Table 3.1: (Continued)

	Faintest Detectable Apparent K_s-magnitude by Separation			
Target Name	0.″96	1.″92	3.″04	4.″96
Gliese 488	9.2	9.8	12.3	14.7
Gliese 536	8.6	10.1	12.6	15.3
Gliese 675	8.9	9.5	12.0	14.4
Gliese 740	8.6	9.5	12.3	15.0
Gliese 514	12.3	12.6	15.3	17.8
Gliese 75	9.5	10.4	12.9	15.3
Gliese 172	10.4	11.7	14.7	16.3
NN3371	11.7	12.3	14.7	16.0
Gliese 273	13.2	15.0	18.1	19.0
Gliese 222	8.9	9.5	13.2	16.0
Gliese 183	15.0	15.0	15.3	15.7
Gliese 124	8.0	8.0	9.2	12.6
Gliese 212	11.7	12.0	13.5	13.5
Gliese 169	9.2	9.2	11.7	14.4
Gliese 848	15.0	15.0	15.7	16.0
Gliese 69	9.8	10.1	12.0	15.7
Gliese 92	8.0	8.0	11.4	14.1
Gliese 892	12.0	12.9	16.6	17.8
Gliese 752	11.4	12.0	15.0	16.9
Gliese 673	10.4	11.4	14.4	16.0

Table 3.1: (Continued)

	Faintest Detectable Apparent K_s-magnitude by Separation			
Target Name	0.″96	1.″92	3.″04	4.″96
Gliese 41	15.3	15.3	15.3	15.3
Gliese 324	8.9	9.2	12.3	14.4
Gliese 380	13.8	14.4	16.6	17.5
Gliese 211	13.5	13.8	14.1	14.7
Gliese 166	16.3	16.3	16.3	16.3
Gliese 31.4	13.5	13.5	13.5	13.5
Gliese 349	10.8	11.4	13.8	15.7
Gliese 205	16.6	16.6	16.6	16.9
gj2066	15.7	15.7	16.0	16.0
Gliese 327	14.4	14.7	15.0	15.0
Gliese 526	14.4	15.3	18.1	18.7
Gliese 475	12.9	13.5	16.3	17.5
Gliese 424	13.8	14.7	17.2	18.7
Gliese 764	10.8	12.0	14.7	17.8
Gliese 388	8.3	8.6	10.8	11.1
Gliese 368	11.1	11.7	13.5	13.8
Gliese 412	11.4	11.7	11.7	11.7
Gliese 395	14.7	15.0	15.0	15.7
Gliese 451	17.5	17.8	18.1	18.4
Gliese 450	12.9	13.2	14.4	14.4

Table 3.1: (Continued)

	Faintest Detectable Apparent K_s-magnitude by Separation			
Target Name	0.″96	1.″92	3.″04	4.″96
Gliese 534	12.6	12.6	12.6	12.9
Gliese 502	9.5	9.8	12.0	14.7
Gliese 549	13.8	14.1	14.4	14.7
Gliese 390	12.0	13.2	14.7	16.0
Gliese 449	8.0	8.0	11.1	13.5
Gliese 408	17.8	17.8	17.8	17.8
Gliese 567	16.6	16.6	16.6	16.6
Gliese 603	10.4	10.8	13.5	15.7
Gliese 644	10.4	11.1	14.4	16.3
Gliese 678	14.1	14.1	14.1	14.4
Gliese 768	8.0	8.3	9.5	12.6
Gliese 807	8.0	8.0	10.1	12.6
Gliese 706	11.1	12.0	15.0	16.9
Gliese 699	14.7	15.3	18.1	19.3
Gliese 617	12.0	12.3	15.7	16.9
Gliese 688	15.3	15.3	15.3	16.0
Gliese 695	8.3	8.9	10.8	13.8
Gliese 654	15.7	15.7	15.7	15.7
Gliese 598	8.0	8.3	12.3	14.7
HIP 113421	13.2	13.2	13.2	13.2

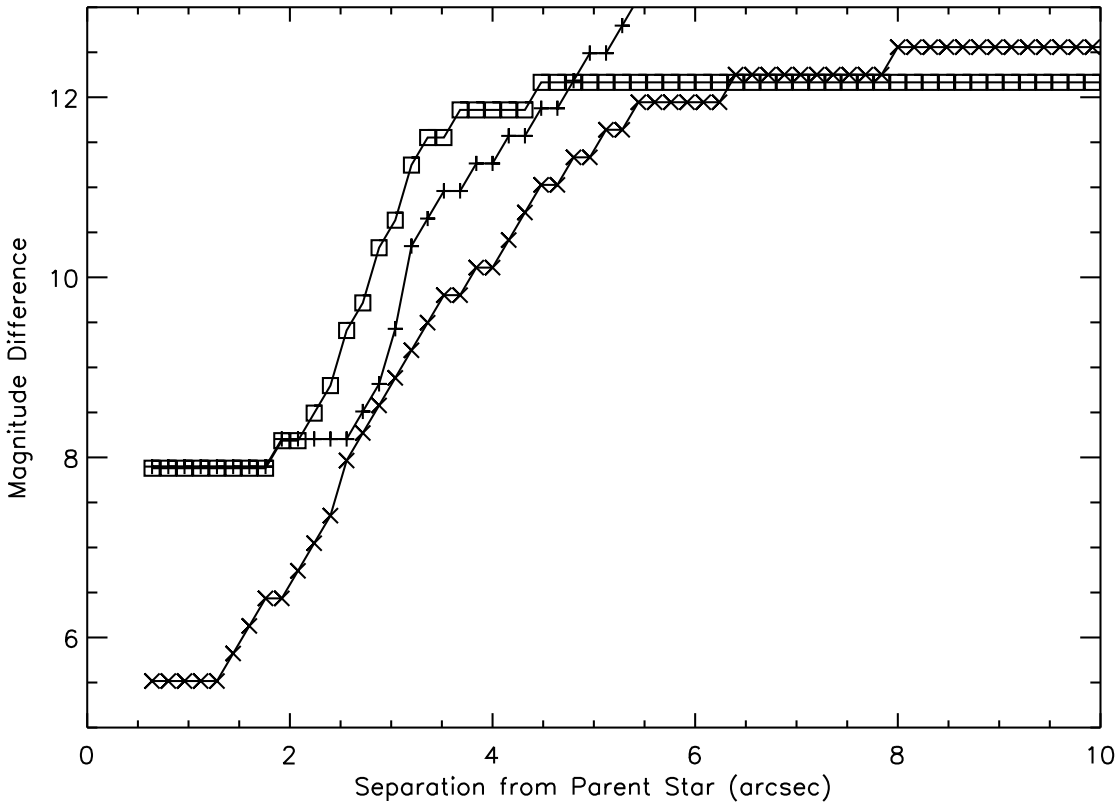

Figure 3.10: K_s-band sensitivity curves displaying limiting differential magnitude (K_s-companion minus K_s-parent) as a function of separation from the parent star. Individual plots represent curves derived from CHAOS data for Gliese 638 (K_s = 4.7), Gliese 75 ($K_s = 4.0$), Gliese 222 ($K_s = 3.0$), and Gliese 768 ($K_s = 0.1$). Limits represent 5-sigma detections in $\sim$ 5-minute integration times. Curve symbols are consistent with those used in Figure 3.9

Chapter 4

CHAOS Population Simulations

4.1 Introduction

To conclude our CHAOS survey, we perform a population synthesis analysis of the survey results. Using a likelihood analysis approach combined with Monte Carlo simulations, we determine the upper limit to the fraction of stars with brown dwarf companions to be 9.7% for the 25-100 AU semi-major axis region. Taking these results into account, we conclude that the brown dwarf desert described by Marcy and Butler for narrow separations ($<$ a few AU in semi-major axis values) continues, at some level, through the 25-100 AU regime. In the sections below we provide detailed descriptions of our techniques and conclusions, along with comparisons to other groups' procedures and results.

4.2 The Mathematics of Our Likelihood Analysis Approach

Our Likelihood Analysis approach seeks to answer the question: How consistent is a hypothetical brown dwarf companion population with our observed results? To answer this question, we begin by defining two parameters, θ and ϕ, which represent vectors describing all of the parameters of our brown dwarf population. ϕ describes the fraction of stars with brown dwarf companions. θ represents all other population parameters including brown dwarf masses, brown dwarf luminosities, orbital radius distributions, etcetera. Next we note that, for each star, we have a measurable probability of detecting a given luminosity brown dwarf. This probability depends on D, distance to the system, L_*, luminosity of the parent star, r, projected orbital separation, and I, instrumental parameters. I includes factors such as throughput, exposure time, PSF stability, etcetera. For a given star, therefore, we may write the probability of a brown dwarf detection as:

$$P_{detection} = P(\phi, \theta, D, L_*, I) \tag{4.1}$$

Since we detected no brown dwarf companions in our survey, we may write that, for the j-th observed star, the number of expected detections is $\mathcal{N}_j = P_{detection-j} \ll 1$. Poisson statistics then dictate that the probability of detecting k brown dwarfs around a given star is:

$$\mathcal{P}_k = \frac{\mathcal{N}^k}{k!} e^{-\mathcal{N}} \tag{4.2}$$

Since we detected zero brown dwarfs, we seek to determine a likelihood for $k = 0$. Taking the product of $P_{detection}$ over all 80 sampled stars, with k=0, we may

derive the following likelihood equation:

$$\mathcal{L}(\phi, \theta, D, L_*, I) = \prod_{j=1}^{80} e^{-\mathcal{N}_j} \tag{4.3}$$

Recall that ϕ = fraction of stars with brown dwarf companions; θ = all other brown dwarf population parameters (mass, luminosity, orbital radius, etcetera); D = distance to target system; L_* = luminosity of the parent star; I includes instrument parameters such as exposure time and throughput; $\mathcal{N}_j$ = number of expected detections around the j-th star. Our relation here therefore represents the likelihood of making zero detections through 80 observations of a brown dwarf companion population represented by θ and ϕ. D, L_*, and I are all measurable values that we define for each observing set. Hence, they are factors included in $\mathcal{N}_j$. For the purposes of a straightforward analysis, we shall set θ to sample test populations. We shall then let m_j equal the segment of $\mathcal{N}_j$ which includes all parameters except for ϕ. In other words, $\mathcal{N}_j = \phi m_j$. Substituting this relation into equation 4.3 we now have

$$\mathcal{L}(\phi) = \prod_{j=1}^{80} e^{-\phi m_j} \tag{4.4}$$

We note here that this analysis assumes that each star has a maximum of one orbiting brown dwarf. A star with two brown dwarf companions would therefore be treated, statistically, as there being two stars in the sample which each possessed a brown dwarf companion. This type of treatment takes precedent in population statistical studies such as Tokovinin (1992). We recommend that the reader refer to that publication for a further discussion of such a technique.

For our final analysis, we choose a 90% confidence level for our conclusions. Therefore, we seek to find the range of ϕ values which yield a null detection (through

80 observations) 90% of the time. Clearly, $\phi = 0$ will be the lower limit for ϕ. ϕ_u represents the upper limit to the number of stars with brown dwarf companions. Combining these facts with equation 4.4, we may derive the relation:

$$0.9 = \frac{\int_0^{\phi_u} e^{-\phi(m_1+m_2+\cdots+m_{80})} d\phi}{\int_0^{\infty} e^{-\phi(m_1+m_2+\cdots+m_{80})} d\phi} \tag{4.5}$$

Solving for ϕ_u, we get the simple equation:

$$\phi_u = \frac{-ln(0.1)}{m_1 + m_2 + \cdots + m_{80}} \tag{4.6}$$

In the next section, we describe how we may use Monte Carlo simulations to evaluate the m_j values in equation 4.6.

4.2.1 Sampled Brown Dwarf Orbits

Practically, our Monte Carlo simulations operate by sampling through a databank of brown dwarf model orbits. In this databank, each array represents a unique combination of orbital parameters. With dimensions equivalent to those of our noise maps (see section 3.5.1), the arrays' nonzero pixel values represent detector positions that the orbiting brown dwarf occupies sometime during its orbit. The pixels' individual values represent the fraction of the total orbital period that the brown dwarf spends occupying that pixel. The complete orbit databank samples semi-major axes from 4 to 7000 pixels (at 1 pixel intervals), inclinations from 0 to 90 degrees (at 10 degree intervals), eccentricities from 0 to 0.9 (at 0.1 intervals), and longitudes of pericentre from 0 to 90 degrees (at 10 degree intervals). While our Monte Carlo simulations sample over all mentioned values of inclination, eccentricity, and longitude of pericentre, they do not sample the complete 4 to 7000 pixel semimajor

axis range. Rather they select semi-major axis values ranging from 5 to 900 AU (at log[AU] intervals $\sim$0.03) and convert to the appropriate pixel values according to the target system's distance.

4.2.2 Combining Theoretical Brown Dwarf Orbits with Observational Noise Maps and Potential Brown Dwarf Magnitudes

The simulation starts by selecting an apparent K_s-magnitude and semi-major axis and converting these values into detector counts and distance in pixels, respectively. (See section 3.5.2 for a description of sampled apparent K_s-magnitudes and the conversion to detector counts.) Next the simulation looks to the target's composite noise map and identifies all pixel positions where the K_s-magnitude signal fails to exceed the combined Poisson and noise map noise by a factor ≥ 5. Identifying all arrays from the orbit databank that correspond to the selected semi-major axis (including all combinations of inclination, eccentricity, and longitude of pericentre), it sets all of those positions on the orbit arrays equal to zero. It then sums all of the pixels in all of the selected orbit arrays and divides by the number of orbital arrays. The final value represents the probability, for that given target star, of detecting an orbiting brown dwarf (assumed to be existent) with the given apparent K_s-magnitude and semi-major axis. We determine such a value, corresponding to m_j in section 4.2, for all target systems over all sampled semi-major axes and apparent K_s-magnitudes. Using equation 4.6, we can then evaluate a ϕ_u for each hypothetical apparent K_s-magnitude and semi-major axis.

4.3 Population Simulation Results

In our discussion of the population simulation results we address three questions: (1) What are the sensitivity levels of our survey with regards to physical population characteristics (i.e. absolute magnitudes, semi-major axes, brown dwarf masses, etcetera)? (2) What population upper limits may we derive from our simulation results? (3) How do our population analysis techniques and results compare with other brown dwarf companion population studies? With regards to the first question, we describe that our simulation results and analysis reveal that our survey is most sensitive to brown dwarfs orbiting with semi-major axes ranging from 25-100 AU. Given our sensitivity limits, our survey should detect 30% of all 10-73 Jupiter mass objects in this semi-major axis regime. From our population upper limit analysis we derive that, with a 90% confidence level, **at most 9.7% of our target stars possess brown dwarf companions with semi-major axes between 25 and 100 AU**. Compared to radial velocity brown dwarf companion statistics like Marcy & Butler (2000), our results are consistent with the brown dwarf desert described within a few AU of stars. Furthermore, while our results suggest that a brown dwarf desert continues through the 25-100 AU region, they cannot verify or contradict the extreme brown dwarf paucity measured at radial velocity separations. Our results are also consistent with brown dwarf companion populations derived by McCarthy & Zuckerman (2004) and Gizis et al. (2001a). However, we note that significant errors in their analyses must be addressed before a useful comparison can be made.

4.3.1 Survey Sensitivities

In section 3.5 we described our survey sensitivities in terms of observational characteristics such as apparent magnitude and angular separation from the parent star.

Deriving population statistics however, relies on a formulation of survey sensitivities in terms of physical characteristics such as brown dwarf mass and semi-major axis. Our Monte Carlo simulation outputs provide the basis for these formulations. Recall that in section 4.2.2 we stated that our Monte Carlo simulations output detection odds for each semi-major axis and brown dwarf apparent K_s-magnitude. Since semi-major axis is already a physical characteristic, we just need to transform, for each target system, our apparent K_s-magnitudes into corresponding brown dwarf masses. We may then take an average (weighted according to mass function), for each target system semi-major axis, of all the apparent K_s-magnitudes' detection odds. We then average over all target systems to arrive at a plot of survey detection odds versus semi-major axis. In the text below I describe these procedures in greater detail.

We begin our task by first converting all apparent K_s-magnitudes to absolute K_s-magnitudes using the parallaxes given in Table 2.1. Converting from absolute K_s-magnitude to brown dwarf mass requires a knowledge of the brown dwarf age. For the quarter of the target stars with published Fe/H line strengths (see Table 2.2), we may estimate an age using equation 2.1. We may then input age and apparent K_s-magnitude into evolutionary models by Burrows et al. (2001) to determine a brown dwarf mass. At this point we should be able to calculate, for each target star with published Fe/H line strengths, a detection probability for every brown dwarf mass at every semi-major axis. To consolidate our mass values, we take a weighted average over all brown dwarf masses' detection odds (truncating anything with masses outside of 10-73 M_{Jup}) according to the following mass function by Chabrier (2001).

$$\zeta(logm) = A * exp[-\frac{[log(m) - log(m_0))^2}{2\sigma^2}] \tag{4.7}$$

$\zeta(logm)$ is the number of objects with mass $log(m)$ (m is measured in units of $M_\odot$); A is a constant which, in our case, will depend on the fraction of stars with brown dwarf companions; σ depends on the mass regime we are examining (i.e. B stars, G stars, brown dwarfs, etcetera), which for our case best approximates to 0.627; m_0 is a characteristic mass which also depends on the mass regime. In our case it approximates to $0.1M_\odot$ (See Chabrier 2001 for a more detailed explanation of the best σ and m_0 values for various mass regimes.)

At this point we should have a plot of detection odds versus semi-major axis for each star with published Fe/H line strengths. For the three fourths of the target stars with no estimatable ages, we assign to them random ages, but with a combined median and standard deviation equal to those of the Table 2.2 stars. We then use the aforementioned procedures to arrive at plots of detection probability versus semi-major axis. Finally, we average the complete sample of detection odds versus semi-major axis plots to get a single plot describing survey sensitivities. In order to ensure that our randomly assigned ages are not creating unrealistic results, we repeat the above procedures several dozen times using a different random sample of ages each time. The different outcomes are then averaged to produce the plot shown in Figure 4.1.

4.3.2 Population Upper Limits

To arrive at brown dwarf companion population upper limits, we combine the sensitivity data from the previous section with equation 4.6. In equation 4.6, m_j represents the detection odds (as defined in Figure 4.1 and the accompanying caption) for a given star and a given brown dwarf semi-major axis. Using the procedures described in the previous section, we may calculate such a value for each star and

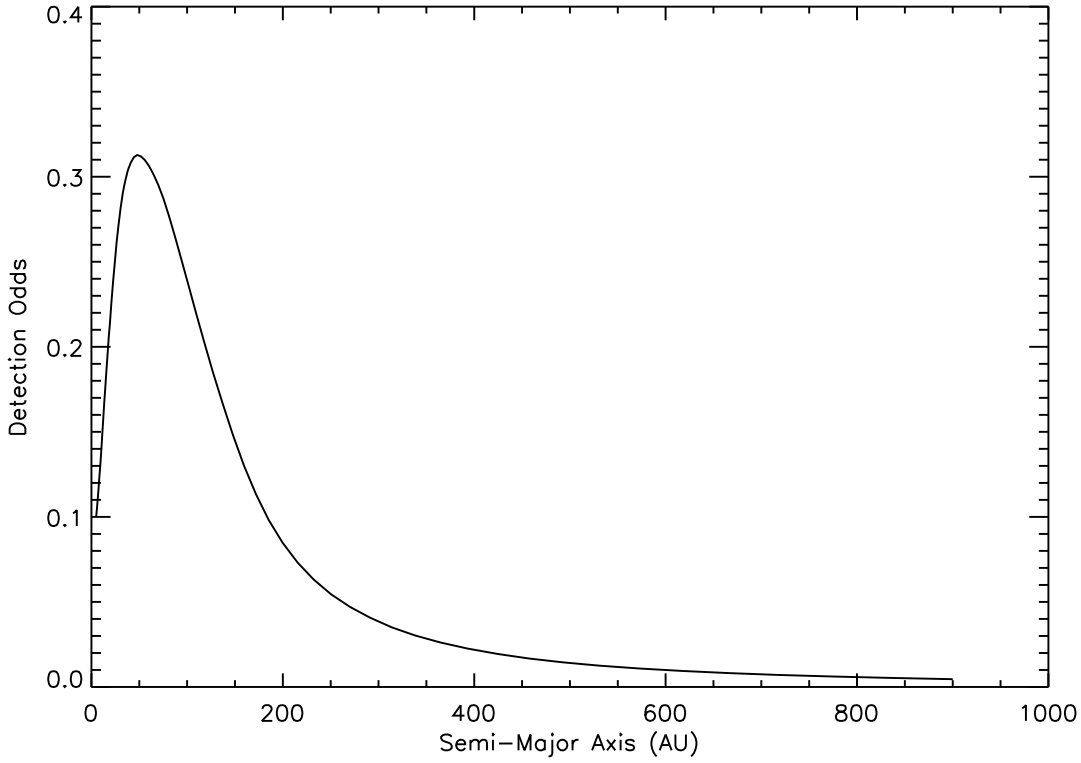

Figure 4.1: CHAOS survey sensitivity plot as a function of brown dwarf semi-major axis. The y-axis represents the survey's odds of making a 5-sigma brown dwarf companion detection around a given star, assuming a single orbiting brown dwarf. Potential brown dwarf masses range from 10 to 73 Jupiter masses. The odds of the brown dwarf being a given mass in this regime were weighted according to the initial mass function described by Chabrier (2001), equation 7. We assume a random orientation for brown dwarf orbital inclination, eccentricity, and longitude of pericentre. Brown dwarf ages were estimated from parent star Fe/H line strengths according to the procedure described in section 4.3.1.

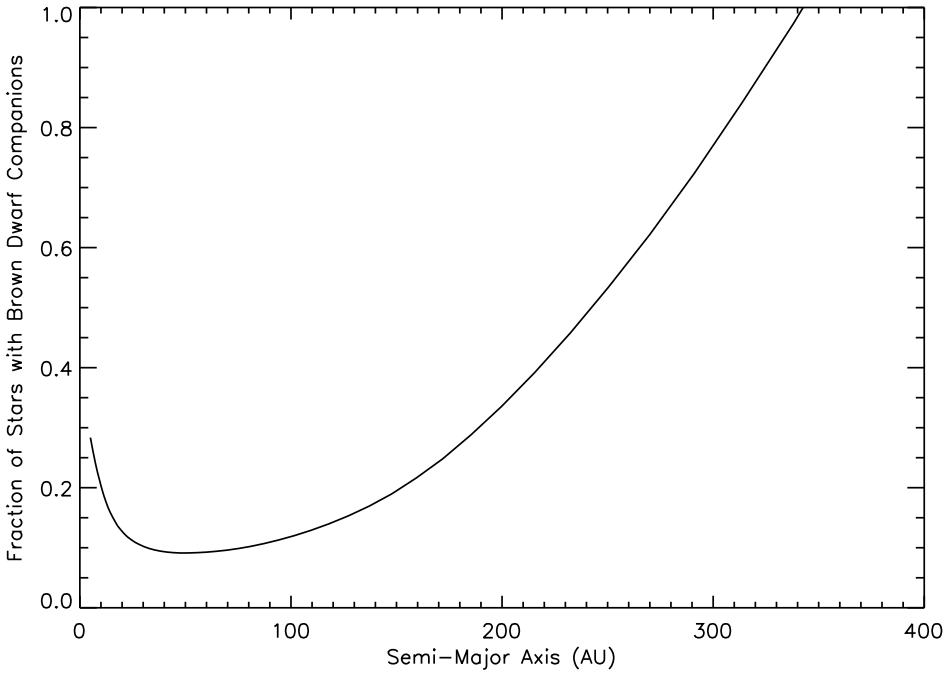

Figure 4.2: Brown dwarf companion population upper limits. This plot represents the upper limit to the fraction of stars with brown dwarf companions given as a function of brown dwarf semi-major axis. The upper limit curve entails a 90% probability based on the Monte Carlo simulations described in section 4.3. Results are based on a minimum 5-sigma detection of potential brown dwarf candidates in the CHAOS survey.

each sampled semi-major axis. We input these values into equation 4.6 to determine a population upper limit (corresponding to the number of brown dwarf companions per surveyed star) for each semi-major axis value. Figure 4.2 displays the results of such an analysis. From the plot we see that our survey is most sensitive to semi-major axes ranging from about 25 to 100 AU; The plot indicates that, at a 90% confidence level, at most 9.7% of CHAOS targets have a brown dwarf companion between 25 and 100 AU.

Effects of Brown Dwarf Eccentricity on Population Results

A biased brown dwarf eccentricity may alter results by causing typical projected separations to differ significantly from actual semi-major axes. To take the possibility of a biased eccentricity into account, we examine the effect that different eccentricity selections will have on our calculated brown dwarf upper limits. Unfortunately, our Monte Carlo simulations output results which clump together all possible eccentricities (randomly distributed between 0.0 and 0.9) into one statistical average. Rather than re-running our CPU-intensive simulations with decoupled eccentricities, we tested how upper limit changes when we extrapolate populations from a single system observation with different hypothetical eccentricities. While the absolute companion upper limits represented on these curves may differ from a test that includes the entire sample, the incremental effect of a changing eccentricity should be indicative of the effects on the entire survey sample. Figure 4.3 displays brown dwarf upper limits for eccentricities of 0.0, 0.9, and randomly distributed values. The upper limits for the plot were calculated using the same procedures as Figure 4.2 except that we assume that the detection probability maps (like the one shown in Figure 4.1) for all eighty systems are identical to the one calculated for Gliese 15. We note that upper limit values with semi-major axes corresponding to low detection probabilities (say $< 10\%$) are poor representations of the complete survey. This results from the fact that regions with low sensitivities exhibit upper limit values with a high dependency on individual observing conditions. However, for upper limit values with better sensitivities, the incremental changes between curves with different eccentricities should be representative of eccentricity's effect on the complete population results. In the case of Gliese 15, where sensitivity peaks between 10 and 60 AU, we see calculated upper limit values in this region increase

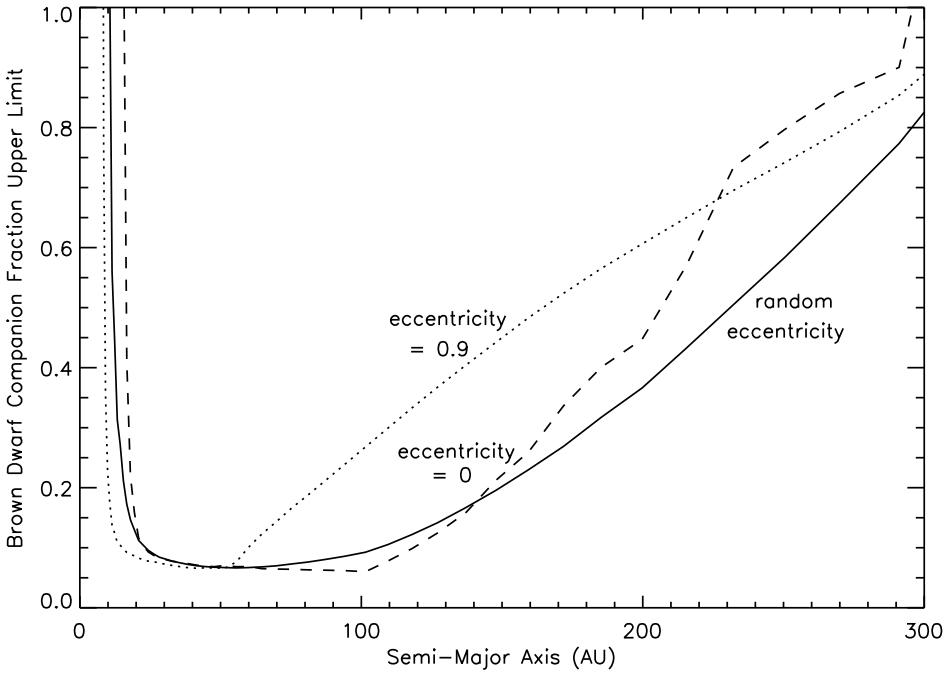

Figure 4.3: Comparison of upper limit curves created with different brown dwarf orbital eccentricities. The y-axis values values represent survey upper limit values when all target sensitivities are all equal to those of Gliese 15. Such an extrapolation deviates substantially from a complete version (which takes into account each observing set's sensitivity levels) for semi-major axis values corresponding to low (like $< 10\%$) detection probability values. However, in regions where sensitivity peaks (for the case of this star, from about 10 to 60 AU), fractional changes in upper limit values between different eccentricity curves should be indicative of eccentricity's effect on the complete survey results.

by a factor of 1.56 between random eccentricity values and an eccentricity value of 0.9. Such an effect indicates that the actual brown dwarf companion population could be significantly higher than our 9.7% upper limit, should the typical brown dwarf eccentricity be significantly biased toward higher values.

Effects of Stellar Ages on Population Results

The upper limit plots in the previous section rely on an accurate knowledge of typical system ages. If the actual median system age is significantly lower than this,

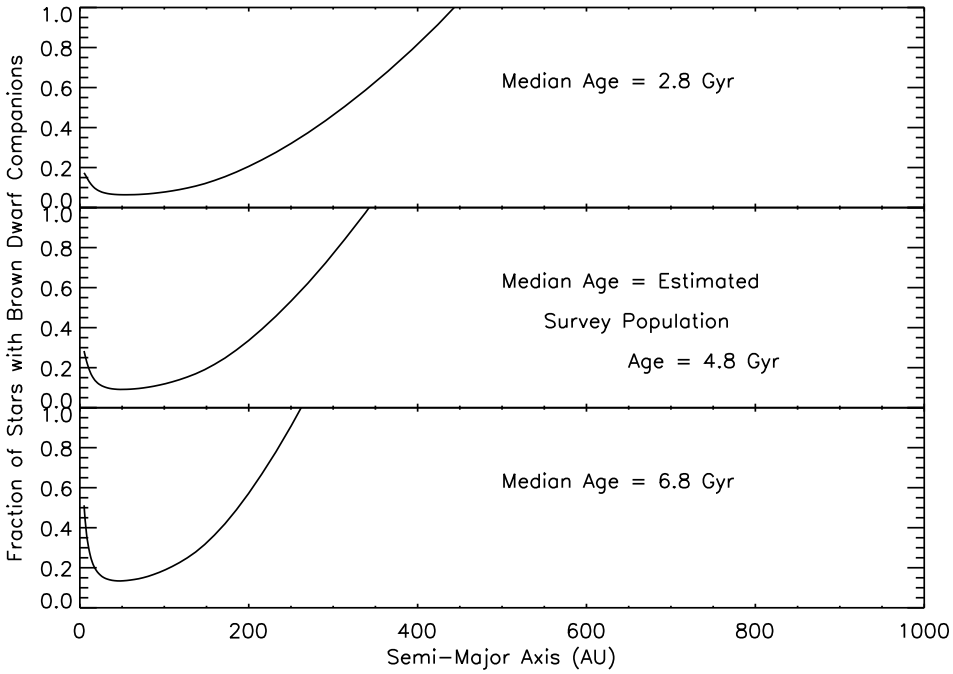

Figure 4.4: Comparison of upper limit curves created with different system ages. The central plot here represents the plot shown in Figure 4.2. The plots above and below represent the same scenario as the central one, only the median system age has been shifted by ±2 Gyrs.

our sensitivities to a given brown dwarf mass are actually better than we predicted, and the true upper limit is in fact lower. If the median system age is in fact larger than we predicted, the true upper limit will be higher. To examine how such mis-estimations may change our conclusions, we consider instances when the median population age is 2 Gyrs older or 2 Gyrs younger than the median age we used. Figure 4.4 shows a comparison of such modified instances along with our original estimated 4.8 Gyr median population age. For the 25-100 AU range, a change of positive and minus 2 Gyrs alters the original calculated upper limit of 9.7% by a multiple of 1.49 and 0.70 respectively. These values illustrate the errors in upper limits that would be introduced should we find that our age estimates are incorrect.

Effects of Minimum Brown Dwarf Masses on Population Results

While published brown dwarf searches have discovered many larger-mass field and companion brown dwarfs, very few detections have been made of lower mass brown dwarfs. This likely attributes solely to the fact that these smaller masses are fainter and more difficult to detect. Conventional wisdom dictates that these undetected smaller mass brown dwarfs should be as or more abundant than larger brown dwarfs. However, purely observational surveys have failed to confirm or negate this speculation. Therefore, we consider the possibility that typical brown dwarf populations have an effective cutoff at some mass greater than the 10 M_{Jup} we have considered. Figure 4.5 describes how different effective cutoffs would alter our upper limit estimates. From these plots we see that our calculated upper limits are not strongly affected by changes in the minimum brown dwarf mass. For example, a change in the brown dwarf minimum mass from 10 M_{Jup} to 40 M_{Jup} only changes our calculated upper limit by about 1%. This result might seem counter-intuitive to the reader since a 40 M_{Jup} brown dwarf should be significantly easier to detect than a 10 M_{Jup} brown dwarf. However, we remind the reader that our uncertainties are influenced by a number of factors including mass function, orbital parameters, system age, and observing conditions, to name a few. As a result, our upper limits remain relatively loosely constrained even when we only consider brighter, higher mass brown dwarfs.

Effects of the Brown Dwarf Mass Function Shape on Population Results

Our calculated population upper limits assume that the brown dwarf mass function has a shape described by equation 4.7. We consider here the effect of a changing mass function slope on our population upper limits. We begin with the equation 4.7 mass function plot displayed in the middle-left of Figure 4.6. We then add a linear

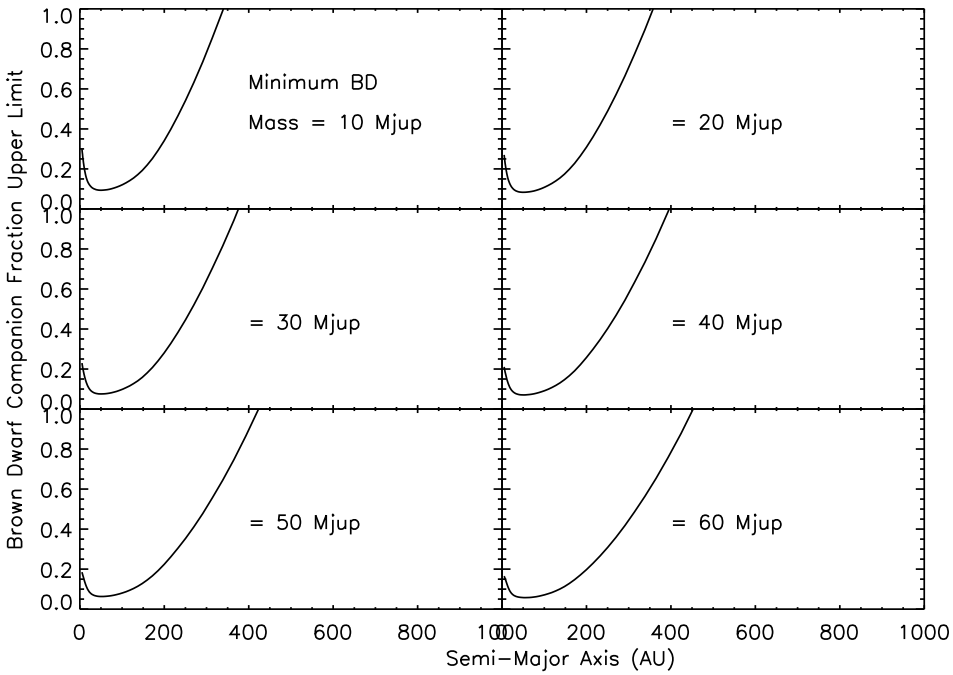

Figure 4.5: Comparison of upper limit curves created with different minimum brown dwarf masses. These plots represent the equivalent of the Figure 4.2 plot only we have set the minimum brown dwarf population mass equal to different test values.

slope of ±30 degrees to arrive at the mass functions shown immediately above and below that plot. More specifically, our added "slopes" are functions with the forms *y=0.577x-23.9* and *y=-0.577x+23.9*, where x = brown dwarf mass (M_{Jup}) and y = number of brown dwarfs. The adding of these functions has the effect of changing the mass function slope without altering the total area underneath the mass function curve. The three plots on the right in Figure 4.6 represent the corresponding upper limit curves for each of the mass functions. An inspection indicates that our upper limit results are not terribly sensitive to errors in our assumption of the shape of the brown dwarf mass function. For instance, a change in slope of a full 60 degrees results in a change in the brown dwarf population upper limit of only a few percent. Therefore, our upper limit results should still be valid despite any future small changes (say 10 degrees or so) in our knowledge of the brown dwarf mass function shape.

4.4 Companion Population Results by Other Authors

In the following sections we show how our results and techniques compare with companion population studies performed by Marcy & Butler (2000), McCarthy & Zuckerman (2004), Gizis et al. (2001a), Fischer & Marcy (1992), and Duquennoy & Mayor (1991). We divide these studies into three categories: Substellar Companion Radial Velocity Searches, Substellar Companion Imaging Searches, and Stellar Companion Searches.

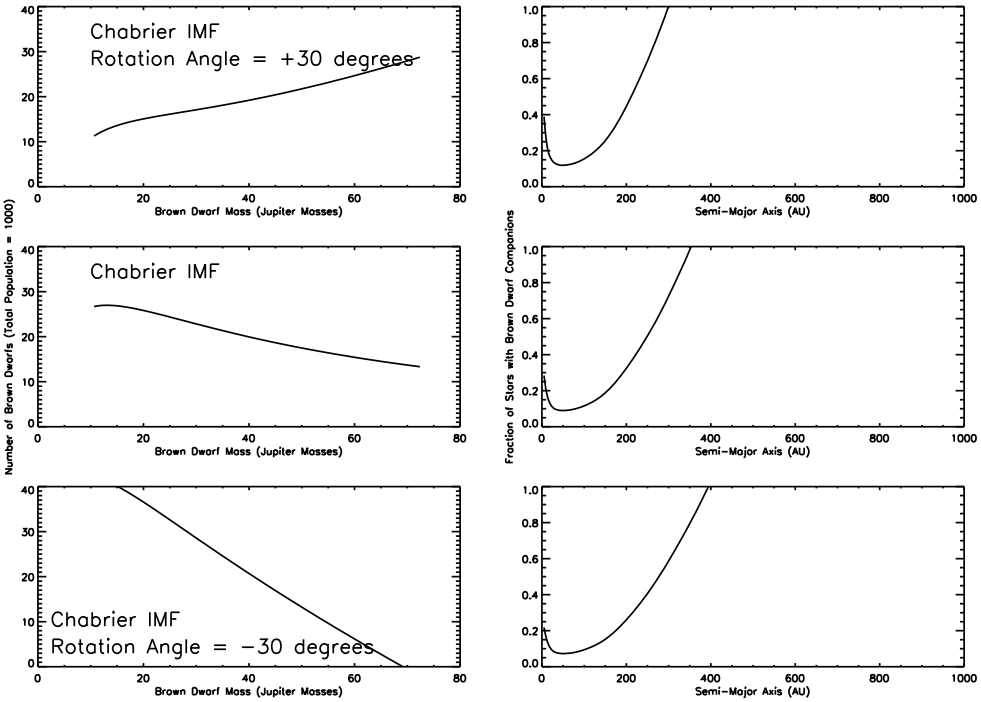

Figure 4.6: Comparison of Upper Limit Curves Created with Different Brown Dwarf Mass Functions. The three plots on the left represent three brown dwarf mass functions: (1) the mass function described in equation 4.7, but with an introduced slope of +30 degrees, (2) the original equation 4.7 mass function, and (3) the equation 4.7 mass function shifted by -30 degrees. The three plots on the right represent the corresponding brown dwarf population upper limit for each of the sample mass functions. The upper limit plots were created using the same procedures as those for Figure 4.2, but using the appropriate mass function.

4.4.1 Substellar Companion Radial Velocity Searches

Radial velocity extrasolar planet searches like Marcy & Butler (2000) have been very effective at detecting companions at close separations (like < 6 AU) to parent stars. At the time of this writing, http://exoplanets.org (managed by the California & Carnegie Planet Search) compiles 110 substellar objects detected via this technique. Using a radial velocity probe, Marcy & Butler (2000) report that less than 0.5% of F-M stars have brown dwarf companions (down to 11 M_{Jup}) with semi-major axes $\leq$3 AU. From our results, we cannot speculate whether these statistics continue through the 25-100 AU region. We can however state that our values are consistent with their population numbers. Furthermore, in agreement with the Marcy & Butler (2000) description of a "brown dwarf desert," our upper limits do suggest that the 25-100 AU companion population is most consistent with a drop-off in brown dwarf companions, as compared to the stellar companion population. (See section 4.4.3 for a more complete discussion of the comparitive stellar companion population.)

4.4.2 Substellar Companion Imaging Searches

In the last decade, an abundance of brown dwarf companion imaging surveys has arisen. Wide-field surveys such as the Two Micron All Sky Survey (2MASS; Skrutskie et al. 1997) and the Deep Near Infrared Survey (DENIS; Epchtein et al. 1997) have received particular attention as data miners and follow-up observers have confirmed a number of wide separtion brown dwarf companions (Wilson et al. 2001 and Kirkpatrick et al. 2001, for example). Unfortunately, the number of corresponding companion population statistical studies remains quite slim. At the time of this writing, we are aware of only two such companion population estimate from imaging surveys: McCarthy & Zuckerman (2004) and Gizis et al. (2001a). In the

paragraphs below we discuss each of these population results and their agreements or disagreements with our population study.

McCarthy & Zuckerman

McCarthy & Zuckerman (2004) take advantage of a Keck coronagraphic study to compute brown dwarf companion population numbers for semi-major axis values ranging from 75 to 300 AU. They report the frequency of brown dwarf companions to young G, K, and M stars in this region to be 1% ± 1%; Using Lick and Steward observations with Keck follow-up, they determine a >30 M_{Jup} brown dwarf frequency at the 120-1200 AU semi-major axis region to be 0.7% ± 0.7%. While these population numbers are consistent with our results, we show here that systematic errors in their analysis lead them to conclude results which are inconsistent with their observational data. We therefore strongly oppose the inclusion of such population estimates in an accurate summary of brown dwarf companion populations. For the purpose of comparison though, we describe the differences between their approach and our approach, along with a sample analysis of our data using their analysis techniques.

Rather than taking a Monte Carlo approach, McCarthy & Zuckerman (2004) rely on a probability analysis given in McCarthy (2001), p. 67 and the Appendix of Burgasser et al. (2003b). While the raw mathematical bases of their conclusions are sound in principle, the authors take some significant mis-steps in reaching their conclusions. The greatest fault in their study involves the measurement of brown dwarf semi-major axes without considerations of system inclination or eccentricity (in effect assuming inclination = 0 and eccentricity = 0). Assumptions of zero inclination contradict conventional wisdom regarding stellar orientations, which sees

no reason not to assume an effectively random orbital orientation. Assumptions of zero eccentricity run contrary to statistics compiled by Marcy & Butler (2000) which suggest that brown dwarf orbital eccentricities may in fact be biased toward high eccentricities as we leave the radial velocity regime (this regime being inclusive of perhaps a half-dozen AU). But at the very least, there is little evidence to support the assumption that we should expect brown dwarf orbits to be circular. In Figure 4.7 we display how such assumptions lead to significant errors in sensitivity estimates. There we display two curves derived from our survey data. The solid line curve represents our detection sensitivities as a function of semi-major axis according to Monte Carlo results that assume a random inclination and eccentricity. The dashed line curve represents detection sensitivities derived from the same data set, but with an assumption of inclination = 0 and eccentricity = 0. One sees there that the assumption of inclination = 0 and eccentricity = 0 approach leads to a drastic shift in the survey's predicted sensitivity ranges.

For the purpose of comparison, we shall apply assumptions of zero inclination and eccentricity to our CHAOS data and derive population upper limits using the method described in McCarthy & Zuckerman (2004). To remain consistent with their approach, we shall solely consider the semi-major axis regime 75-300 AU from the parent star. Detecting zero brown dwarfs in this region, McCarthy & Zuckerman conclude from their data that there is at most 1 existent brown dwarf that went undetected. This value of 1 is based on the $\sim$9% chance that the brown dwarf happened to be obscured by the coronagraphic finger which partially obscures the 75-300 region. They then use the following equation to plot the probability function for different physical brown dwarf companion frequencies.

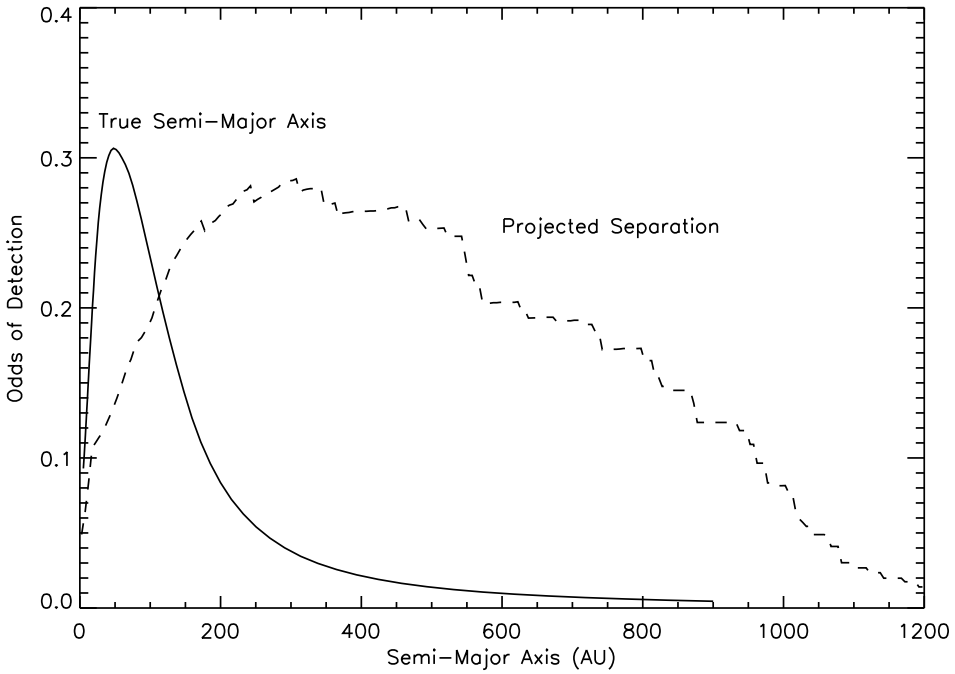

Figure 4.7: Predicted CHAOS detection probability curves using a Monte Carlo and projected separation approach. The dashed line curve represents the estimated detection probabilities of the CHAOS survey when zero inclination and eccentricity are assumed. The solid line curve represents the same data, but with an assumption of random inclination and eccentricity. The comparison illustrates the errors in predicted survey sensitivities that occur when one fails to address inclination and eccentricity properly.

$$P_d(f) = f^d(1-f)^{N-d}\frac{N!}{(N-d)!d!} \tag{4.8}$$

In this equation *P(f)* equals the probability that a survey of N stars will detect d companions when the true frequency of companions is *f*. This equation assumes that the survey is sensitive to all potential brown dwarf companions in the semi-major axis regime. Since the McCarthy & Zuckerman study finds that the true number of brown dwarf companions among their stars is either zero or one, they plot such a result for both d values of 0 and 1. Keeping in the same vein as their analysis, we determine that the CHAOS data admit the possibility that the true number of brown dwarf companions in the 75-300 AU region is between 0 and 12 (twelve brown dwarfs corresponding to a 7% possibility). The missed brown dwarfs would include low mass brown dwarfs falling beneath our detection limits. Figure 4.8 shows the plotted probability functions for CHAOS data with d values ranging from 0 to 6. The curve labeled "Monte Carlo Method" represents an equivalent probability function using our original Monte Carlo simulations and the likelihood analysis approach described in section 4.2. We see here that all McCarthy & Zuckerman functions over-constrain the brown dwarf companion frequency as compared to a more rigorous Monte Carlo approach.

Next we average the McCarthy & Zuckerman plots of CHAOS data for d values ranging from 0 to 12. When averaging, we weight each curve according to the odds of our true physical companion population being equal to that d value. Figure 4.9 shows the resulting composite curve along with the original Monte Carlo computed probability curve. The dotted vertical line designates the region containing 68% of the probability function for the McCarthy & Zuckerman method. This 68% confidence level is used to conclude the 1 ± 1% companion frequency estimates derived in

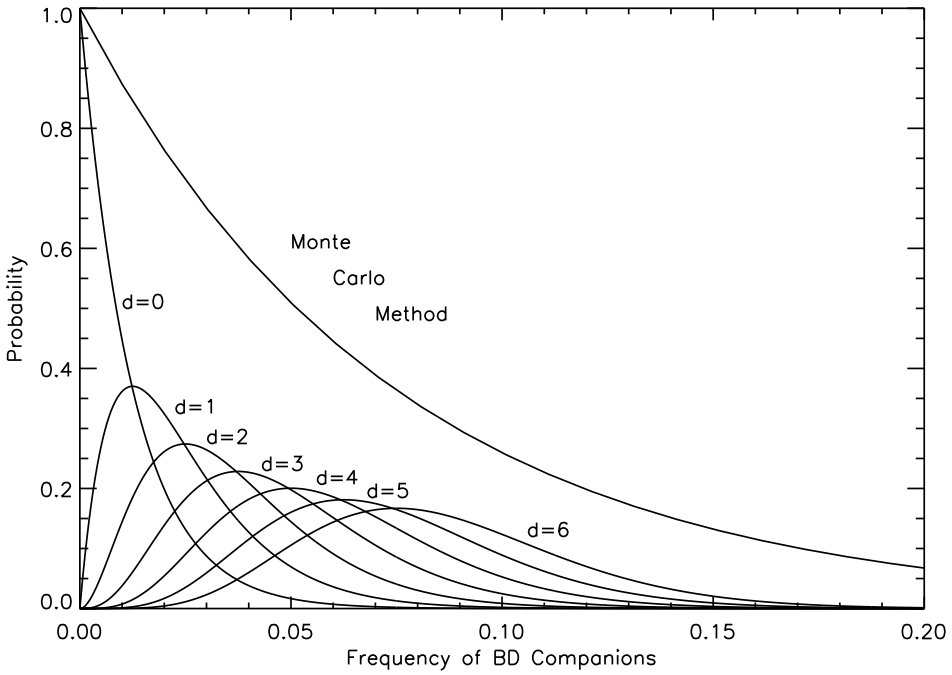

Figure 4.8: Calculated CHAOS brown dwarf companion probability functions computed using the section 4.2 Monte Carlo approach and the McCarthy & Zuckerman (2004) approach. The seven bottom curves represent the McCarthy & Zuckerman method when we assume that the true number of brown dwarf companions in our survey is equal to *d*. Population frequencies cover brown dwarfs with semi-major axis values ranging from 75-300 AU.

McCarthy & Zuckerman (2004). The vertical dashed line represents the region containing 68% of all probabilities when we use the Monte Carlo method. The vertical dot-dashed line represents the Monte Carlo 90% confidence region, corresponding to the 9.7% companion frequency upper limits we published earlier in this chapter. (For the Figure 4.9 case though, the upper limit value is larger since we're calculating over a different semi-major axis region.) Examining these lines we see that, given the same CHAOS data set, a Monte Carlo determined population upper limit of 17.7% (for the 75-300 AU semi-major axis region) would change to 6.3% had we used the McCarthy & Zuckerman method.

Gizis et al.

The Gizis et al. (2001a) population analysis of wide (> 1000 AU) projected separation brown dwarfs is plagued by the same erroneous assumptions of zero inclination and eccentricity. As described in the previous section, these assumptions of zero inclination and eccentricity run counter to conventional wisdom regarding orbital systems. Their survey though is somewhat more forgiving than McCarthy & Zuckerman (2004) since the >1000 AU semi-major axis region is large enough that their population results are less dependent on errors in the systems' estimated semi-major axes. Nonetheless, we show here how their assumptions result in significant errors.

From the mathematical side, Gizis et al. (2001a) rely on the following equation to arrive at their results.

$$f_{bd} = \frac{\rho_{comp}}{\rho_{star}} = \frac{\rho_{comp}}{\rho_{bd}} \frac{\rho_{bd}}{\rho_{star}} = \frac{g_w \rho_{bd}}{\rho_{star}} = \frac{g_w \rho_L}{y_L \rho_{star}} \tag{4.9}$$

In this equation, f_{bd} is the fraction of stars with brown dwarf companions; ρ_{star} is the space density of stars; ρ_{bd} is the space density of field brown dwarfs; g_w is the fraction of the total brown dwarf population that are companions; ρ_{comp} is the

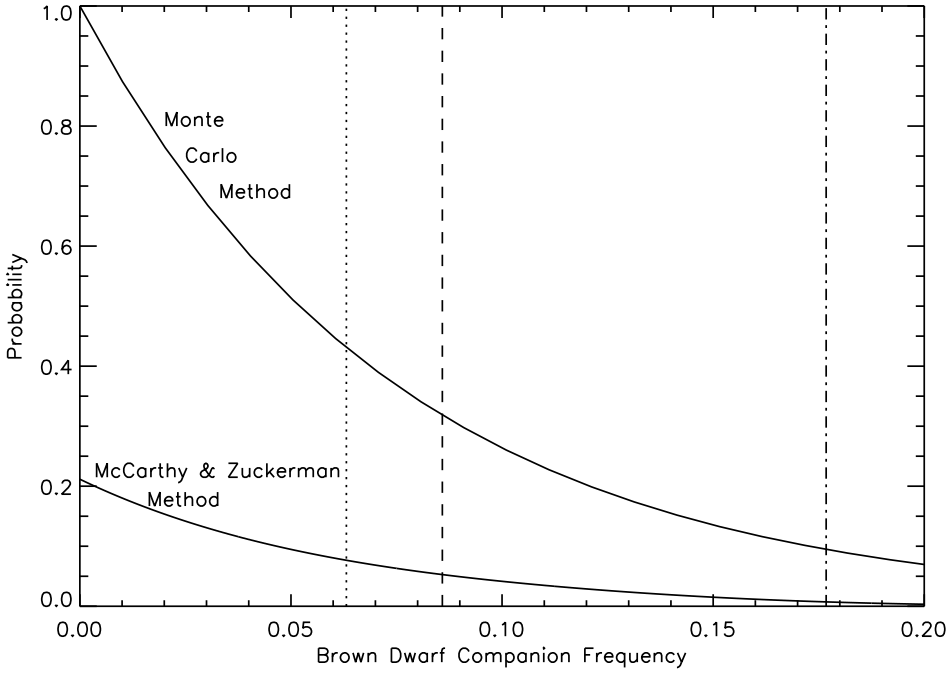

Figure 4.9: Here we plot the probability of different true brown dwarf companion frequencies as concluded from the CHAOS data set. The two curves represent the Monte Carlo method described in section 4.2 and the McCarthy & Zuckerman method described in section 4.4.2. The vertical dotted line delineates the region containing 68% of the McCarthy & Zuckerman probability function. The vertical dashed line designates the region containing 68% of the Monte Carlo probability function. The dot-dashed line represents the region containg 90% of the Monte Carlo probability function. Companion frequencies represent brown dwarfs with semi-major axis values ranging from 75-300 AU. The plot illustrates how, using the same data set, we may alter our Monte Carlo 17.7% upper limit to 6.3% when we instead use the procedures utilized by McCarthy & Zuckerman (2004).

space density of brown dwarf companions; ρ_L is the space density of L dwarfs; y_L is the fraction of brown dwarfs that are L dwarfs. The authors derive g_w, ρ_L, and ρ_{star} from 2MASS data. They estimate y_L from theoretical reasoning. From this technique they conclude that 18% $\pm$ 14% of F-M0 stars have brown dwarf companions with semi-major axes $>$ 1000 AU. While over-simplification of inclination and eccentricity should not significantly affect y_L, ρ_{star}, or ρ_L, it can affect the constraints placed on g_w. For instance, Gizis et al (2001a) conclude nonzero brown dwarf companion populations for semi-major axes $>$ 1000 AU. However, the true $>$1000 AU brown dwarf companion population could still be zero if their detected brown dwarfs happened to have high eccentricities. In that case, the true semi-major axes might be less than the 1000 AU cutoff point.[1]

Conducting a comparitive Gizis et al. (2001a) analysis using CHAOS data is difficult since the utilized data sets are so different. Instead we model how Gizis et al. (2001a) detection odds vary when we introduce non-zero eccentricity and inclination. Figure 4.10 shows the results of our analysis. The solid line labeled "inclination = 0; eccentricity = 0" represents detection odds, as given by Gizis et al. (2001a), for all L dwarfs within the survey volume. Running a small-scale Monte Carlo simulation of brown dwarf companions with projected semi-major axes of 1000-5000 AU, we arrive at the remaining three curves in the plot. When eccentricity equals zero, but inclination is random, their predicted 1000-5000 AU detection levels drop from 100% to 89%. If eccentricity and inclination are both random (with a maximum eccentricity of 0.9), their predicted 1000-5000 AU detection levels drop from 100% to

[1]We should acknowledge at this point that Gizis et al. (2001a) never specifically refer to a "semi-major axis". Instead they refer to a "separation" in AU (which should, at the very least, be acknowledged as a projected separation because of unknown inclination). But since they directly compare their "separations" with Marcy & Butler (2000) determined "separations," which are true semi-major axes, we find it reasonable to assume that Gizis et al., in practice, equate "separation" with semi-major axis.

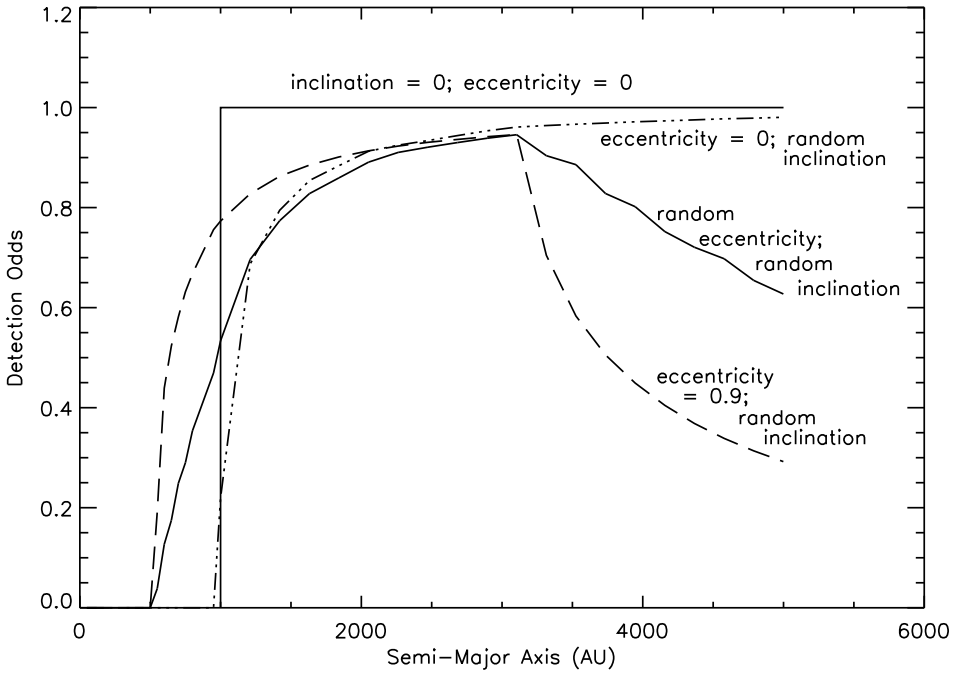

Figure 4.10: Here we plot detection odds for 2MASS wide-separation L-dwarf companions surveyed in Gizis et al. (2001a). The curve labeled "inclination = 0; eccentricity = 0" represents the predicted L-dwarf detection odds described in Gizis et al. (2001a). The dot-dashed curve represents the same predictions when one assumes a random inclination. The solid "random eccentricity; random inclination" curve represents the predicted detection odds when both eccentricity and inclination are assumed random. The dashed curve represents predicted detection odds when inclination is random and eccentricity = 0.9. The curves highlight the importance of including inclination and eccentricity considerations when concluding brown dwarf companion populations.

80%. If inclination is random and eccentricity is 0.9, their predicted 1000-5000 AU detection levels drop from 100% to 69%. This comparison highlights the importance of including inclination and eccenctricity considerations when concluding companion frequencies.

4.4.3 Stellar Companion Searches

I use the title "Stellar Companion Searches" to include companion population studies that examine nuclear-burning companions to main sequence stars. Duquennoy & Mayor (1991) and Fischer & Marcy (1992) fall into this category as they use stellar companion periods (derived from radial velocities and wobble techniques) to determine companion frequency versus semi-major axis. Since their semi-major axis values derive from measured periods, they avoid the pitfalls taken by McCarthy & Zuckerman (2004) and Gizis et al. (2001a). From their analyses, they determine that just over 10% of main sequence stars have 0.08-0.32 $M_{\odot}$ companions between 25 and 100 AU. Based on an equation 4.7 mass function then, we should expect 9.6% of stars to have brown dwarf companions between 25 and 100 AU. This value just falls within the upper limits of our calculated brown dwarf populations. Therefore, while our population statistics suggest a drop-off from the ordinary field mass function, our results do not preclude that the two could still agree.

4.5 Summary

We showed in this chapter how we may combine a likelihood analysis approach with Monte Carlo simulations to derive brown dwarf companion population upper limits from CHAOS observational data. Using this technique, we found, at a 90% confidence level, a brown dwarf companion population upper limit of 9.7% for semi-major axes between 25 and 100 AU. In Figure 4.11 we show our brown dwarf companion results compared with brown dwarf companion population estimates by Marcy & Butler (2000), McCarthy & Zuckerman (2004), and Gizis et al. (2001a). While our results may seem less constraining than the comparable imaging surveys by Mc-

Carthy & Zuckerman and Gizis et al. (2001a), we showed in the previous sections that systematic errors in their analysis, due to unaccounted-for projection effects, cause them to deduce conclusions and uncertainties inconsistent with their observational data. Marcy & Butler brown dwarf population values, which derive from radial velocity measurements, may be used as a trustworthy comparison with our results.

When we combine Duquennoy & Mayor (1991) and Fischer & Marcy (1992) stellar companion frequencies with brown dwarf field mass functions, predicted by Chabrier (2001), we deduce that 9.6% of main sequence stars should have brown dwarf companions. However, our observational results indicate that, in 89% of all Monte Carlo scenarios, we find a brown dwarf companion frequency less than the value extrapolated from a field brown dwarf mass function. Hence, with an 89% certainty, we conclude that the "brown dwarf desert" described by Marcy & Butler (2000) continues, in at least some regard, into the 25-100 AU semi-major axis region.

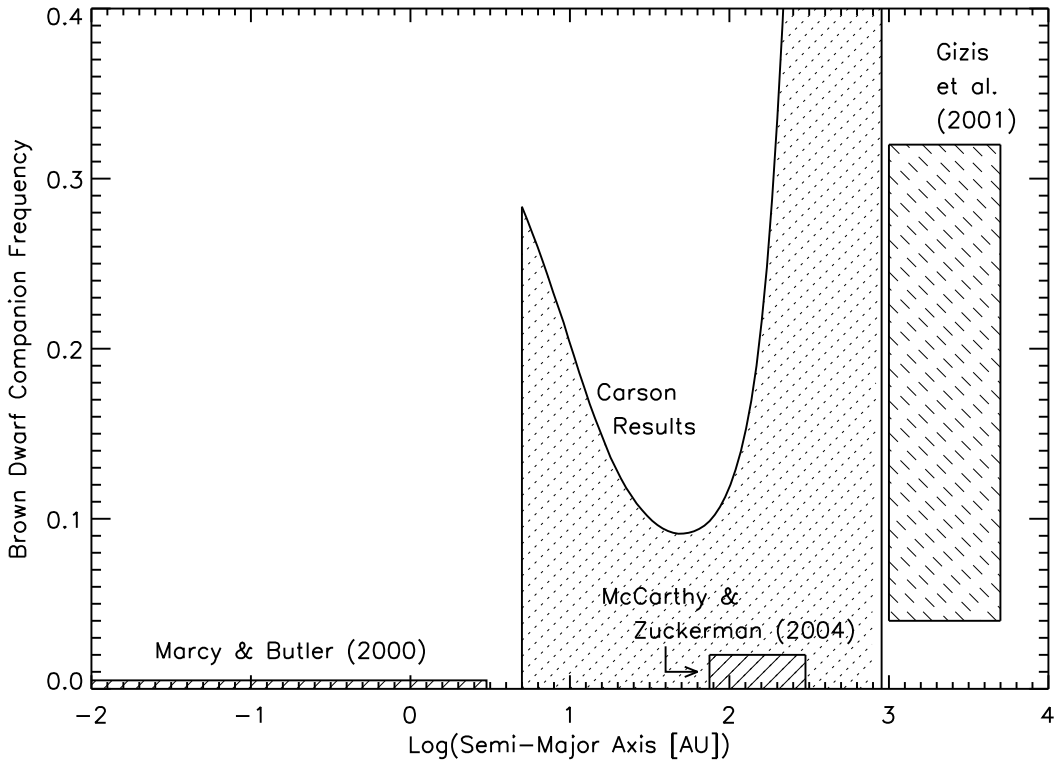

Figure 4.11: Here we plot brown dwarf companion frequencies as predicted by myself, Marcy & Butler (2000), McCarthy & Zuckerman (2004), and Gizis et al. (2001a). The shaded regions represent brown dwarf companion frequencies allowed by the various surveys. While the brown dwarf imaging survey results of McCarthy & Zuckerman and Gizis et al. appear more constrained than the Carson results, we showed in this chapter that systematic errors in their analysis cause them to derive conclusions not supported by their observational data. The Marcy & Butler results, avoiding these pitfalls, may be used as a useful comparison with our population values. Taking this fact and the known field brown dwarf density into consideration, our results conclude that, in 89% of all Monte Carlo scenarios, the suppressed brown dwarf companion mass function (as compared to the field brown dwarf density) continues, in some regard, from the the Marcy & Butler <3 AU region into the 25-100 AU space.

Chapter 5

A Probable White Dwarf Companion to HD150451AB: A Discovery Made in the Course of the CHAOS Survey

5.1 Introduction

White dwarf companion observations are important because they preserve clues to star formation history and galactic evolution as a whole. Comprehensive statistics on the mass distribution of white dwarf companions can provide insights into binary orbital evolution and post-main-sequence mass loss (Oswalt et al. 1990). And while thousands of white dwarfs have been discovered in the last century, the number of white dwarfs companions to normal stars remains a relatively small proportion. Silvestri et al. (2001), for instance, compiles a list of 50 such objects around main sequence stars. Larger mass white dwarfs ($>0.6M_{\odot}$) make up a an even smaller

minority of this subset. White dwarfs with masses greater than $1.0 M_{\odot}$, for instance, make up less than 2% of the general white dwarf population. Thus, the discovery and classification of a greater number of more massive white dwarfs is greatly needed in order to better understand the higher end of the white dwarf luminosity function.

Section 5.2 below describes the observational evidence for HD150451C, first discovered with the Palomar 200-inch telescope during the course of the Cornell High-order Adaptive Optics Survey for Brown Dwarfs (CHAOS). Section 5.3 discusses the properties of the companion and the implications for the stellar system. In Section 5.4 we present our conclusions.

5.2 Observations

5.2.1 Palomar Adaptive Optics Coronagraphic Observations

We first imaged HD150451C in May 2000 as part of the CHAOS survey for brown dwarf companions. We designed CHAOS to use the Palomar Hale Telescope's adaptive optics (AO) system (Troy et al. 2000) to examine 80 bright stars out to 13 parsecs (J. Carson et al., in preparation). The PHARO science camera's (Hayward et al. 2001) coronagraphic and spectroscopic modes combine Strehl ratios typically $\sim 30\%$ (V $\sim$ 10 mag) with a 40-mas pixel scale to allow high dynamic range observations of faint companions to bright stars. Our May observations included 120 5.45-second K_s exposures of HD150451AB with the camera's large Lyot cross and a $0\farcs91$ coronagraphic occulting spot positioned in the center of the $0\farcs8$ binary. A set of 60 5.45-second sky images (5 positions separated by $5''$ dithers) flanked the target set on each side. Table 5.1 displays the system coordinates and relevant target information.

Table 5.1: The HD150451 System

Star	R.A. (J1991.25)[a]	Decl. (J1991.25)[a]	Parallax (mas)[a]	Spectral Type[b]	ρ (arcsec)[c]	θ (deg)[d]
A	16 41 11.53278 $\pm$ 0.00007	-01 00 01.0213 $\pm$ 0.0008	21.22 $\pm$ 1.06	(F0-F1)V	-	-
B	16 41 11.58416 $\pm$ 0.00123	-01 00 00.9771 $\pm$ 0.0185	21.22 $\pm$ 1.06	(K1-K2)V	0.777 $\pm$ 0.009	74.8 $\pm$ 0.1
C	-	-	-	-	6.750 $\pm$ 0.015	71.0 $\pm$ 0.1

[a]From Hipparcos (Perryman et al. 1997)

[b]Based on Hipparcos magnitudes and Kroupa et al. (1993) color-color diagrams.

[c]Separation from star A, as observed with Palomar Adaptive Optics, September, 2002.

[d]Position angle, measured counter-clockwise from Star A's north-south axis. Observed with Palomar Adaptive Optics, September, 2002.

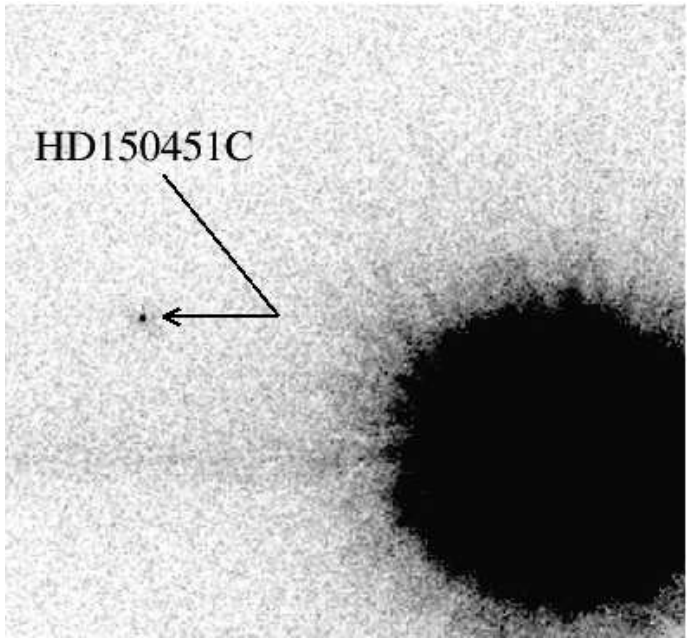

Figure 5.1: A probable white dwarf companion to the binary system HD150451AB imaged with Palomar AO in May, 2000. At a separation of 6″, the candidate companion exhibited a K-magnitude of 16.0 ± 0.2 with J - K = 0.55 ± 0.10.

For our May observations, we began data reduction by median-combining each 60-image sequence of dithered sky images to create a sky frame. Using standard procedures, we created a flatfield array from twilight images taken earlier that evening. A sky frame was subtracted from each target image and the flatfield was applied. We median-combined the 120 target images after using the point spread function (PSF) from the parent star to shift any frames that may have mis-alignments due to telescope drift. Finally, we applied a bad-pixel algorithm that sorted through the frames and replaced, using the median of its neighbors, any pixel value that differed from surrounding pixels by more than 5-sigma. We present the resulting image in Figure 5.1.

At 47 parsecs from our solar system, the primary system HD150451AB was originally selected as a possible PSF calibration star for CHAOS. Noticing a potential companion 6″ from the primary system, we followed our May observations with J

and K photometry in August, 2000. While HD150451C could only be seen with the adaptive optics system engaged (hereafter referred to as closed-loop), our standard star, FS144, required non-AO "natural seeing" imaging (hereafter referred to as open-loop) in order to avoid saturation in the minimum exposure time. In order to compare the open-loop standard star fluxes with the closed-loop HD150451C fluxes, we additionally took closed and open loop images of a third star, Gliese 631. Our general plan was thus the following: (1) Take open-loop J and K photometry of the standard star FS144. (2) Take open-loop and closed-loop J and K photometry of the calibration star GL631; This star was selected based on the similarity of its closed-loop PSF to that of HD150451A. (3) Take closed-loop J and K photometry of HD150451C. (4) Use the calibration star closed to open-loop ratio to compare HD150451C fluxes with that of the standard star FS144. Below I explain this procedure in greater detail.

The close proximity (107″ separation) and similar magnitude ($\Delta V < 0.5$ mag) between Gliese 631 and HD150451A ensured that the Palomar Adaptive Optics (which guides on visible light) would produce similar closed-loop PSFs for Gliese 631 and the brown dwarf candidate. To transform magnitudes from open to closed-loop, we took 15 images each of Gliese 631 in closed-loop J (5.45-second exposures), open-loop J (5.45-second exposures), closed-loop K (5.45-second exposures), and open-loop K (1.8-second exposures). We measured a magnitude difference of 0.82 (K-band) and 1.38 (J-band) between closed-loop (0.″12 aperture radius for J and 0.″24 aperture radius for K) and open-loop (4-sigma aperture radius) fluxes. We used a larger aperture for closed-loop K than closed-loop J due to the naturally wider point spread function for longer wavelength images. A 0.1% neutral density filter was used with all these sets in order to avoid saturation. Before the Gliese 631 images,

we took 150 1.8-second closed-loop K-band images of HD150451ABC flanked by an equal number of dithered sky images. Like the May observing set, we positioned a 0.″91 coronagraphic spot in the center of the AB binary. We repeated the K-band data set with an identical closed-loop set in J-band. Before the HD150451ABC images, we took 15 open-loop images each in J (29.0-second exposures) and K (10.9-second exposures) of the standard star FS144. Performing photometry on all three targets, we were able to calibrate the HD150451C closed-loop magnitudes.

For these August observations, we subtracted a median-combined sky image and applied a flatfield using a procedure similar to the one used in May. We then divided the 150 images into 5 30-image subsets and median-combined each subset. The subsets allowed us to gauge uncertainty by observing the spread in flux values. After applying our bad-pixel filter, we conducted photometry on each of the 5 images by measuring the flux in a 3 pixel (for J-band) or 6 pixel (for K-band) aperture radius. While our parent system was largely occulted by our coronagraphic mask, residual star flux from the central binary still contaminated the brown dwarf candidate's flux. For example, in a typical J or K-band image, we found that about 20% of the photons in our flux aperture were due to the parent system rather than the brown dwarf candidate. We quantified, and therefore were able to remove, this residual flux by mapping the slope of the parent system's brightness as a function of distance from the central binary. The corrected HD150451C flux values were then averaged together and the uncertainty was determined from the standard deviation from the mean.

For the photometric standard star, FS144, we median-combined the dithered images to create a sky frame in each filter. After subtracting the sky frame and applying a flatfield, we median-combined each of the 5 30-image subsets and ran

our bad-pixel filter. We determined a flux value for each of the 5 images by using a 4-sigma radius aperture and circular sky annulus. We averaged together our final flux values and determined an uncertainty from the standard deviation from the mean. We determined the flux for the Gliese 631 sets in a similar manner, using a 3 pixel or 6 pixel aperture radius for closed-loop images and a 4-sigma aperture radius for open-loop images.

We used the Gliese 631 flux ratios between open and closed loop to compare our calibration star with HD150451C flux levels. We measured J-K=0.55±0.10 mag and m_k=16.0 ± 0.2 mag (MKO-NIR filter set). If we assume HD150451C is a physical companion, this corresponds to an absolute magnitude M_K=12.6 ± 0.2 magnitudes. These values are consistent with a white dwarf or an early-type methane brown dwarf (see Figure 5.2).

In September, 2002, two years after taking the first observations, we conducted astrometric measurements of the three-object system. We took 20 sets of 10 1.817-second exposures in K_s where each set was separated by a 5″ dither. In these data sets, we let our coronagraphic spot avoid the parent system since our astrometric measurements were less sensitive to pixel saturation than the photometry measurements.

To conduct astrometry for HD150451B and C, we ran an algorithm to sort through each of the 150 August-2000 images and 200 September-2002 images and examine the areas that included the candidate companion and parent system approximate positions. We omitted conducting astrometry for HD150451A since it was heavily occulted by our coronagraphic mask in the August-2000 data set. (For unocculted data, the peaks of A and B were easily resolvable.) For HD150451B and C astrometry, single images did not provide sufficient signal-to-noise ratios to allow

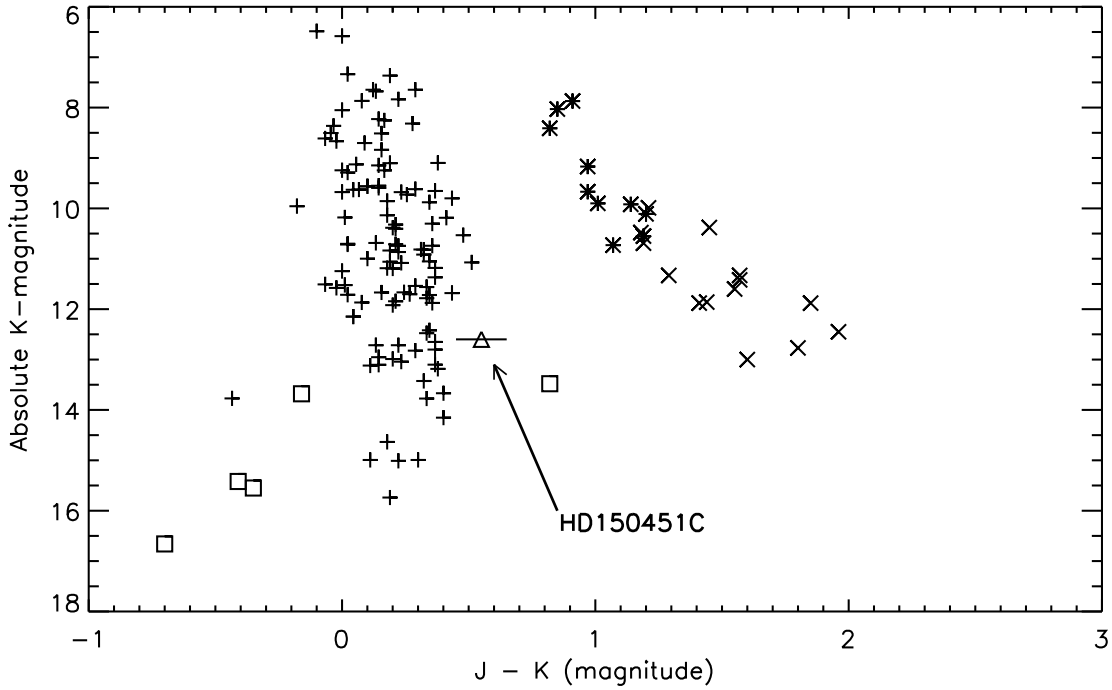

Figure 5.2: Absolute K-magnitude vs. J-K for observed M, L, T brown dwarfs and white dwarfs. The data points correspond to the following classifications: (∗) = M dwarfs; (×) = L dwarfs; (□) = T dwarfs; (+) = white dwarfs. M and L dwarf colors and absolute magnitudes are from Leggett et al. (2002). The T dwarf colors and absolute magnitudes are either from Leggett et al. (2002) or, in the case of some of the absolute magnitudes, were derived by the authors using Leggett et al. (2002) apparent magnitudes and Dahn et al. (2002) parallax measurements. White dwarf colors and absolute magnitudes are from Bergeron et al. (2001). All photometric values, including those of HD150451C, represent MKO-NIR photometry. White dwarf values were published in the CIT system, but were transformed, by the authors, into the MKO-NIR system using equations given by Hawarden et al. (2001).

a Gaussian fit. Instead, we used an algorithm which chose the peak pixel value to be the central position of the object. We averaged the position values of each data set (150 August-2000 positions and 200 September-2002 positions) and determined the uncertainty from the standard deviation from the mean. For the August-2000 HD150451B position determinations, we found that partial occulting by the coronagraphic mask made it unreliable to use the peak pixel value as our star position. Instead, we inspected each image individually and used the intersection of the star's diffraction spikes as the central position. We found this to be an accurate method since the diffraction spikes of A and B were easily distinguishable and HD150451B's spikes provided a well-defined cross-hair. Our uncertainty was determined from the standard deviation from the mean. Using the aforementioned techniques, we were able to determine an object's position with an accuracy ranging from 2 to 24 mas (one pixel = 40 mas) depending on the signal to noise ratio. Between August, 2000 and September, 2002, we found that HD150451C exhibited a shift (measured relative to HD150451B) of $\Delta\alpha$=12 $\pm$ 17 mas and $\Delta\delta$=$-$4 $\pm$ 23 mas, a measurement consistent with no relative shift. Hipparcos proper motion measurements (Hipparcos catalogue; Perryman et al. 1997) for HD150451AB predict a system shift of $\Delta\alpha$=41.2 $\pm$ 2.4 mas and $\Delta\delta$=$-$23.3 $\pm$ 1.9 mas for the same period. Therefore, given the precision of our measurements, the odds of a non-associated background star displaying a measured movement equivalent to the Hipparcos values are about 1 in 110. Thus, at a 99% confidence level, we conclude that HD150451C is a physical companion and not a background star.

In June, 2004 K. Matthews repeated the September, 2002 astrometric observations to confirm a physical companionship. While data reduction for these observations is still underway, preliminary results agree with HD150451C being a physical

companionship.

We may consider whether our observed common proper motion is instead due to a change in pixel scale between measurements. For the two observing nights in question, we did not conduct any independent test of pixel scale. However, pixel scale calibration measurements taken over a nine month baseline between 2000 and 2001 indicated that the pixel scale was stable to at least 1 part in 100. During this period the AO system and camera were installed and removed about half a dozen times. Thus, to the limits of our measurement abilities, we found no evidence of pixel scale evolution.

Additionally, we note that if we were witnessing a change in pixel scale, then that fractional change should equally affect both the x and y dimensions on our chip. But our measurement of HD150451C's proper motion requires that the pixel scale in x alter by a fraction that is roughly double the pixel scale in the y direction. Therefore, the possibility that pixel scale evolution is causing our perceived common proper motion seems unlikely.

5.2.2 Palomar Wide-field Infrared Camera Observations

In March, 2002 we followed these AO observations with differential methane-band imaging using WIRC, the Wide-field InfraRed Camera on the Palomar 200-inch telescope (Wilson et al. 2003). Methane-band imaging identifies atmospheric methane-band absorption by taking narrow band photometry on and just off the H-band methane absorption window (Rosenthal et al. 1996). Figure 5.3 shows our methane filter transmission curves plotted over a late T-dwarf spectrum. The plot demonstrates how, for a methane brown dwarf, differential photometry should show an easily measurable drop in flux from short to long bands. The use of a wide field

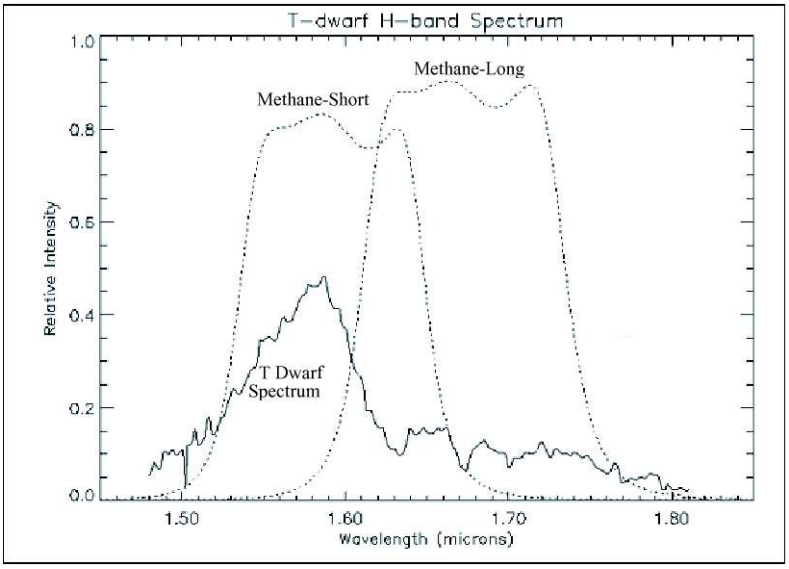

Figure 5.3: WIRC methane filter transmission curves plotted over a sample methane brown dwarf spectrum (Leggett et al. 2000). Our methane filters were fabricated by NDC Infrared Engineering and purchased through the MKO consortium (Simons and Tokunaga 2002; Tokunaga et al. 2002).

(5'×5') camera allows us to compare a brown dwarf candidate's flux with field stars to remove any systematic effects from the analysis (e.g. non-photometric sky conditions). We obtained a total of 160 14.54-second exposures (9 positions separated by 20″ dithers) in the CH_4-Short (1.53-1.65μm) and CH_4-Long (1.61-1.73μm) filter bands. (Our methane filters were fabricated by NDC Infrared Engineering and purchased through the MKO consortium [Simons and Tokunaga 2002; Tokunaga et al. 2002].)

We began our photometry by median-combining the dithered images of each set to create sky frames. We created flatfield arrays using dome-flat images taken later that night. We subtracted the sky and applied the flatfield to each target image. To perform accurate photometry on the brown dwarf candidate, it was important to ensure that the measured differential flux was not contaminated by residual flux from the parent system (see Figure 5.4). To do this, we took data from three sets

extending over two separate nights and, in each data set, used two independent star flux subtraction methods. This gave us a consistency check for any apparent methane detections. For the first star flux subtraction method, we measured the background flux by creating a circular annulus centered on the candidate companion. For the second method, the background flux was estimated by creating an arc extending along a constant radius from the parent system. With the parent system's diffraction spikes defining four quadrants, we extended our arc along the quadrant containing our candidate companion. We truncated the arc in the areas where it began to overlap with the parent system's diffraction spikes. (For the WIRC observations, the parent binary was unresolved and therefore had only one set of diffraction spikes.) The partial annulus allowed us to estimate the residual flux at the brown dwarf's separation from the parent system. Using a 2.9-sigma radius aperture, we compared the resulting background-subtracted brown dwarf candidate flux with the measured flux of various field stars. Figures 5.5a, 5.5b, and 5.5c show the resulting flux ratios from these procedures [(a) Data set 1, 22nd March 2002; (b) Data set 2, 26th March 2002; (c) Data set 3, 26th March 2002]. The field star data points give us an idea of our uncertainty. (For field stars, we conducted sky subtraction using a circular, star-centered annulus with a 2.9-sigma radius aperture.) Our uncertainties extend over a considerable range though all data sets, with the possible exception of the middle set where uncertainty is very high, suggest a drop in flux from short to long, the signature of a methane-abundant atmosphere. Incidentally, we also note that the apparent methane depression change ($\sim 12\%$) between the first and second night is consistent with other groups' variability monitoring of T dwarfs (E. Artigau, in preparation).

As another test of the candidate's methane abundant properties, we mapped

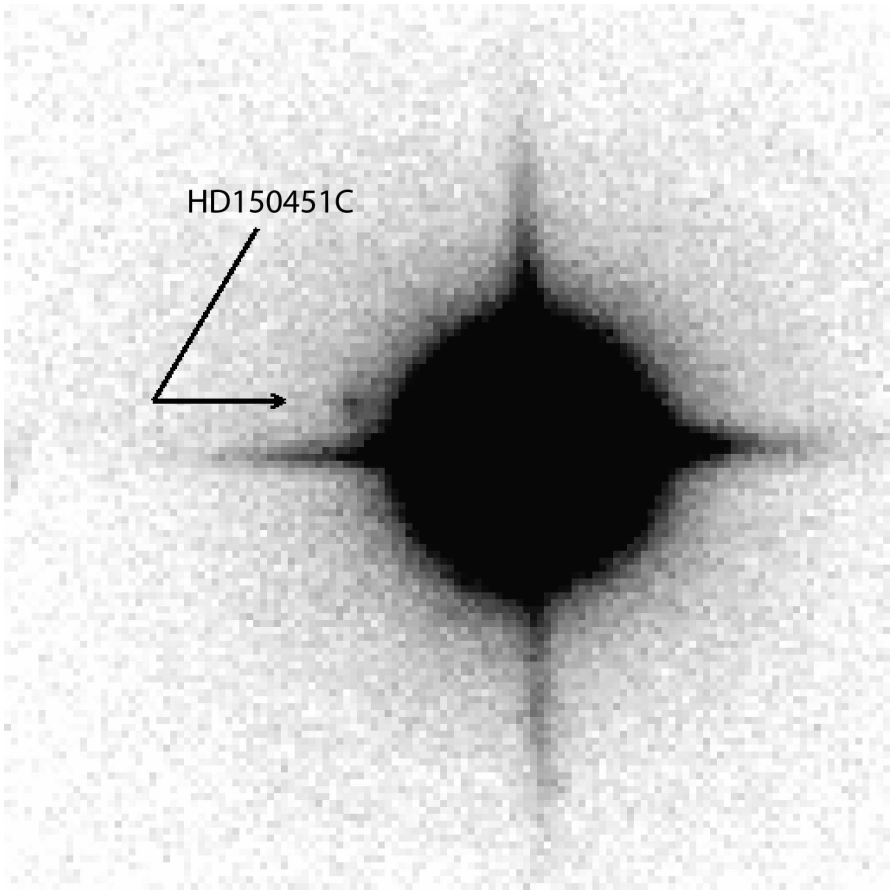

Figure 5.4: A close-up of a Palomar Wide-Field Infrared Camera image of HD150451C and an unresolved HD150451AB taken in the methane-long filter band. The image provides an example of the HD150451AB pollution that affects HD150451C photometry.

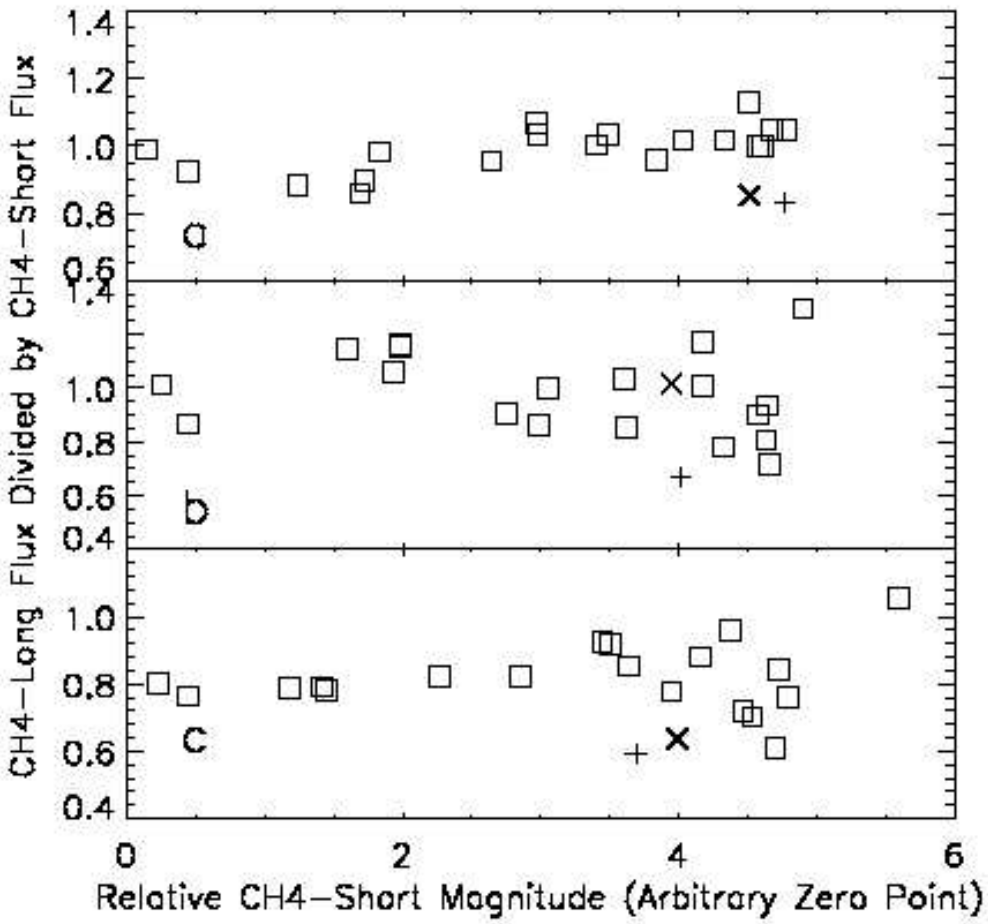

Figure 5.5: HD150451C Methane Depression Measurements [(a) Data set 1, 22nd March 2002; (b) Data set 2, 26th March 2002; (c) Data set 3, 26th March 2002]. (□) = Field stars; (+) = HD150451C reduced with an HD150451C-centered sky annulus; (×) = HD150451C reduced with an HD150451AB-centered sky annulus. While the scatter in the measurements for HD150451C on a given night is large (due to contamination from the parent binary), our data suggest depressed methane band emission as compared to field stars.

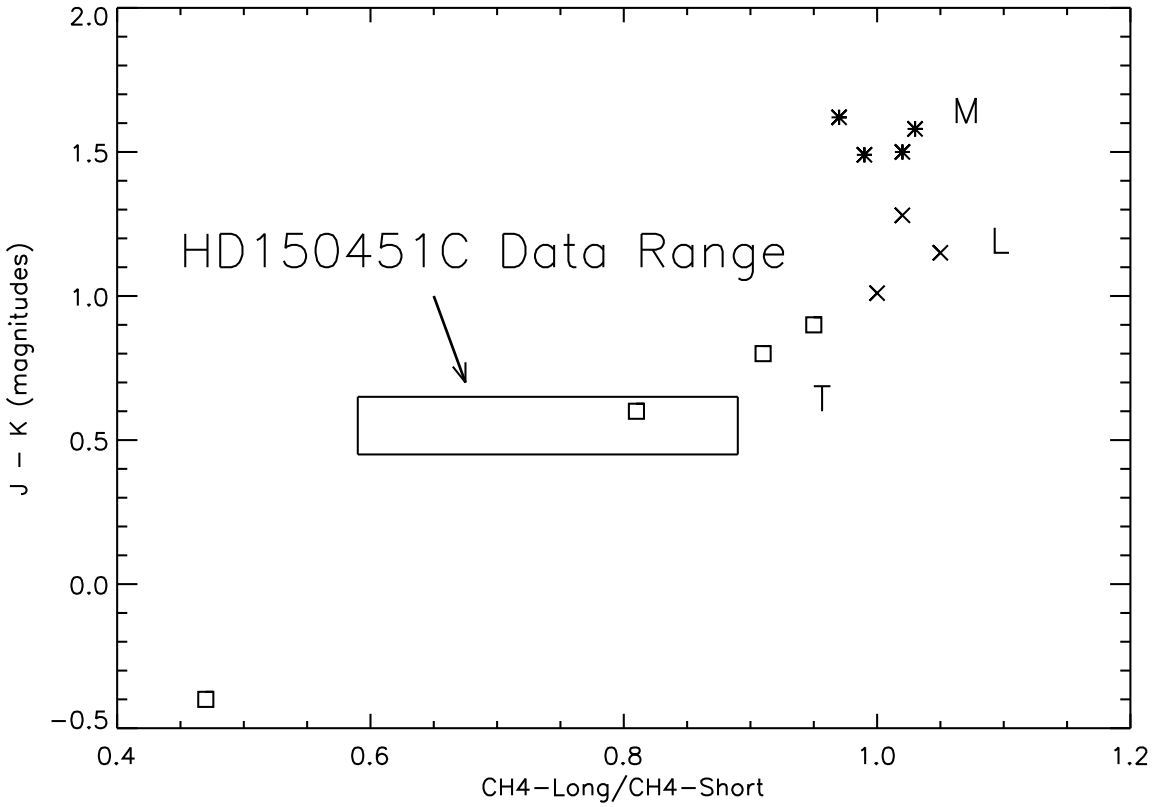

Figure 5.6: J-K vs. CH_4-Long/CH_4-Short for published spectra convolved with CH_4-Long and CH_4-Short filter transmission curves for the Palomar 200-inch Telescope's Wide-field Infrared Camera (WIRC). The data points correspond to the following classifications: ($*$) = M dwarfs (Legget et al. 2001); ($\times$) = L dwarfs (Leggett et al. 2001); ($\square$) = T dwarfs (Leggett et al. 2000).

out the object's suggested methane depression levels versus its adaptive optics J-K values. We then took published brown dwarf spectra and J-K magnitudes (Leggett et al. 2001; Leggett et al. 2000) and convolved the spectra with our measured filter response curves. All the published data noted here used the same MKO-NIR filter system as PHARO. The comparison showed that all of our values were consistent with those of a methane dwarf (see Figure 5.6).

5.2.3 Palomar IR Camera Observations

In May, 2003, we followed our WIRC observations with spectral observations using the Palomar D78 IR Camera. The system allowed us to combine the Palomar 200-inch telescope's light-collecting power with a low resolution (R $\sim$ 100) grism-spectrograph to maximize our companion's signal-to-noise. The parent system's close proximity (6″ away) and resulting interfering brightness (differential magnitude, compared to HD150451C, $\sim$ 11 magnitudes) made maximizing our signal-to-noise ratio an important consideration. We aligned the slit along the north-south axis to minimize the light from the parent system, positioned almost directly west. With the instrument's H-grism and 1.0-arcsecond slit, we took nine 300-second images separated by 5″ dithers along the slit axis. Figure 5.7 shows a sample spectral image. Even positioned 6 arcseconds west of the slit, the parent system's light still appears as the brightest spectrum in our image.

Before taking the HD150451 exposures, we took a 60-second spectral image (H-grism, 1.0-arcsecond slit) of the G-star SAO 85575. During the exposure, we activated the 200-inch telescope's chopping secondary so that the calibration star's flux extended across the entire length of the slit. After this exposure, we moved the telescope 20" and took a 60-arcsecond sky image. After the HD150451 exposures, we repeated this G-star observing procedure for the G-star SAO 121152. The close time proximity and similar airmasses (1.30 for SAO 85575, 1.52 for SAO 121152, and 1.38-1.62 for HD150451C) between the SAO stars and the target made the G-stars a useful tool to calibrate instrument and sky conditions.

We began our spectral analysis by subtracting the accompanying sky spectral images from the G-star spectral images. Next we ran a bad pixel algorithm which flagged any pixel that differed by more than 5-sigma from the three pixels above

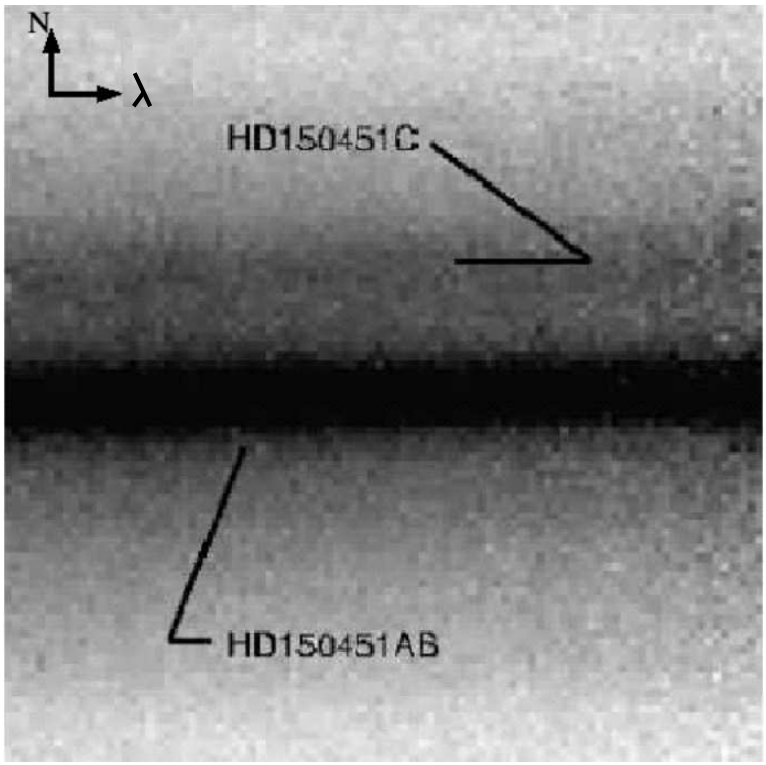

Figure 5.7: H-band spectrum of HD150451AB and HD150451C. We note here the interfering HD150451AB spectral flux that affects our HD150451C spectroscopy: Positioned 6″ west our 1.0 arcsecond slit, the parent binary still appears as the dominant spectrum.

and three pixels below. We replaced the flagged pixels with the median of its pixel neighbors above and below. Finally, we normalized our resultant array to a value of one.

For reducing our HD150451 set, we began by subtracting each of the nine images from the image immediately preceding it. We made an exception for the first image, subtracting it from the ninth image. Given the spacing of our dithering pattern, these subtractions allowed us to remove interfering sky flux without losing the target spectral flux. The resulting images each contained a positive and negative spectrum of the composite HD150451AB and the resolved C. Next we divided our images by one of our G-star spectra, whose median value we normalized to one. We chose which of our G-star spectra to use based on the closeness of it airmass value. This division performed multiple functions: It served as a flatfield to correct for varying pixel sensitivity; It also corrected for telluric absorption; Thirdly, since the G-star spectrum closely resembles a blackbody spectrum, the resulting HD150451 spectra should reflect primarily the two spectra's absorption and emission features, if existent. After performing the division, we applied the bad pixel filter described in the previous paragraph. We acknowledge that, in this procedure, we have effectively assumed that our G-star spectrum represents a perfect blackbody function, where any deviations are due to pixel sensitivity variations or telluric absorption. This, of course, is not an entirely correct assumption, for G-star spectra do possess narrow (< 0.01 micron width) absorption and emission features (Lancon & Rocca-Volmerange 1992). However, for the purpose of our analysis, where we are searching for broad features a few tenths of a micron in width, such as the water and methane absorption bands shown in figures 5.3, 5.8a, and 5.8b, the assumption of a perfect blackbody is an effective approximation.

After this processing, we examined our G-star spectral images and mapped how the x-axis position of spectral features varied as we scanned up and down the image. If there were no curvature issues, the spectra's positions should should remain constant as one moves up and down the image. In our case, we had some curvature which we removed by recording the observed deviation from the ideal case and then shifting each HD150451ABC row accordingly.

As displayed in Figure 5.7, the parent system's spectral light overlaps with the C component's flux. At the center of the HD150451C spectrum, we found that AB contributed about 21,000 counts while the C component contributed about 5,000 counts. (Background noise measured a minor 6 counts per pixel.) We removed the interfering parent flux by first measuring the HD150451AB spectrum's central y-axis position. We then took each pixel in the HD150451C spectrum and subtracted from it the pixel that was the same distance from the parent spectrum center, but located on HD150451AB's opposite side. Thus, in a sense we are cutting HD150451AB down the middle, folding it over and subtracting it. We next extracted each of our positive and negative parent-subtracted spectra, including all flux 1.5-sigma above and below the spectrum center. We then subtracted each negative spectrum from the positive spectra. This effectively summed the two spectra while removing any residual sky flux. For the first image, we refrained from conducting this subtraction since we had an uneven number of total exposures. We summed the y-direction of each spectrum to create one dimensional spectra. We next summed our five one-dimensional spectra to create the HD150451C spectrum shown as Figure 5.8d.

For comparison, we also reduced an HD150451AB spectrum. For this reduction, we used the same procedure used with HD150451C, but without any subtraction of interfering flux. Figure 5.8c displays the resultant HD150451AB spectrum. This

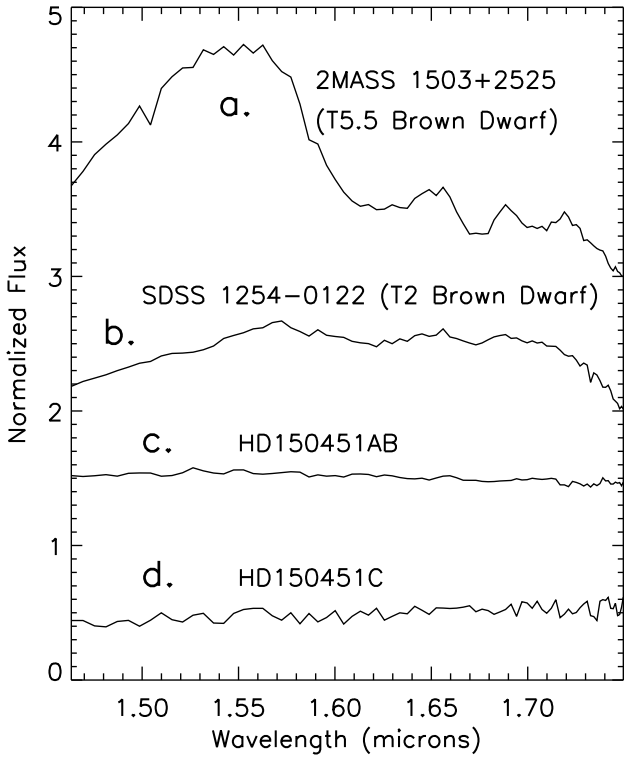

Figure 5.8: H-band spectra of 2MASS 1503+2525 (7a), SDSS 1254-0122 (7b), HD150451AB (7c), and HD150451C (7d). The spectra's y-axis values represent the spectra's flux values, normalized to a value of one, and then offset on the plot for exhibiting purposes. In addition to the observed lack of methane absorption, we also note, in HD150451C, the absence of the strong water bands evident in the brown dwarfs displayed in the top two plots. Instead HD150451C most closely resembles the blackbody-like spectrum HD150451AB, supporting HD150451C's white dwarf classification.

spectrum was useful for comparison because any emission or absorption features in the HD150451C spectrum could be compared with HD150451AB's spectrum to ensure that features were indeed unique.

For additional comparison, we also conducted observations of the T2 brown dwarf SDSS 1254-0122 (Leggett et al. 2000) and the T5.5 brown dwarf 2MASS 1503+2525 (Burgasser et al. 2003c). For each observing set, we took five 300-second exposures (H-grism, 1.0-arcsecond slit) separated by 5" dithers along the slit axis. We accompanied the SDSS 1254-0122 exposures (airmass 1.27-1.32) with a 40-second image (H-grism, 1.0-arcsecond slit, airmass 1.34) of the G-star SAO 80478. Again we activated the 200-inch telescope's chopping secondary to extend our flux along the entire extent of the slit. After, we dithered 20" off the source to take an accompanying 40-second (H-grims, 1.0-arcsecond slit) sky exposure. This G-star exposure set also served as the calibration star for 2MASS 1503+2525 (airmass 1.18-1.25), which we observed immediately after. We reduced the T-dwarf data sets using the same procedures we used for HD150451AB. Figures 5.8a and 5.8b display the resulting spectra.

We determined our wavelength solution for the four spectra by comparing the 2MASS 1503+2525 spectrum with the published spectral data from Burgasser et al. (2003c). With five identifying features, our wavelength solution matched the published data to within 0.002 microns. Comparing the four spectra, one sees that HD150451C most closely resembles the flat spectrum of HD150451AB: The HD150451C spectrum lacks signs of the methane absorption bands we expect in a methane brown dwarf; But more noticeably, the C spectrum lacks the strong water absorption bands present in 6a and 6b. Given the C component's luminosity and infrared colors, such a blackbody-like spectrum is most consistent with a cool ($\sim$

6700K) white dwarf (see later discussion in section 5.3.3).

5.3 Discussion

5.3.1 Association with HD150451AB

As shown in section 5.1, astrometric measurements between August, 2000 and September, 2002 give evidence of common proper motion, the indicator of a physical association. We acknowledge however that our 99% confidence level, by itself, leaves a non-zero possibility that we are instead observing simply a statistical fluctuation coinciding with common proper motion. To improve the certainty of our conclusions, we calculate the odds of coming across such a statistical phenomenon through the course of our survey.

From the known field density, as determined from our 4.1'×4.1' WIRC field of view of the HD150451ABC region, we find that the probability of finding a field star (with brightness $\gtrsim$ HD150451C's brightness) within 6″ of the parent system is roughly 3%, a small, but nonzero value.

Next we consider the density of stars with J-K colors similar enough to potentially be confused with our object. If we simulate an exponential mass function, as given by Chabrier (2001), we find that, given our sensitivities, 5.6% of all observable main sequence stars should have J-K values consistent with our measured colors (Drilling & Landolt 2000; Gilmore & Zeilik 2000; Tokunaga 2000). This fraction corresponds to the G6-K4 V spectral types. Additionally, we know that such an object can be no more than $\approx$ 320 pc away in order for the corresponding luminosity to be consistent with the apparent magnitude (Drilling & Landolt 2000; Tokunaga 2000). Given the volume density of G6-K4 V stars as described by Kirk-

patrick (2001), the odds of happening upon one of these objects 6″ from our parent system is 1.7×10^{-4}. This value is effectively unchanged when we include giants and supergiants as well, since their space density (Mikami & Ishida 1981) is small enough to be negligible for our considerations.

Finally, we combine this space density value with the probability of a 2.6-sigma deviation taken over the course of our survey. Presently, we have observed on the order of 100 systems. Thus, through measurements of 100 systems, the odds of finding a non-associated main sequence star, with 2.6-sigma proper motion measurements, with colors and magnitude consistent with HD150451C, within 6″ of our parent system is $\sim 1.6 \times 10^{-4}$.

We may also consider the odds of discovering a non-associated white dwarf 6″ from our system. Figure 5.2 data indicates that a white dwarf with our J-K values would require a minimum absolute K-magnitude somewhere around 10 mags. Thus, a non-associated white dwarf with our apparent magnitude of 16 mags could have a maximum distance around 160 parsecs. Given the white dwarf space density predicted in Leggett, Ruiz, & Bergeron (1998), the odds of finding such an object within 6″ of our system is roughly 1.3×10^{-5}. Thus, through measurements of 100 systems, the odds of finding a non-associated white dwarf star with our J-K values and 2.6-sigma common proper motion measurements are $\sim 1.2 \times 10^{-5}$. Thus, all scenarios compel us to interpret HD150451C as a true physical companion.

Our final consideration is whether our HD150451C perceived common proper motion is instead due to an orbital motion between HD150451A and B. In other words, if our candidate companion and binary system were in fact unrelated, could HD150451B orbital motion lead us to believe that the separation between HD150451C and AB was staying constant over the two year time span, while the binary center

of mass was in fact changing its separation with HD150451C? Recall that in section 5.1 we used HD150451B as a stationary indicator of our central binary position. Therefore, our conclusions require that, over the two year time span, HD150451B remains effectively non-moving relative to the parent binary center of mass. Is this a reasonable assertion? As mentioned in section 5.1, HD150451A is heavily occulted in the August-2000 data set, preventing a rigorous determination of its position. However, we do have limited calibration data, taken immediately following that set, that shows the relative positions between HD150451A and B. Using this data, along with the more extensive September-2002 data sets, we measure that, between August, 2000 and September, 2002, HD150451B exhibited a shift, relative to HD150451A, of $\Delta\alpha$=-12 ± 12 mas and $\Delta\delta$=$+16 \pm 24$ mas. Thus, the values yield no compelling evidence for a nonzero shift between HD150451B and HD150451A. Incidentally though, if we accept $\Delta\alpha$=-12 mas and $\Delta\delta$=+16 mas as true physical shifts, then we find that our HD150451C measured shift (relative to the primary system center of mass) changes from $\Delta\alpha$=12 ± 17 mas and $\Delta\delta$=-4 ± 23 mas to $\Delta\alpha$=0 ± 17 mas and $\Delta\delta$=$+12 \pm 24$ mas. Thus, even including any suggested orbital motion, our measurements are still most consistent with common proper motion, indicating a physical companionship.

5.3.2 Previous Observations of the Primary System HD150451AB

The primary system HD150451AB was originally spectroscopically identified (SAO Catalogue: Ochsenbein 1980) as a single A7III giant. Subsequent observations with Hipparcos instead revealed a binary system with absolute V-magnitudes of 6.3 ± 0.4 mag and 3.0 ± 0.3 mag and a composite B-V value of 0.31 ± 0.02 mag. In contrast, an

A7III giant would have an absolute V-magnitude of 1.1 mag with a B-V value ~ 0.22 mag (Schmidt-Kaler 1982). The Hipparcos values, rather, describe a binary system with an (F0-F1)V and a (K1-K2)V star (Kroupa et al. 1993). Using theoretical age limits given by Schaller et al. (1992) for an F0-F1 main sequence star, we arrive at a system upper age limit of 3.1-3.8 Gyrs.

5.3.3 Estimates of HD150451C Physical Properties

Presently, we cannot reconcile a flat white-dwarf-like spectrum with the suggested methane depression. In the absence of any consistent physical explanation, we classify our object as a white dwarf. While our methane band observational data does suggest methane absorption, it includes a larger amount of uncertainty than our our spectral data.

A White Dwarf Interpretation

To determine a white dwarf temperature from our J - K values, we used observational data from Bergeron, Leggett, & Ruiz (2001) and fitted the following relationship between temperature and J - K values:

$$T = 9756 - 17750 * (J-K) - 12860 * (J-K)^2 + 108300 * (J-K)^3 - 81180 * (J-K)^4 \quad (5.1)$$

where T is the temperature in Kelvin and J-K represents the infrared color measured in the MKO-NIR filter system. (We transformed the Bergeron et al. [2001] CIT color values to MKO-NIR color values using transformation equations by Hawarden et al. [2001].) The spread in the data points yields an uncertainty in the derived temperature of 970 K (see Figure 5.9 to view our fit). Inputting our HD150451C J-K value and uncertainty into this equation, we derive a temperature of 6700 $\pm$970

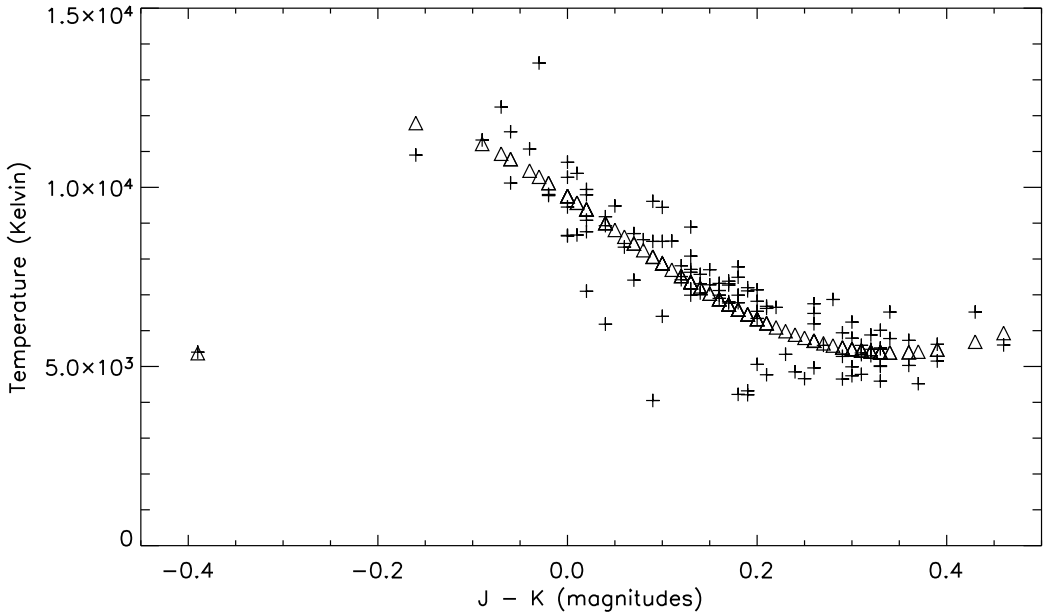

Figure 5.9: Temperature vs. J-K for white dwarf observational data (represented by [+]) from Bergeron et al. (2001). All J-K values represent the MKO-NIR filter system. The original published J-K values, measured with the CIT filter system, were transformed by the authors to MKO-NIR values using transformation equations by Hawarden (2001). The (△) symbols represent the authors' fitted curve to the observational data. See Equation 1 and the accompanying discussion for further information.

Kelvin.

We first shied away from a white dwarf classification because of the object's high J-K value. However, as seen in Figure 5.2, our error bars just include the very reddest end of the white dwarf J-K regime. And strengthening a white dwarf classification, our absolute K-magnitude agrees well with measured white dwarf K-magnitudes.

A white dwarf classification places constraints on our system age. Earlier we mentioned that the central binary's spectral types gives us an upper age limit of 3.1-3.8 Gyrs. For a white dwarf classification, we also require that the system be old enough for HD150451C to have evolved off the main sequence. Determining an exact age is difficult since we must rely on theoretical models, an area of some controversy (see discussion in Bergeron et al. 2001). Nevertheless, to arrive at an age estimate,

we referred to evolutionary models presented in Bergeron et al. (2001) which uses theoretical and observational data to describe physically allowable combinations of mass, temperature and age; Masses and temperature values are mapped out for lifetimes given at 1 Gyr intervals (i.e. 2 Gyr, 3 Gyr, 4 Gyr, etcetera). (These ages include the main sequence lifetimes.) Inspecting these plots, we find that our temperature regime just includes lifetimes of 2 Gyr and up. Thus, from our temperature estimates alone, we derive an age $\gtrsim 2$ Gyrs. Combining this fact with our previous age analysis of the central binary, we derive a system lower limit ≈ 2 Gyrs with an upper limit of 3.1-3.8 Gyrs. If we therefore assume an age range of 2.0-3.8 Gyrs with a temperature of 5730-7670 Kelvin, we derive a mass of 0.6-1.3 $M_{\odot}$, using the aforementioned Bergeron et al. (2001) plots.

Our age estimate also sheds light on the white dwarf progenitor mass. For an age range of 2.0-3.8 Gyrs, Schaller et al. (1992) models predict a minimum mass of 1.250 $M_{\odot}$ for solar metallicity and nonzero convective overshoot. (Due to limits on the model resolution, 1.250 $M_{\odot}$ is outputted for both 2.0 and 3.8 Gyrs.) For an estimate on the upper limit to the the progenitor mass, we refer to Jeffries (1997) who argues a white dwarf progenitor mass upper limit of 5.5 $M_{\odot}$. Thus we determine a final HD150451C progenitor mass of 1.250-5.5 $M_{\odot}$. Using De Jager & Nieuwenhuijzen (1987) spectral type classification curves, we find a corresponding spectral type of B7-F8 V star.

An Alternative Methane Brown Dwarf Interpretation

If we are mistaken to trust a white dwarf classification, and we are indeed observing a methane brown dwarf, then our suggested methane depression levels describe an object ranging from a T0 (weakest methane depression data point) to T6 (strongest

methane depression data point) V dwarf, based on T dwarf classification standards of Burgasser et al. (2002b). We arrived at this classification by comparing our methane ratios with those derived from published T dwarf spectra (Burgasser et al. 2002b) folded through our filter transmission curves. Given this classification, determining a corresponding temperature and luminosity proves difficult since, at the time of this writing, only a handful of T dwarfs have known distances, and hence reliable absolute brightness measurements. However, if we use the spectral types and effective temperatures for the six T dwarfs described in Leggett et al. (2002) and apply a linear function to the data, we derive the following equation:

$$T = 1310 - 58.68 * SpT \tag{5.2}$$

where T is the temperature in Kelvin and SpT is the T dwarf spectral type number (i.e. T3 would be 3, T4.5 would be 4.5, etcetera). The spread in the data points yields an uncertainty in the derived temperature of 59.60 K (see Figure 5.10 to view our fit). Applying our measured spectral type range to this equation, we arrive at a T dwarf temperature range of 960-1310 K. If we assume a radius of 1.0 R_{Jup} (Burrows et al. 2001), we arrive at a corresponding luminosity of (0.8-2.3) $\times$ 10^{-5} $L_{\odot}$. Given the system age upper limit described earlier, we estimate a mass $\leq$ 73 M_{Jup}, using evolutionary models from Burrows et al. (2001).

5.3.4 Implications for White Dwarf Companions

Resolved white dwarfs in stellar systems are especially valuable because, unlike many field dwarfs, they typically allow for reasonable estimates of luminosity, metallicity, mass and age. Studies of objects such as these are therefore crucial to our understanding of luminosity functions. They also help provide insights into system

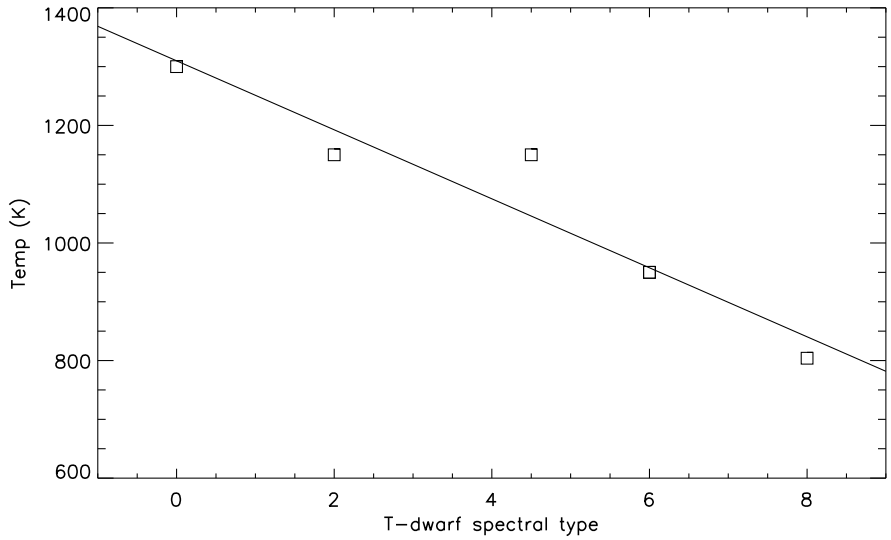

Figure 5.10: A linear fit through Leggett et al. (2002) data points of six T dwarfs. Please note that the plotted symbol at T dwarf spectral type 6 consists of two overlapping data points.

origin and evolution. For instance, discoveries of high mass white dwarfs offer opportunities to study the white dwarf mass-radius relationship as it approaches the Chandrasekhar limit. Correctly understanding such a relationship is important because observers routinely use such models to estimate white dwarf mass and radii. Furthermore, such white dwarf models play roles in fields ranging from estimating the age of the galactic disk (Wood 1992) to finding distances to globular clusters (Renzini et al. 1996).

As we continue to monitor HD150451C's near-IR colors as well as conduct spectroscopy on the companion and parent system, we will further constrain the companion's spectral classification and provide important experimental data for observational and theoretical comparisons.

5.4 Conclusions

We presented evidence for a likely white dwarf companion to the F/K V binary HD150451AB. K-magnitudes, J-K colors, and common proper motion with the primary system constrained the classification to either a white dwarf or methane brown dwarf companion. While methane band observations suggested a methane brown dwarf classification, more definitive spectroscopic observations lead us to conclude a white dwarf classification.

Chapter 6

WIRC: A Wide-Field Infrared Camera for the Palomar 200-inch Telescope

6.1 Introduction

In this chapter I describe my work in the design, fabrication, and commissioning of WIRC (Wilson et al. 2003), a state of the art wide-field near-infrared camera which serves as a full-time facility instrument for the Palomar 200-inch Hale Telescope. The instrument, whose development was led at Cornell University by Stephen Eikenberry[1] (Principal Investigator) and John Wilson[2] (Lead Scientist), uses a 9-element corrector camera to deliver an 8.7×8.7 arcminute seeing-limited field of view at the prime focus of the 200-inch telescope. As part of the development effort, I directed

[1]Current Address: Astronomy Department, University of Florida, 211 Bryant Space Science Center, Gainesville, FL 32611

[2]Current Address: Astronomy Department, University of Virginia, P.O. Box 3818, Charlottesville, VA 22903

the implementation of a filter wheel system powered by high-precision cryogenic motors. I also built the camera power supply and provided support designing and building the mechanical structures that house the electronics network and maintain a cryogenic environment. The instrument achieved first light, using an engineering grade 1024×1024 pixel Rockwell Hawaii-I NIR detector, on December 1, 2001. In the Spring and Summer of 2002, the WIRC team, in collaboration with Caltech, implemented a 2048-square Rockwell Hawaii-II NIR detector, taking advantage of a full 8.7×8.7 arcminute field with Nyquest sampling pixels (see Figure 6.1 for an example image.). The upgraded instrument achieved first light in September, 2002 and is currently a full-time facility instrument. In the paragraphs below I describe an overview of the instrument as well as detailed descriptions of my work in this development.

6.2 An Overview of the WIRC Camera*

6.2.1 Optical

Designed by Telic Optics (North Billerica, MA) with input from Cornell faculty and scientists Tom Hayward[3], John Wilson, Bernhard Brandl[4] and Steve Eikenberry, the optical design uses an all-refractive 9-lens re-imaging system to optimize wide-field observing in the *JHK* atmospheric bands (1.1 - 2.3 μm). Fabricated primarily from ZnSe, Infrasil, and CLEARTRAN (a water-free ZnS), all optical elements, with the exception of the dewar window, reside inside the cryogenic dewar at operating temperatures equal to that of liquid nitrogen.

*This section summarizes results published in Wilson et al. 2003

[3]Current Address: Gemini Observatory, AURA/Casilla 603, La Serena Chile

[4]Current Address: Leiden Observatory, P.O. Box 9513, NL-2300 RA, Leiden, Netherlands

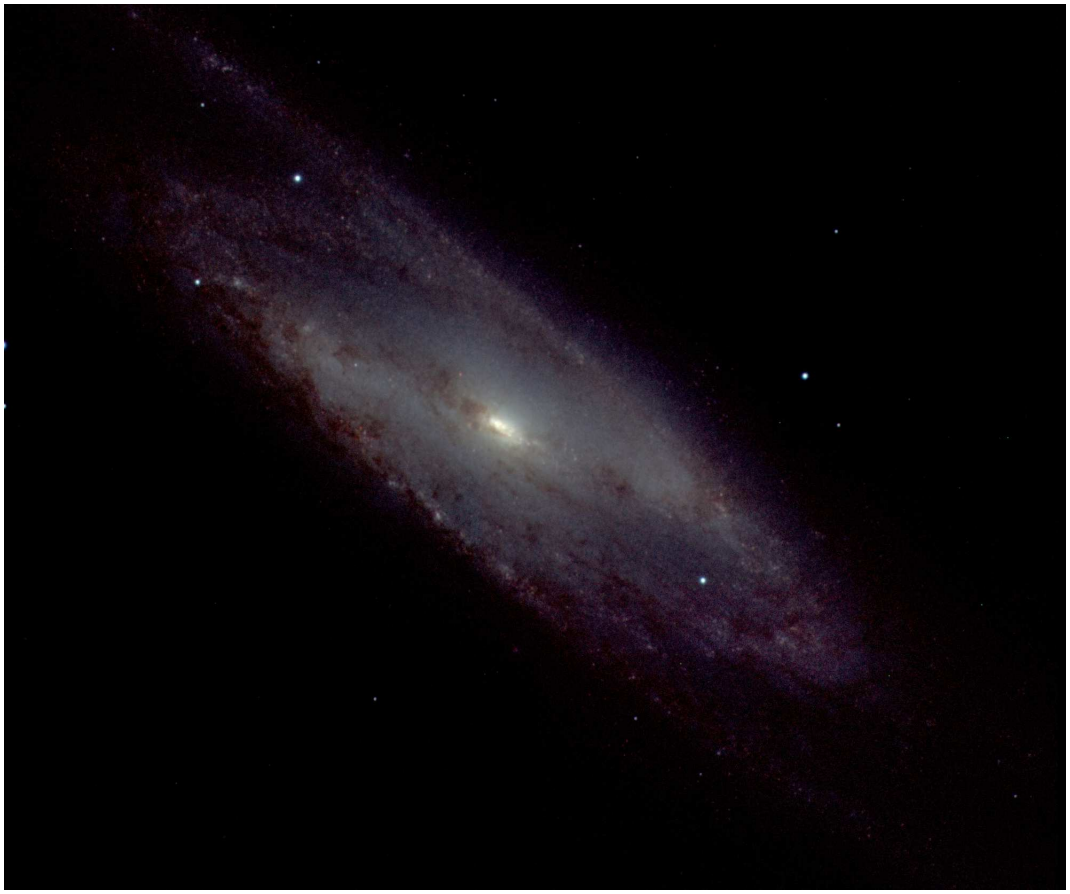

Figure 6.1: WIRC-2K Commissioning Image. Starburst Galaxy NGC 253 observed in J (blue - 3 min.), H-continuum (green - 3 min.), and K_s (red - 18 sec.) at Palomar Observatory on September 2, 2002.

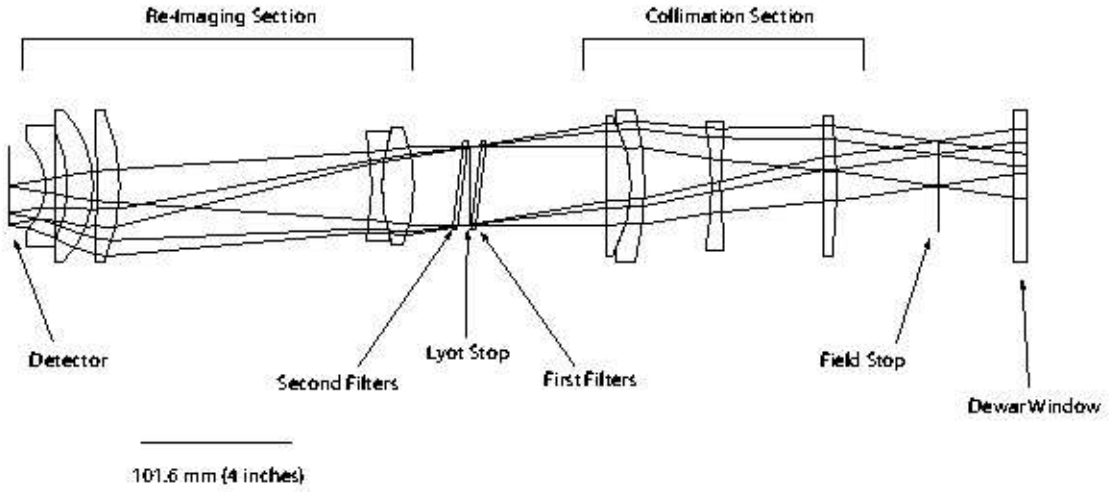

Figure 6.2: A schematic of the WIRC optical train as shown in Wilson et al. (2003). The beam enters at the Dewar window on the right and continues to the detector on the far left. The displayed beams include an on-axis beam and two beams representing the edges of the field. This image was reproduced with permission from J. Wilson.

The original f/3.3 optical beam, arriving from a reflection off the primary mirror, first passes through the dewar window and immediately comes to a focus at the field stop position (see Figure 6.2). The square-shaped field stop constrains the beam to the shape and size of the detector, located at the final focus. Passing through the field stop, the beam encounters four collimating lenses. The subsequent collimated beam continues to the two filter wheels, which flank the Lyot stop. The filter wheel surfaces, tilted at a 7 degree angle to minimize ghost reflections, contain up to 7 filters each. Following the filter wheels, five spherical lenses, including a three lens field flattener, re-image the beam in preparation for its eventual focus on the detector chip. The final f/3.0 beam reaches the array producing 0.25 arcsec per pixel imaging, slightly oversampling the typical seeing-limited point spread function.

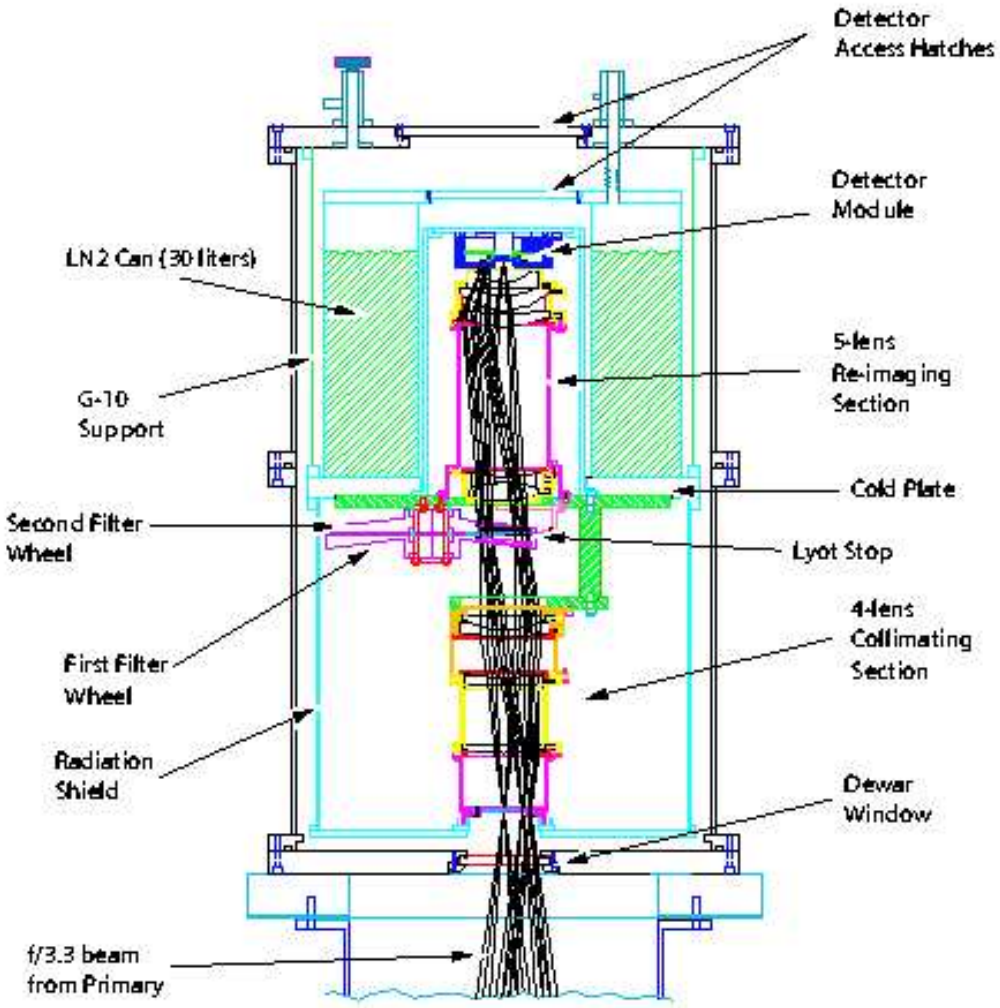

Figure 6.3: A schematic of the WIRC dewar and optics as shown in Wilson et al. (2003). Reproduced with permission from J. Wilson.

6.2.2 Mechanical

In Figure 6.3 we present a schematic of the WIRC mechanical assembly. The structure supporting the lenses takes advantage of a barrel system where the only physical connection to the rest of the dewar occurs at the cold plate. Figure 6.4 displays a photo of the barrel system removed from the dewar. The cold plate can be seen in the middle with the collimating system mounted above and the filter wheels residing below.

Figure 6.4: The WIRC dewar opened in the lab. One can see the 4-lens collimating section as well as the two filter wheels.

The two gold cylinders to the right and left of the collimating barrel represent the cryogenic stepper motors, purchased from Phytron (Waltham, MA). With a gear ratio $\sim$ 17.7:1, the stepper motors drive the $\sim$ 9.4 inch filter wheels via a drive shaft that makes contact with geared teeth on the wheel perimeters. If you have good vision, you should see in Figure 6.4 a brown rectangular-shaped mechanical homing switch, sitting to the left of the wheels just below the support pillar. One of two mechanical homing switches (one for each wheel), it is tripped by a tab protruding from the filter wheel. Since the stepper motors operate without any feedback from the filter wheels, these switches give the user an independent verification of wheel position.

One important consideration in designing precision cryogenic instruments is determining how to precisely machine a system at room temperatures when it will ultimately be undergoing thermal contraction to operate at cryogenic temperatures. To simplify this issue, the mechanical holding structure was machined entirely of aluminum, minimizing any differential contraction. We support the lenses, whose thermal contractions differ significantly from aluminum, with the following system: At room temperatures, protruding Delron pins extend out from the barrel walls, holding the filters firmly in place. At cryogenic temperatures, the pins contract away from the lenses just as aluminum supports contract snuggly around the lenses.

6.2.3 Dewar

The cold plate diameter (17.5 inch) and lens barrel height were the determining factors in dictating the dewar size. The final 19.75"$\times$32.00" dewar system holds 30 liters of LN2 with typical hold times of $\sim$ 2.5 days. Entrance hatches lie at the top of the dewar, near the detector, to allow for detector positioning adjustments

without having to disrupt optics and optical alignments. The dewar was designed by John Wilson and Steve Eikenberry in collaboration with Precision Cryogenics Inc. (Indianapolis, IN) ; Precision Cryogenics performed all fabrications.

6.2.4 Detector & Electronics

For its detector, the WIRC instrument uses a 2048×2048 Hawaii-II HGCdTe array. A 32-channel detector control system, built by B. Pirger (Cornell University) runs the detector. For the detector read-out procedure, differential signals output from each channel to an independent A/D converter. From here the signals continue to an FPGA based clocking, control, and communications board. This 32-channel system allows for readout rates $\sim$ 1 Hz. In contrast, the more commonly used 4-channel electronics systems provide readout rates $\sim$ 7 Hz.

6.3 My Contributions to the WIRC Development Effort

6.3.1 Filter Wheels

Figures 6.5 and 6.6 display the filter wheel designs, created by J. Carson with input from C. Henderson (Cornell University).[5] The models represent a compact, durable design which takes into account ease of machining while accommodating up to fourteen optical elements. The 7-degree angle of the filter mount surfaces ensures, as modeled by T. Hayward, that ghost reflections forming between the detector and the filter will end up beyond the edges of the image array. With the Lyot stop confining the beam to a 2.060-inch diameter, the outer 13% of the filter diameters

[5]The filter wheel models represent a continuation of preliminary designs by T. Hayward.

remain unused by the transmitting beam. This margin allows us to rest the outer 0.1 inches of the filter diameters on the filter wheel mount shelves without causing any vignetting. At the same time, a remaining 0.1 inches of non-illuminated filter diameter allows forgiveness in the case of positioning or machining errors.

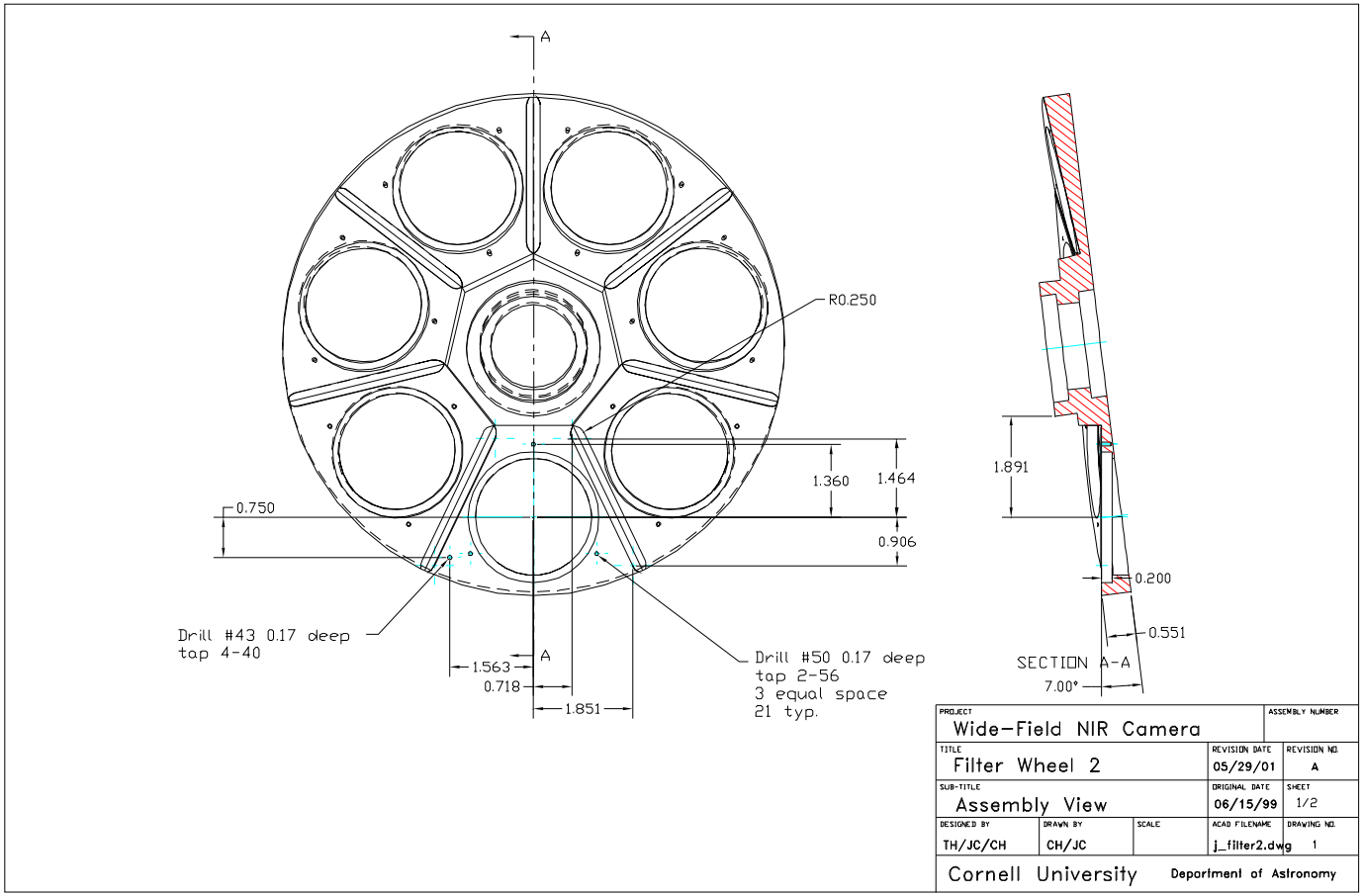

Figure 6.5: Fore Filter Wheel Schematic.

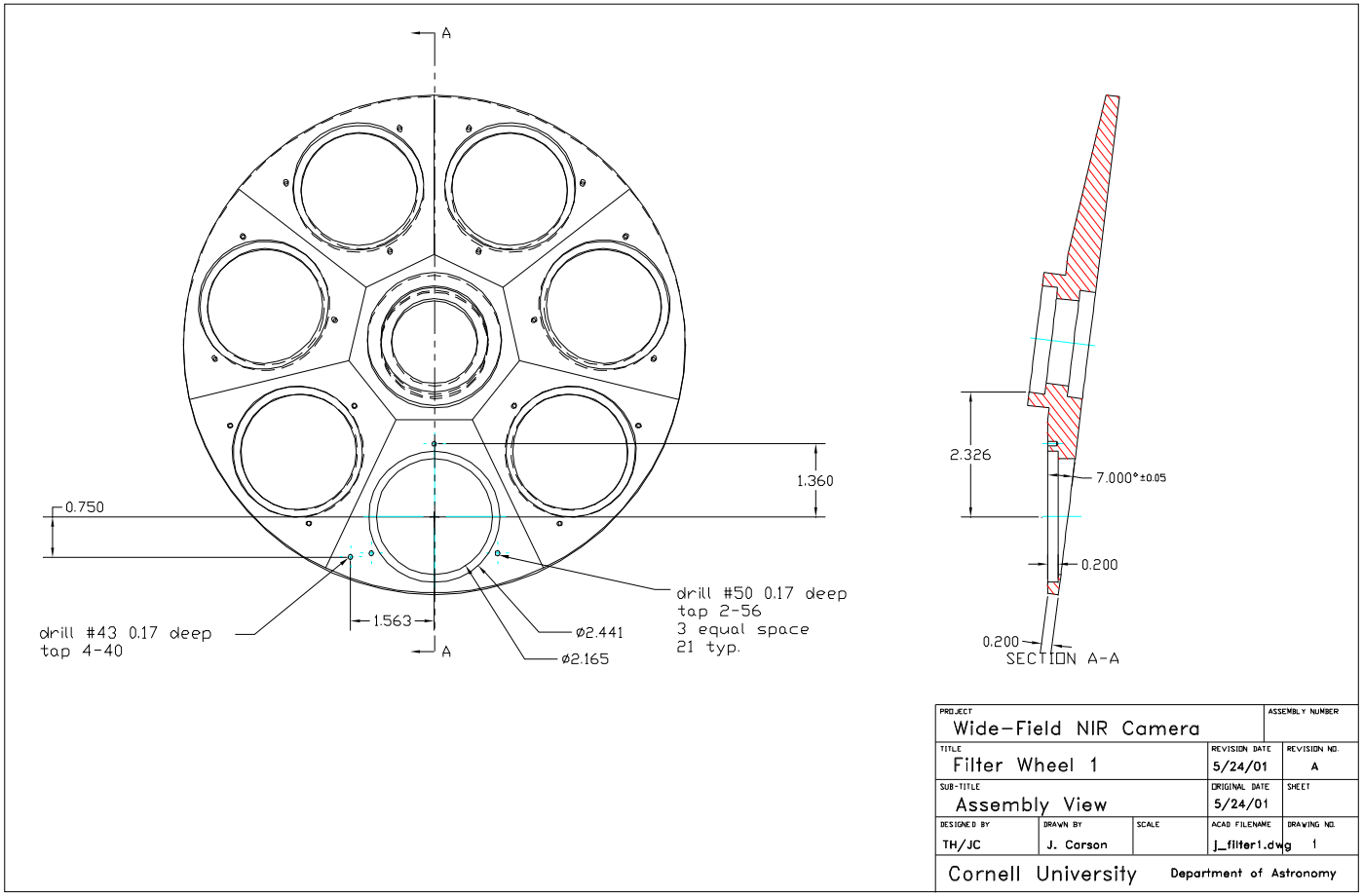

Figure 6.6: Aft Filter Wheel Schematic.

For the fabrication process, we first commissioned Cornell's Clark Hall Machine Shop to manufacture two copies of the wheel blank shown in Figure 6.7. Next we shipped the wheel blanks to Allied Devices (Hicksville, NY) where 672 teeth (72 pitch) were cut into the wheel perimeter. Finally, we returned the geared wheel blanks to the Clark Hall Machine Shop where the final specifications shown in figures 6.5 and 6.6 were completed. Since the latter Clarke Hall machining procedures required the most precise specifications, we chose to complete that stage last. That way, we did not have to worry as much about subsequent handling (like machining of teeth) altering any of the specifications.

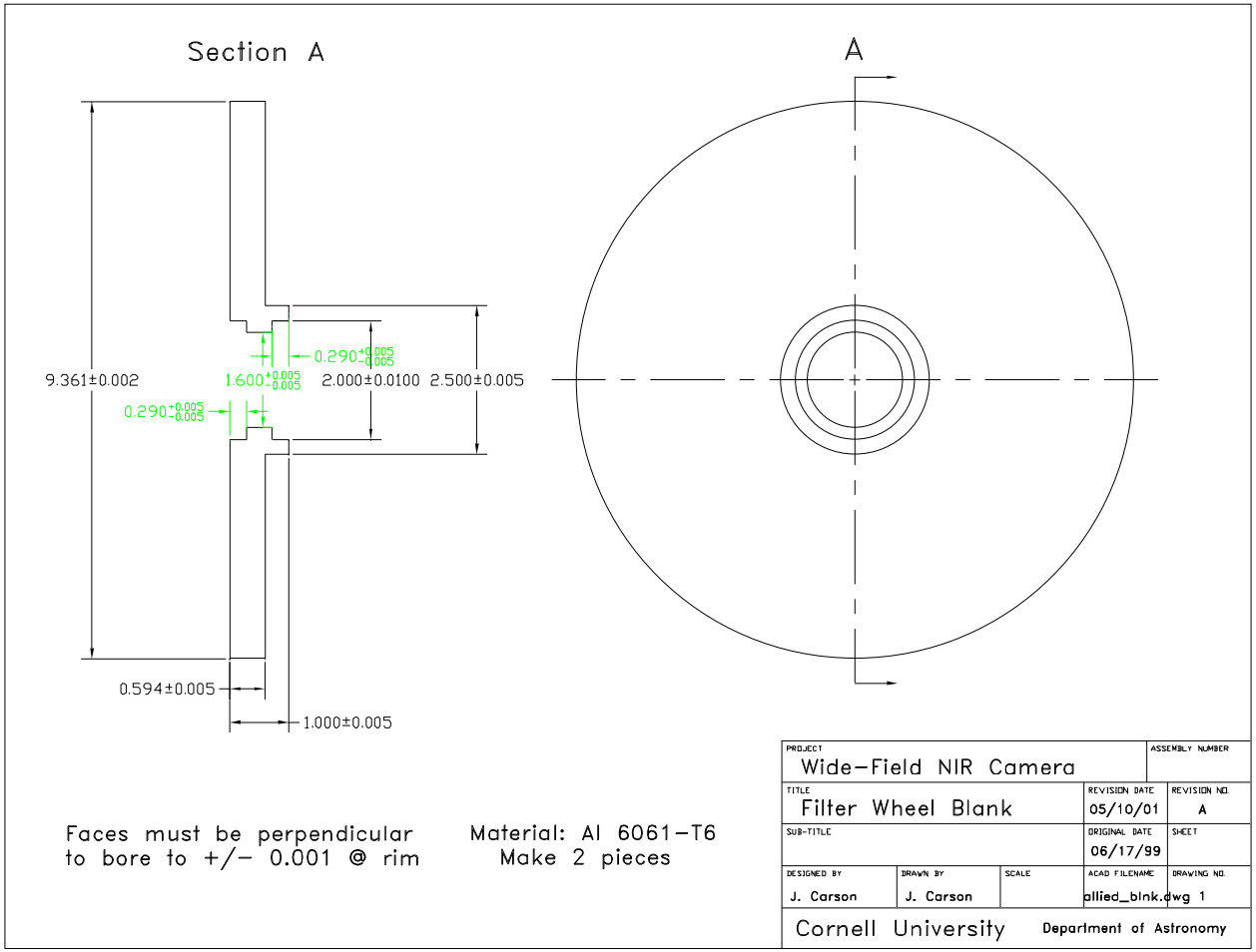

Figure 6.7: Filter Wheel Blank

Filter Wheel Homing System

Our design and fabrication of a homing mechanism went hand in hand with filter wheel development. Figure 6.8 shows the specifications for our two actuators, which provided the trips for our mechanical limit switches. Each of these actuators screwed into the bore in figures 6.5 and 6.6 labeled "drill #43 0.17 deep." The actuator's 7-degree slope (see Figure 6.8) allowed for the actuator contacting side to lie co-planar to the mechanical switch arm surface. Additionally, the actuator's rounded contacting surface allowed for a gradual depression of the mechanical switch as the actuator passed. This helped reduce mechanical stresses on the switch while also creating a finer-resolution time window for the switch's circuit connection. Figure 6.9 displays the clamp we designed to suspend our homing switch just over the edge of the filter wheel. The two joining pieces of the clamp attached to the cold plate posts seen in Figure 6.4. The mechanical switches then bolted to the bores labeled "Drill #36 thru" in Figure 6.9.

Filter Wheel Mounting Setup

Slip-fitted[6] into the central bore of each filter wheel were two 2-inch stainless steel doughnut-shaped wheel bearings (Precision Ball Bearing SSRI-543EER). The central cavity of each bearing then slip-fit to a stationary central post, allowing the wheels to rotate while the central post remained steady. To ensure that the wheel bearing lubricant operated properly at cryogenic temperatures, we processed our bearings at E-M Corporation (New Britton, CT), where the original lubricant was removed and replaced with Microseal 200-1, a lubricant known for its effectiveness at cryogenic temperatures.

[6] "Slip-fit" refers to the object being inserted at a tight fit. The object then remains securely in place by virtue of friction.

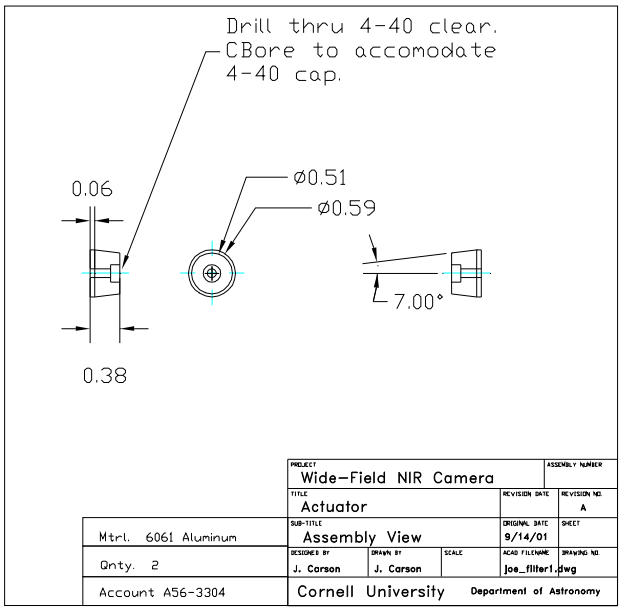

Figure 6.8: Filter Wheel Actuator

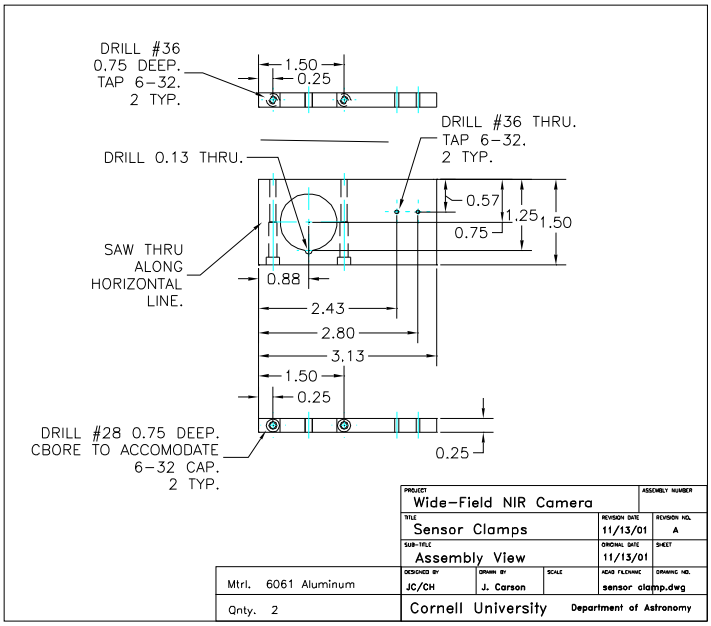

Figure 6.9: Microswitch Clamp

Filter Mounts

The filter wheels shown in figures 6.5 and 6.6 each possess seven circular depressions to hold the filters in place. To ensure that the filters remained secure, we fitted the top of each filter with a circular retaining ring (see Figure 6.10). We placed a filter support ring (see Figure 6.11) below each filter to ensure that all edges of the filter were supported evenly. A thin ring of black construction paper separated each ring surface from the filter surface. This helped safeguard against abrasions between the aluminum rings and the filter surfaces. We held each retaining ring in place with three tabs of indium, which bolted to the three bores surrounding the filter depressions. The protruding ends of the indium tabs fit into the retaining ring notches shown in Figure 6.10. The gentle pressure applied by the indium pieces kept the retaining rings and filters securely in place.

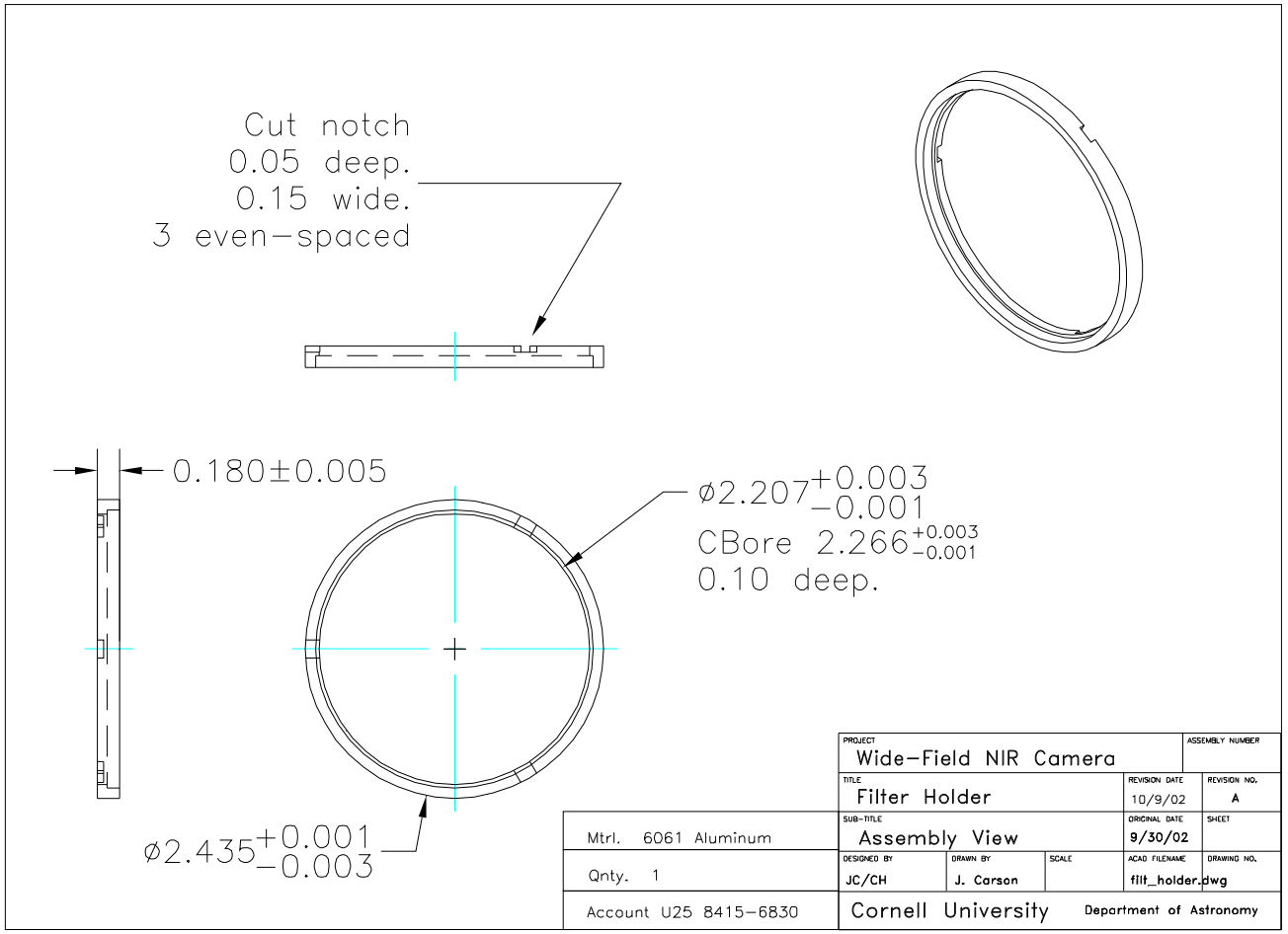

Figure 6.10: Filter Retaining Ring

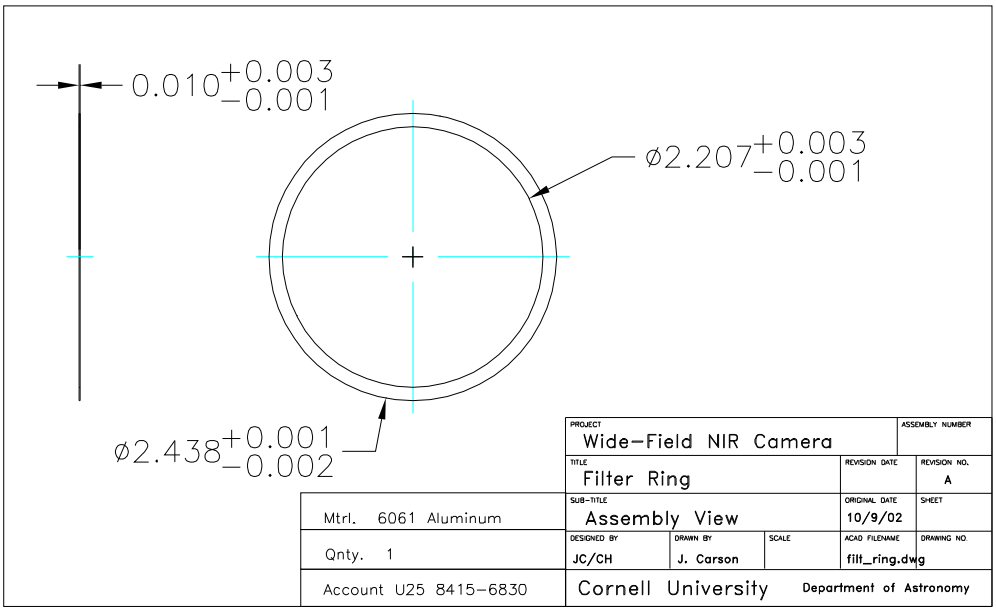

Figure 6.11: Filter Support Ring

6.3.2 Cryogenic Motors

For selecting our cryogenic motors, we considered factors such as torque, drive current, rotational accuracy, and rotational speed. Generally, higher torque entails higher current. In our case though we needed to balance a need for high torque, ensuring easy wheel movement, with a desire to minimize the current which can result in heat emission inside our cryogenic dewar. Calculating the theoretical torque required to turn a frictionless ∼9-inch wheel, we found that this level of force was minor when compared to even the smallest Phytron motor torques (∼1 mN m). The torque though that might be required to provide the first push into motion, considering possible sticking between contacting frozen gear surfaces, might be significantly larger, as well as difficult to predict. Therefore, we reverted to previous experiences with cryogenic filter wheels and chose a VSS 42.200.1.2-UHVC motor with a quoted maximum torque of 7 mN m. B. Brandl's experience with similar

systems led us to believe that this was an adequate torque level. With a maximum speed ∼30 rotations per minute, we estimated a wait time about 1 minute for a complete filter wheel rotation. Previous experience also informed us that required currents would not significantly adversely affect our cryogenic environment. Along with this VSS 42.200 motor, we also used a slightly stronger VSS 43.200.1.2-UHVC motor, which became available as a donation from G. Stacey (Cornell University). Each motor turned at a default rate of 200 steps per revolution with a capability of running in half-step mode. With a 17.7:1 gear ratio between motor and filter wheel, each full step corresponded to a 146-micron increment at the center of the filter. Accordingly, half-step mode allowed for 73-micron increments at the filter center. Since our oversized filters gave us $\sim$ 2.5 mm (0.1 inches) of leeway in filter positioning (before vignetting began), both half-step and full-step accuracies provided sufficient resolution. We eventually chose to use full-step mode since on-telescope testing demonstrated that this caused the smoothest movement of filter wheels. The motors operated with a maximum 1.2 Amp/phase drive current. Both motors were designed by Phytron to operate at temperatures as low as -270° C and pressures down to 10^{-11} Torr.

Effects of Motor/Filter Wheel Positioning Errors on Resolution and PSF Stability

While we felt confident that our resolutions were adequate to avoid vignetting errors, we also wanted to make sure that filter positioning errors would not magnify adverse effects from the filter's own transmission variations. These variations might include inhomogeneities within the filter or dust particles residing on its surface. While flatfield data may correct these effects for a stationary filter, they may not be able

to fix such an effect if the filter position changes without a new flatfield being taken. To predict the impact of such effects, given our positioning uncertainties, we wrote IDL codes to quantitatively describe how filter wheel positioning errors may alter PSF shape and stability.

Dividing a theoretical filter plane into a little over a million elements, we assumed a 2% rms error in the cells' transmission levels. Additionally, we assumed that our array was scattered with 25 randomly positioned 0.4 mm diameter dust particles. We modeled each dust particle as providing a complete blocking of flux across its diameter. In other words, any cell with an overlapping dust particle had a transmission level of zero. Next we created an identical-sized array with a Gaussian-shaped PSF at its center. After Fourier-transforming this focal plane star-like image into the filter plane[7], we multiply the transmission array by our PSF array. Finally, we Fourier-transform the resulting PSF array back into the image plane.

For comparison, we repeated this procedure, only this time we shifted our transmission array by the equivalent of a 0.4 mm shift of the filter wheel. Incidentally, this shift corresponds to ~ 3 step error in our motor positioning (assuming full-step mode). We then compared the resulting focal-plane PSF image to the PSF image created with the original non-shifted transmission array. Measuring the power in a 3-sigma aperture centered on the original PSF center, we found that our filter wheel shift caused a 0.04% change in recorded power. The shifted array also resulted in a change in the gaussian-fitted PSF center of 0.05 pixels (out of a detector focal plane image 1024×1024 pixels). Thus, we concluded that, given typical uncertainties associated with science observations (i.e. background noise, Poisson noise, etcetera), errors from filter positioning errors would be effectively insignificant.

[7]Recall that our filters are effectively located at the pupil plane. Therefore, we assume that the filter plane and the pupil plane are identical.

6.3.3 Motor Controller Box

Figure 6.12 displays the contents and wiring of our Motor Controller Box. The FORE and AFT motor controllers are SINCOS D-32 Stepper Drivers. Attached D-32 connectors allow for convenient wire connections. Signals and currents to and from the PHARO Electronics Box pass through a 41P KPT Panel Mount. Signals and currents to and from the dewar pass through a 19S KPT Panel Mount. The power supply enters from the Power Supply Box through the 16P KPT Panel Mount. The Buffer Board, designed and built by B. Pirger, isolates all dewar currents from the currents that encounter the PHARO Electronics Box and Power Supply. This helps prevent unwanted ground loops traveling between the dewar and outside electronics. The electronics systems are enclosed within an LMB/Heeger 13.3-inch×13.8-inch×5.25-inch aluminum chassis. All subsequent bores and machining modifications (see figures 6.13 through 6.15) were performed by J. Carson.

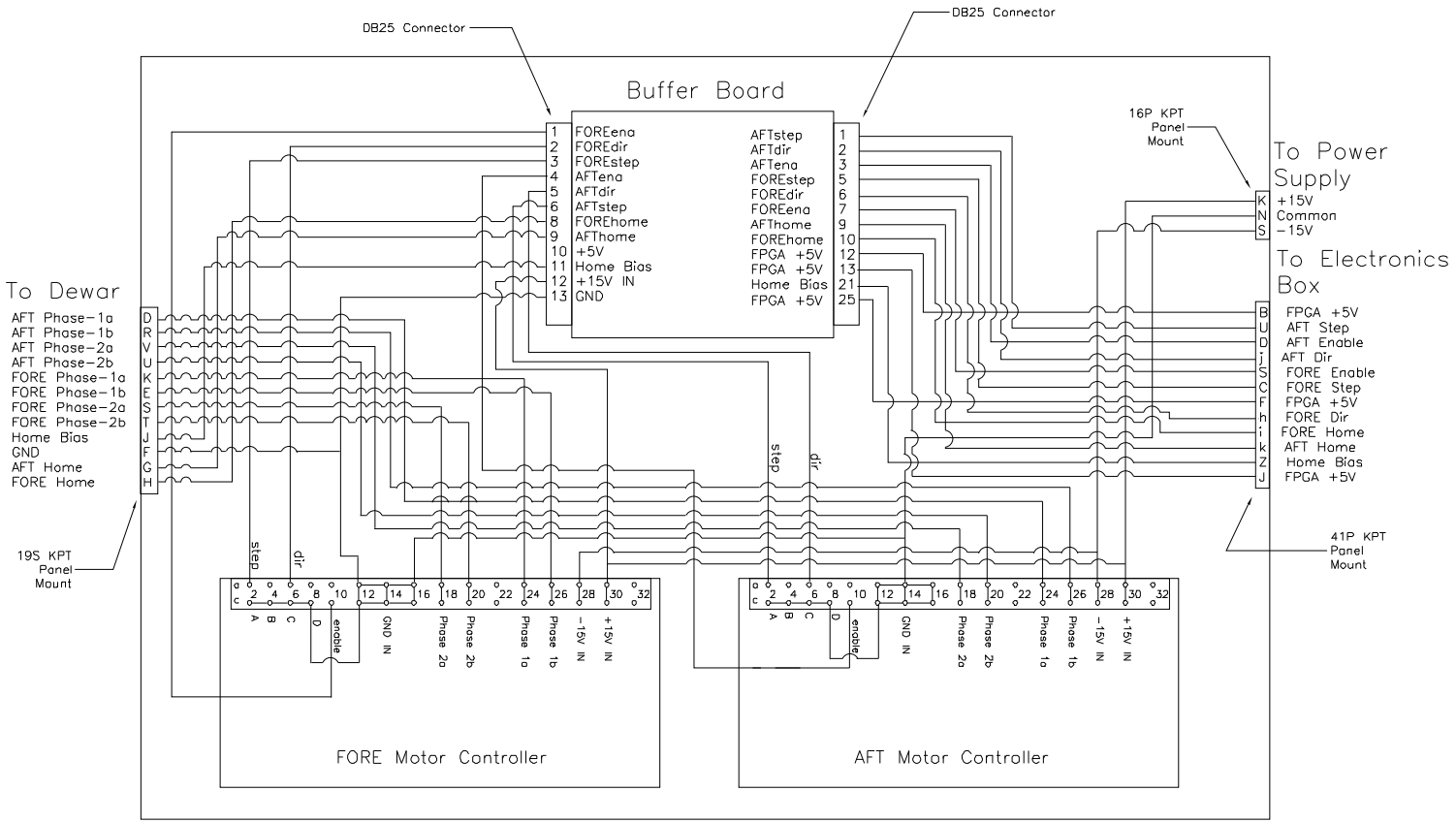

Figure 6.12: Motor Controller Box

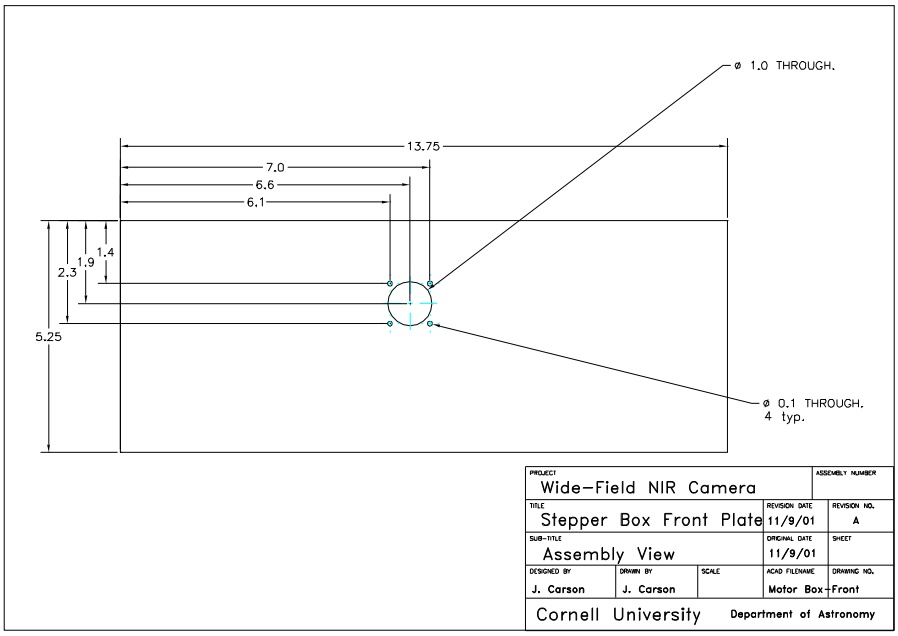

Figure 6.13: Motor Controller Box Front Plate

6.3.4 Power Supply

Figure 6.16 shows the layout of our power supply box. The large rectangular shapes represent the individual power supplies. The ($\otimes$) symbols represent the 0.19-inch bores added so the power supplies could bolt into place. The Jones board performs no special function other than providing us with tabs where we can neatly combine or split currents to transmit to their respective destinations. Toward the top of the drawing we see our cooling fan, which draws air through the system to safeguard against overheating. The 0.9-inch holes in Figure 6.17 provide intake and outtake openings for circulating air. The displayed EMI filter, 4A fuse, and KPT panel mounts all reside on the power supply box front plate displayed in Figure 6.18. The set of eight 0.5 inch bores, stationed in the upper middle and right, support on/off switches as well as light bulbs which illuminate when a switch sits in the on position. Three of the switches allow the user to individually transmit or cut power to the

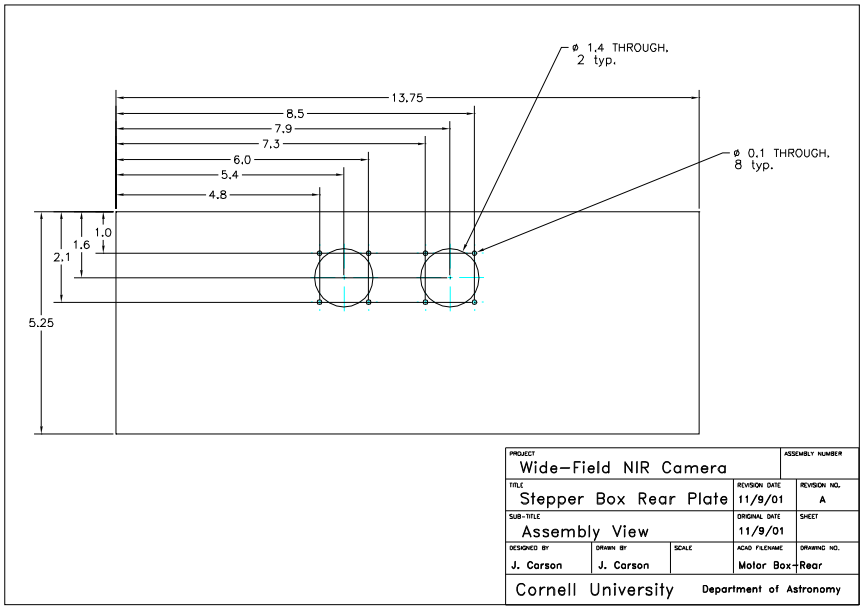

Figure 6.14: Motor Controller Box Rear Plate

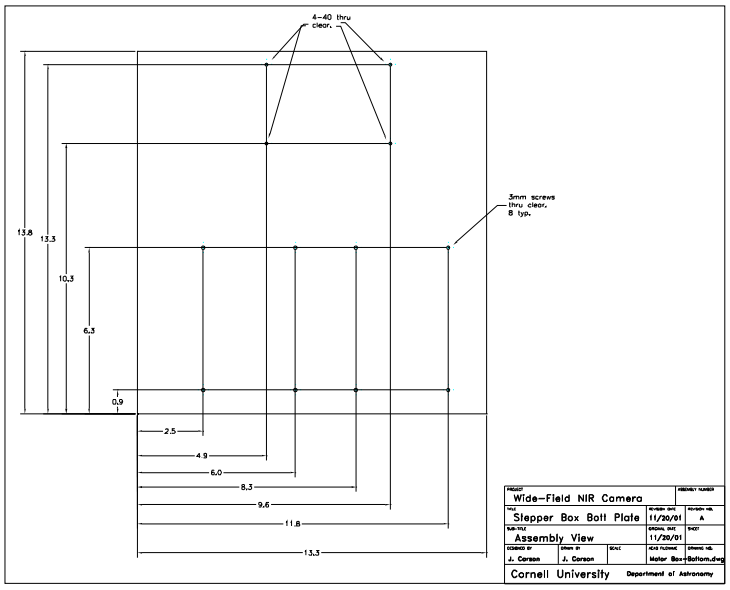

Figure 6.15: Motor Controller Box Bottom Plate

Vacuum Sensor, Motor Controller Box, or PHARO Electronics Box. The fourth switch is a main power switch which connects or cuts the AC power to all of the power supplies. All plates, including the top plate and two side plates not shown here, were purchased from LMB/Heeger (Commerce, CA) as a non-assembled box chassis (part # UPR71714).

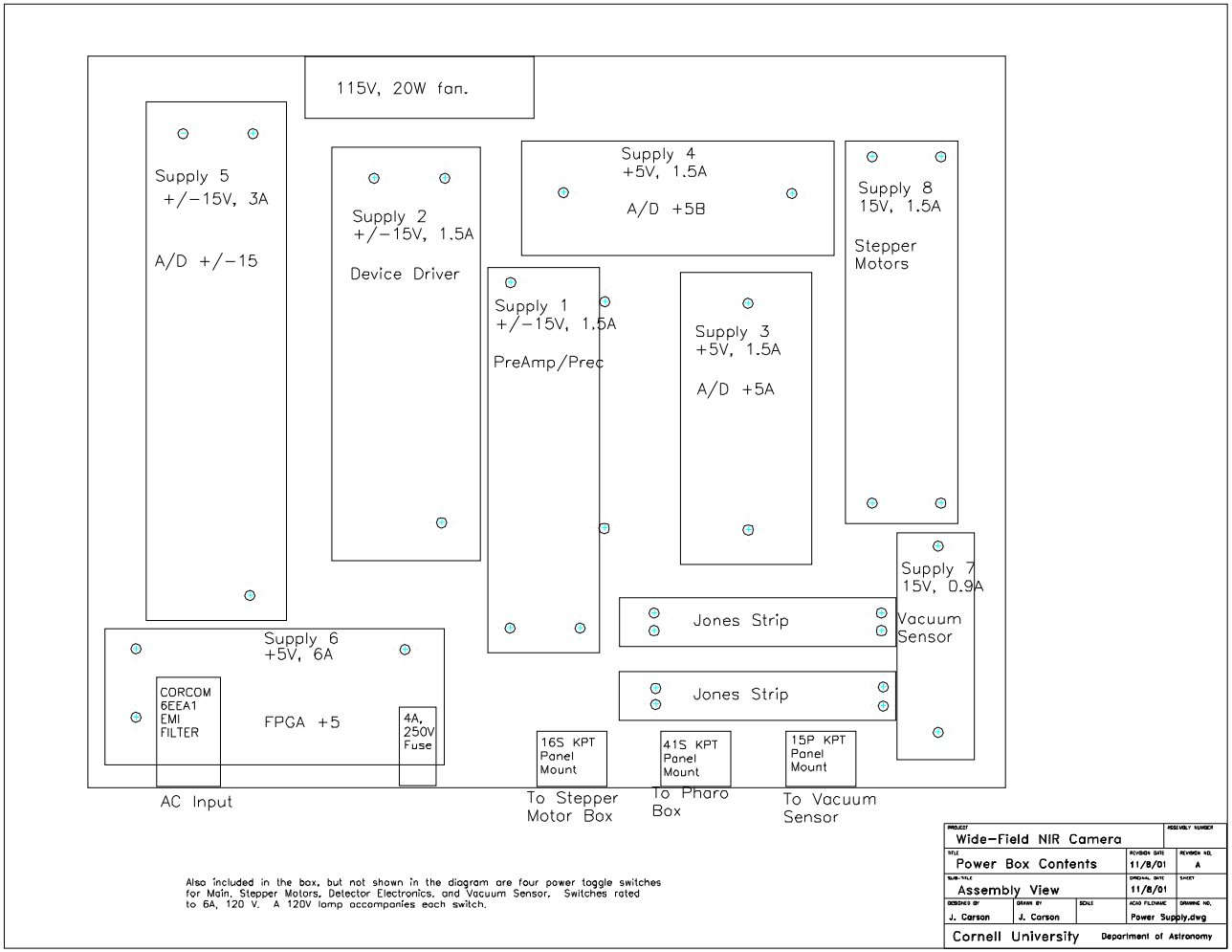

Figure 6.16: Power Supply Box

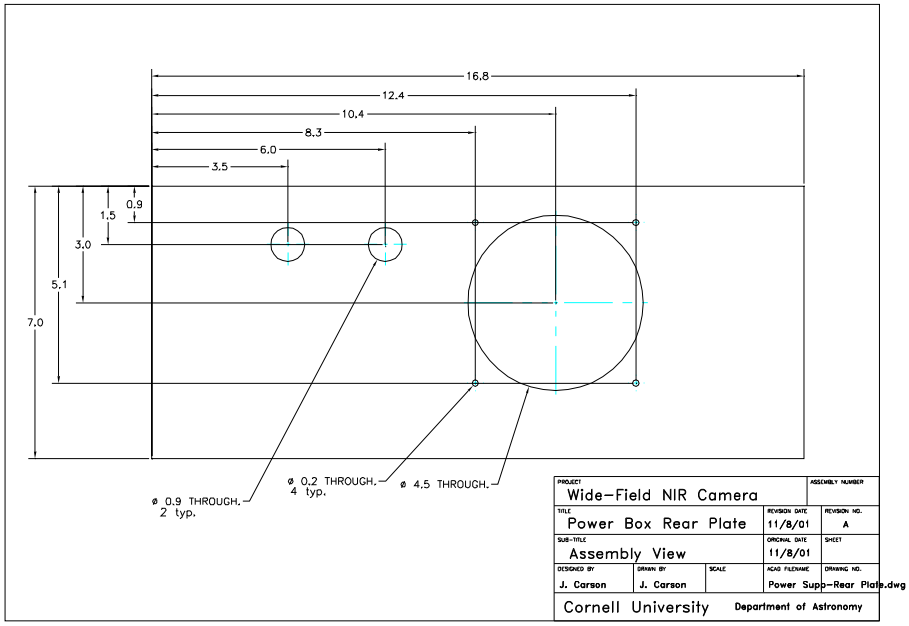

Figure 6.17: Power Supply Box Rear Plate

Our current flow begins at the AC input/EMI filter shown in Figure 6.16. This socket connects with the standard 120 V AC wall socket. Our EMI filter helps secure against unexpected spikes in AC current. Following the EMI filter, the AC current encounters the 4A fuse. Our fuse helps protect our system against power surges or unexpected current shorts. After encountering the fuse, the AC current continues to the main power switch. From here, the current travels to the Jones board where the AC power splits off to the Vacuum Sensor, PHARO Box, and Stepper Motor Box switches. From there, the lines return to the Jones board where they separate off to the appropriate power supplies. All AC grounds connect to the Power Supply Box aluminum structure and wall socket Ground. From the power supplies, the outputted DC currents return to the Jones board where they split off to the appropriate KPT pins. All outputted DC Common signals remain isolated from one another except for supplies 4 and 5 which tie together. All wiring was done with Teflon-coated 20 AWG wire. All assembly, machining, and wiring was

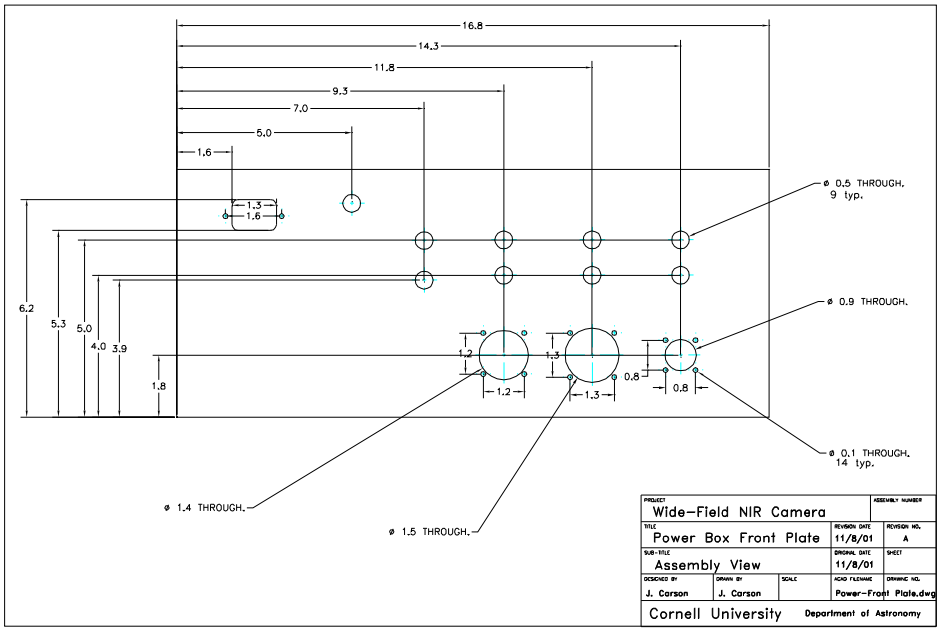

Figure 6.18: Power Supply Box Front Plate

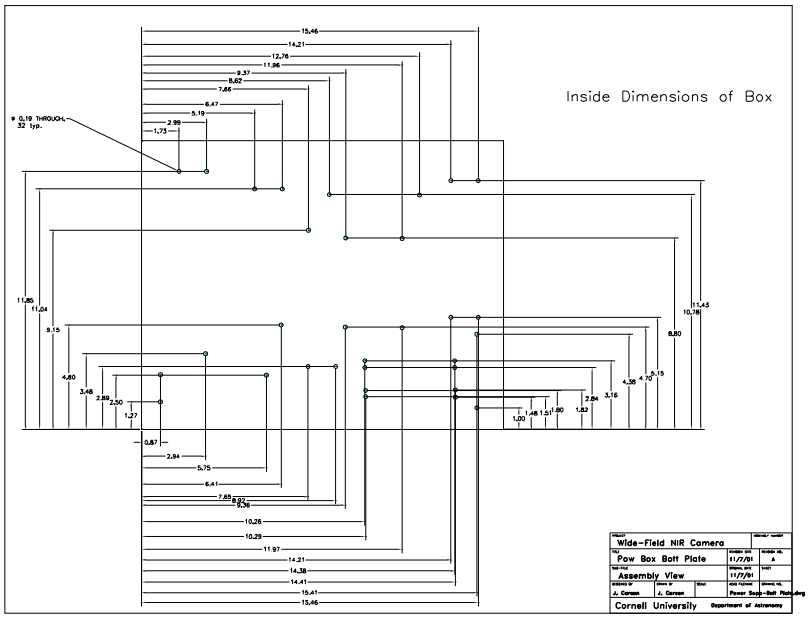

Figure 6.19: Power Supply Box Bottom Plate

performed by J. Carson.

6.3.5 Power and Communication Cables

Figure 6.20 displays the five communication and power cables I designed for the WIRC camera. Figures 6.21 through 6.23 show the different signals and power supplies transmitting through these cables. Cable 2 holds twelve lines connecting the PHARO electronics to the controller box. Six of the lines are devoted to sending instructions to the motor controllers. Of these six, "AFT step" and "FOREstep" deliver square pulses to control the number of steps that the motor shaft rotates. Two additional motor current lines ("AFTena" and "FOREena") carry TTL signals instructing the PHARO electronics to disable the motor currents when the wheels are stationary. "FOREdir" and "AFTdir", similarly, are TTL currents dictating motor rotational directions. In addition to these six instructional lines, two lines carry TTL signals from the dewar's homing switches.

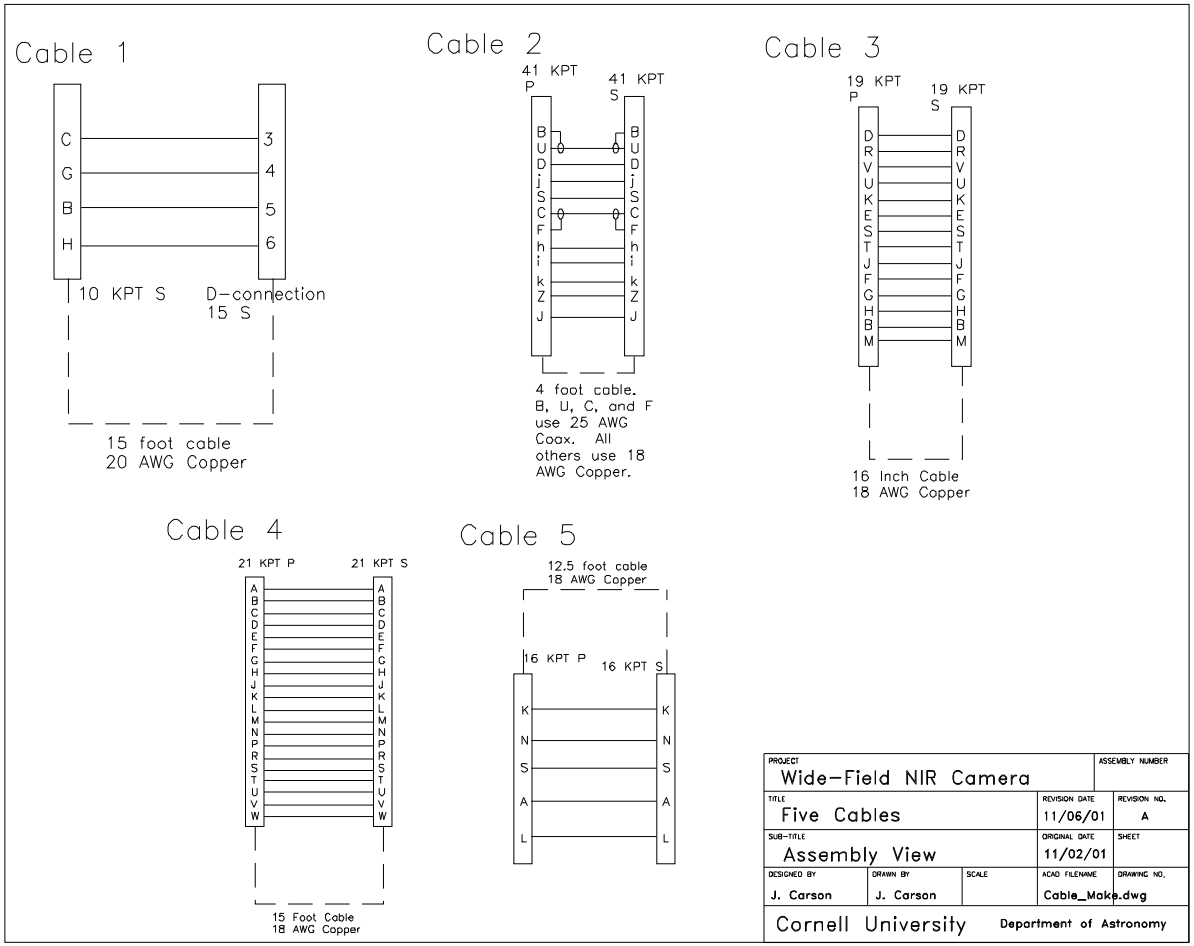

Figure 6.20: WIRC Cables

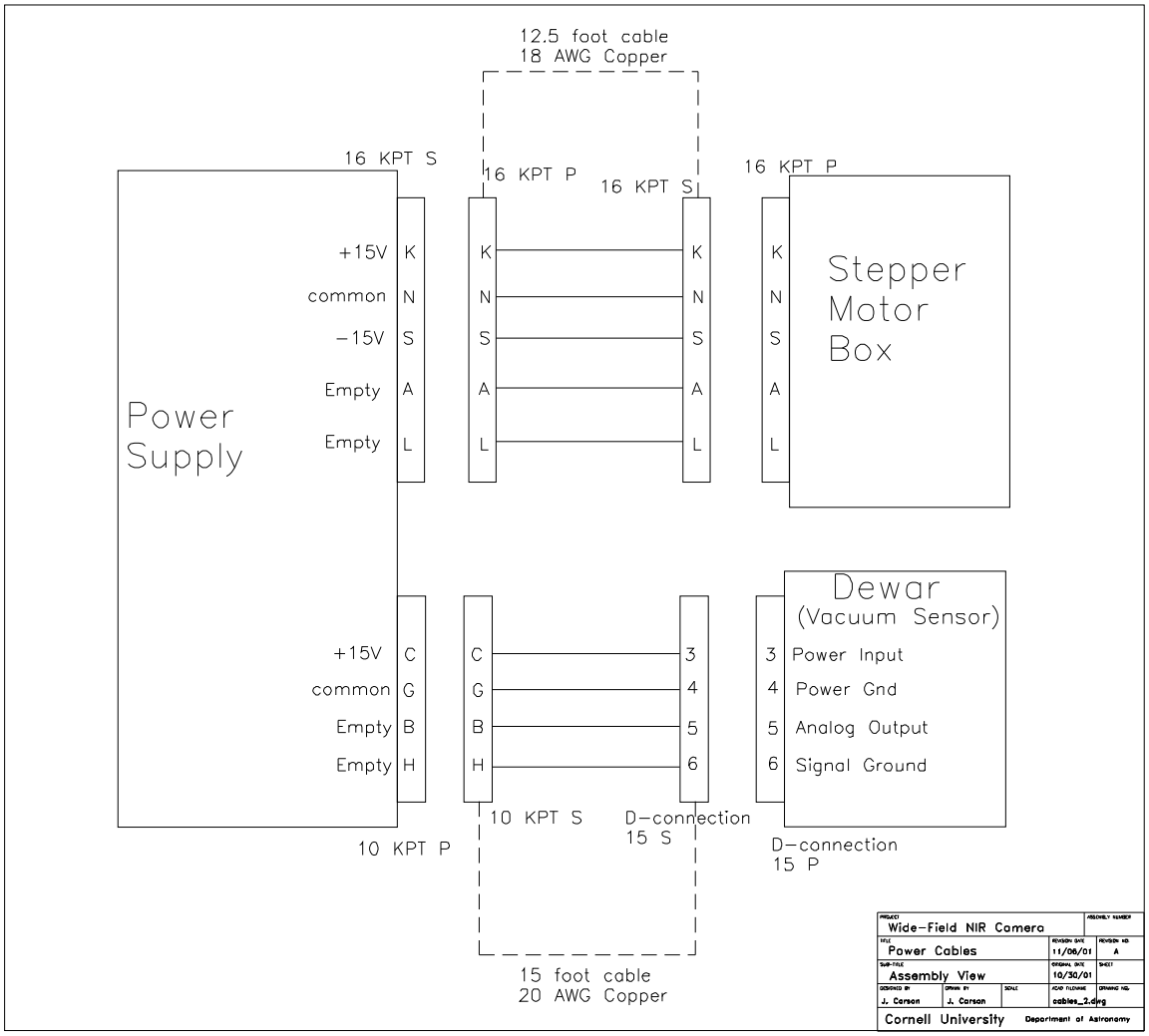

Figure 6.21: Cable 1 and Cable 5

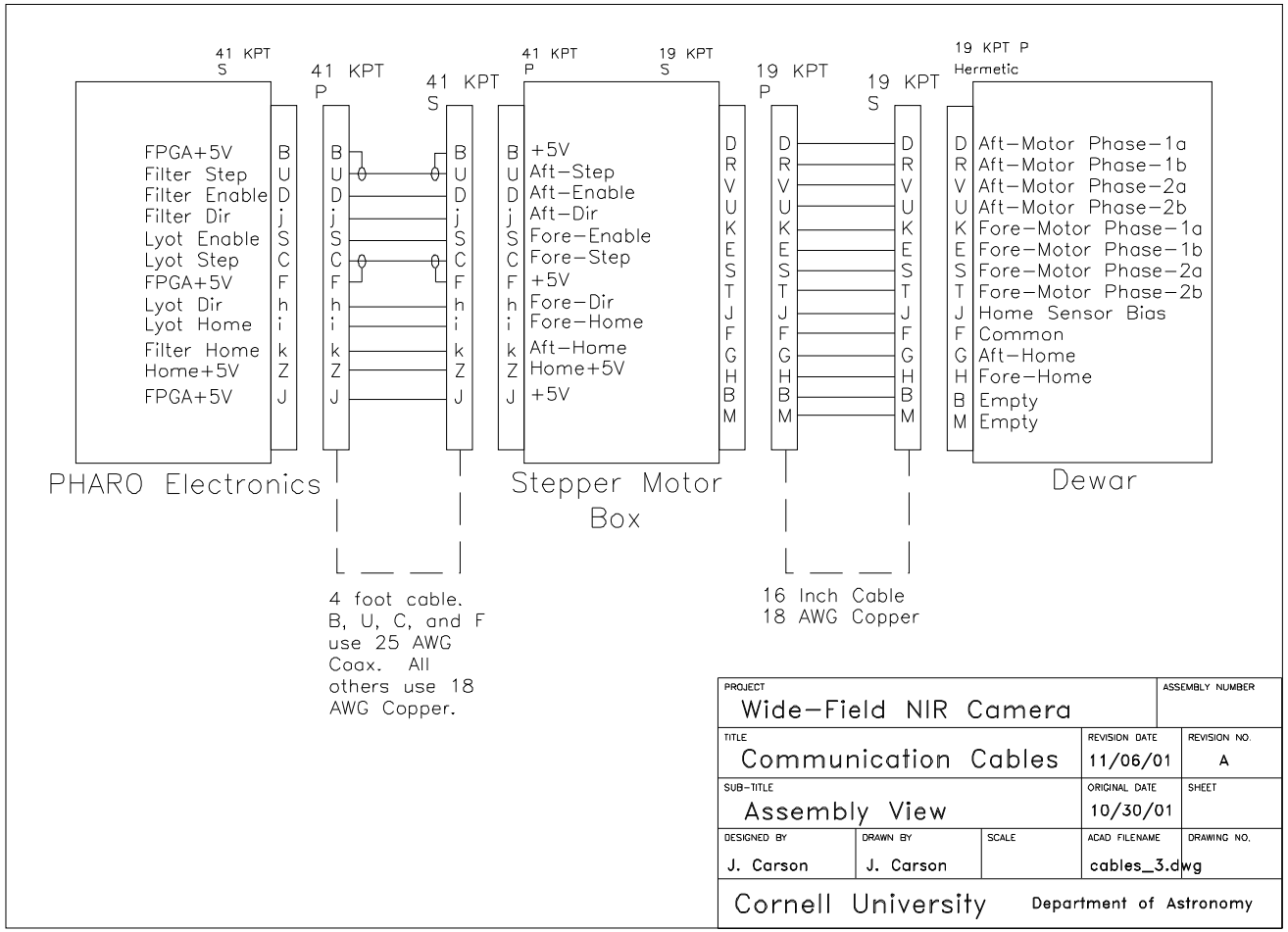

Figure 6.22: Cable 2 and Cable 3

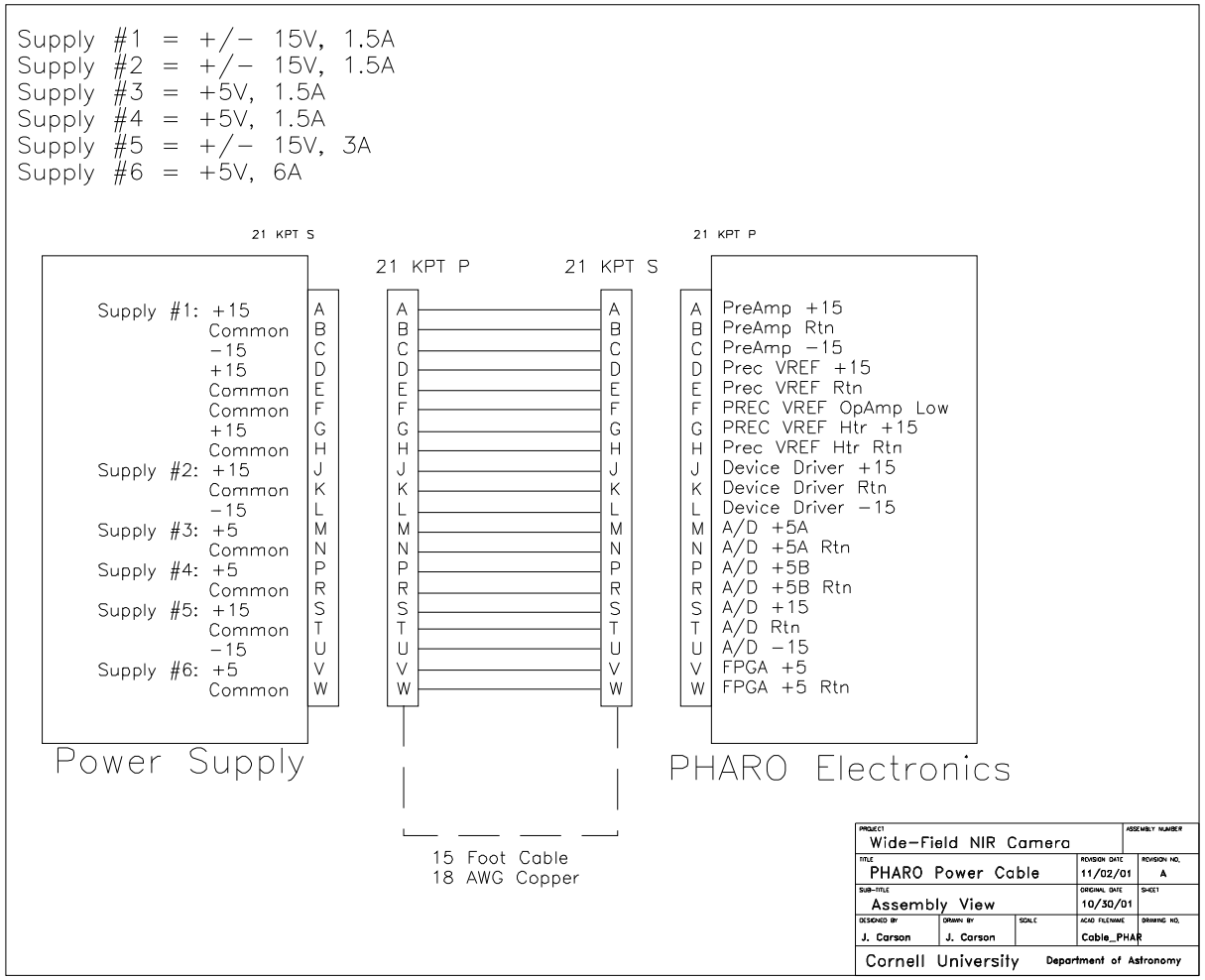

Figure 6.23: Cable 4

Cable 3 possesses the processed counterpart of the cable 2 signals after they have been translated through the controller box. Eight of these lines carry linear phase currents to drive the motors. "Home Sensor Bias" and "Common" carry TTL high and low voltage values. Cables 1 and 5 deliver power supplies to the Stepper Motor Box and Dewar Vacuum Sensor respectively. Cable 4 carries power from the power supply to the PHARO Electronics Box.

When designing these cables I considered the following questions: How important is it to shield our lines from magnetic interference? How thick must our wire be to carry all of our current without creating significant heat? How do we ensure that our cables are durable over the lifetime of the instrument? How do we ensure a sturdy connection between the cables and the connecting electronic systems?

With regards to cable shielding, we considered the effects that adverse magnetic fields might have on the various signals and currents in our wires. We reasoned that all wires delivering linear current would be relatively unharmed by adverse magnetic fields. For instance, our homing switch relies on a TTL signal of either 0 or 5 Volts. A sudden change in voltage by a few tenths of a Volt, due to a stray magnetic field, should not affect the electronic board's deciphering between 0 and 5 Volts[8]. This reasoning also applies to the current driving the motors. Since the motor controllers are linear drivers, as opposed to chopping, the effects of a slight change in the current should be minimal. Taking these considerations into account, we concluded that the clock lines between the PHARO Box and Motor Controller Box were the only lines where magnetic fields were a significant concern; Since the PHARO Box delivers a pulsed signal through the clock lines, an unwanted magnetic field could conceivably cause the Motor Controller Box to miss one or more steps. This would cause an

[8]Nominally, a TTL high equals +5V and TTL low equals 0V. Real TTL circuits will typically read anything less than +0.8V as low and anything greater than +2.4V as high.

error in filter wheel positioning. To avoid this problem, we used coaxial cables for the clock lines with the outer layers held to voltages of +5V. We chose the +5V level, as opposed to a more commonly used grounded outer layer, in order to isolate our PHARO Box Ground from the Motor Controller Box Ground. The isolation of grounds helps minimize unwanted ground loops (i.e. a non-zero current traveling from the PHARO Box to the inside of the dewar through our ground lines).

We determined our wire thicknesses primarily by the stock of cables we had left-over from previous projects. These included cable sizes of 18, 20, and 25 AWG. Current ratings for each of these sizes told us that all of our expected currents were small fractions of the wires' maximum current limits (at which point significant heat loss may occur). We set aside our 25 AWG cable for the clock lines, since the 25 AWG cable was coaxial. We set aside our 20 AWG cable for one of our 15-foot long cables. We reasoned that the longest cables were most likely to experience wear and tear. Therefore, a thicker wire would provide more durability. Having used all of our 20 AWG wire for a 15-foot long cable, we designated our 18 AWG wire for all of the remaining cables.

For all of our connections, with the exception of the manufacturer-designed Dewar Vacuum Sensor input, we used "military style" KPT connectors, purchased from Spacecraft Components (North Las Vegas, Nevada). Experience with previous instruments at Palomar told us that these stainless steel connectors were exceedingly durable and reliable. Furthermore, by choosing appropriate types (i.e. male, female, 19-pin, 14-pin, etcetera), we ensured that a user could never inadvertently attach a cable to the incorrect input. Once we concluded these designs and gathered the components, we commissioned Kippola Electronics (Newfield, New York) to perform the final assemblies. Kippola Electronics combined the wires and connectors and

encased the wires in semi-flexible heat-resistant plastic casings. The casings helped ensure durability through the projected instrument lifetime.

6.3.6 Communications Setup Between the Dewar, Motor Controller Box, and PHARO Electronics

In addition to the communication signals mentioned in the previous sections, the PHARO electronics have two inputs that receive signals from the dewar's homing switches (see Figure 6.24). A low TTL signal indicates that a filter wheel has reached its home position and the switch has been tripped. As mentioned earlier, all of the the communication lines pass through the motor buffer board before interfacing with any electronics in the dewar or motor controllers. The motor buffer board, built by Bruce Pirger, uses optical isolators to separate PHARO current from the current in the dewar and motor controllers.

The motor controllers receive instructions from the buffer board and translate them into motor phase currents which pass to the motors in the dewar. The controllers' external programming connections determine the number of motor steps per revolution. In Figure 6.12, connections are configured so that the motors run in full-step mode. This equates to 200 steps per motor revolution. Combined with a 17.7:1 gear ratio, this equates to 146-micron increments at the center of a filter.

Power supply outputs of Ground, +15V, and -15V power the motor controllers. Since only one motor moves at at time, one 1.5A power supply was more than sufficient to drive both motors (which each require up to 0.6 Amps of current). In addition to the +/-15V output, a +5V output, generated by the buffer board, configures the controllers' external programming connections (labeled A, B, C, and D in Figure 6.12). The homing switches (see Figure 6.24) also receive their TTL high

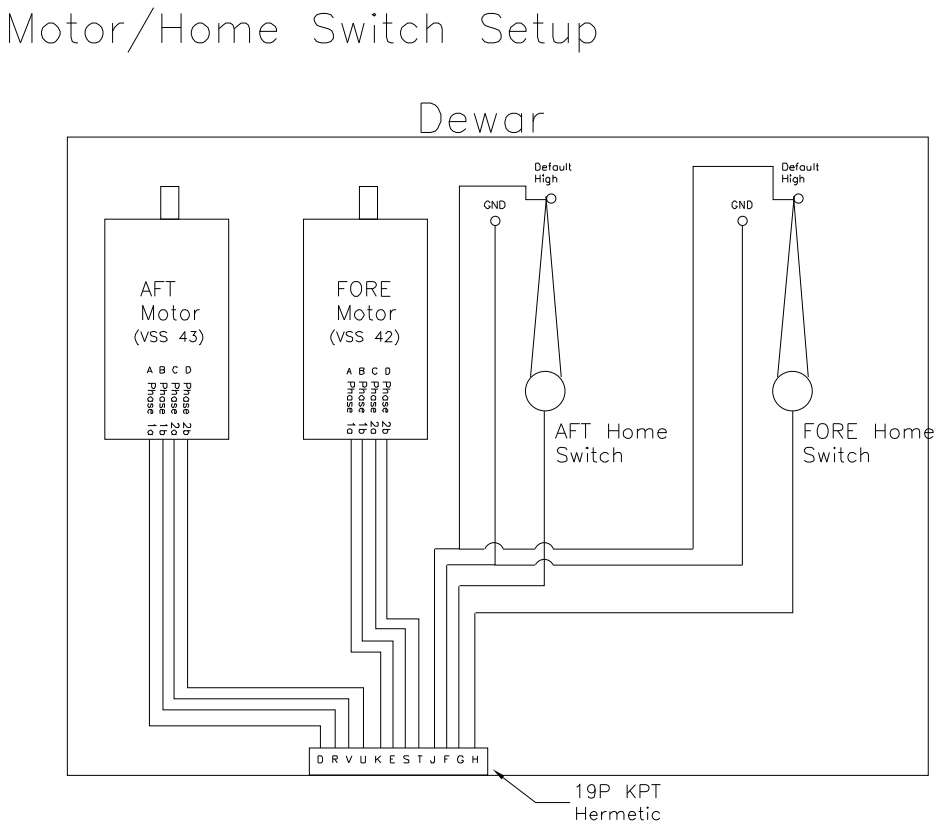

Figure 6.24: Motor and Homing Switch Setup

voltages from the buffer board's 5V output. We keep the switches' default positions at high so that any shorting problems in the circuit may easily differentiate from filter wheel positioning errors: That way, a shorted circuit will not produce the same output as a filter wheel which fails to trip the home switch. A 10K resistor separates the 5V output from the homing switches. In the case of an accidental short, the resistor, located on the buffer board, helps limit the power that sinks into the dewar.

6.3.7 Adaptor Plates & Mounting Racks

Figures 6.25 through 6.30 display the different adaptor plates and mounting racks I designed for the WIRC camera. The designs accommodate dewar, Motor Con-

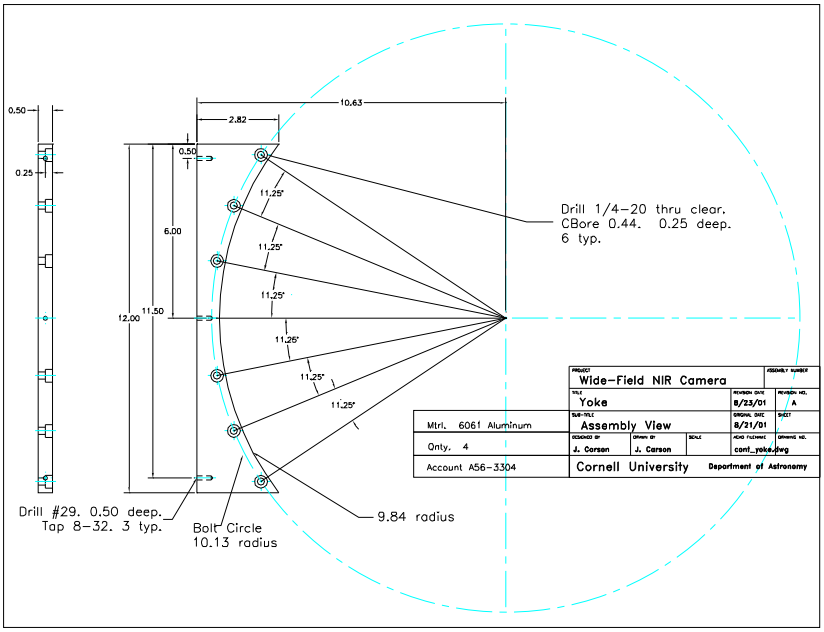

Figure 6.25: Dewar Support Yokes. These pieces provide a support interface between the dewar and the mounting racks.

troller Box, and PHARO Electronics Box bolt patterns while balancing the need to minimize weight and maximize durability. All machining was performed by Cornell University's Clarke Machine Shop.

6.3.8 Anti-Thermal Coatings

To minimize internal instrument reflections, we applied an infrared black paint to the inner surfaces of the aluminum lens barrel and the bottom and top surfaces of the filter wheels. Our painting procedure consisted of two major phases, a primer application and a black paint application. Below I list the procedures for making the two mixtures as well as the application process.

We made our primer from a mixture of the following ingredients:

- 5 parts Aeroglaze 9924A
- 5 parts Aeroglaze 9924B

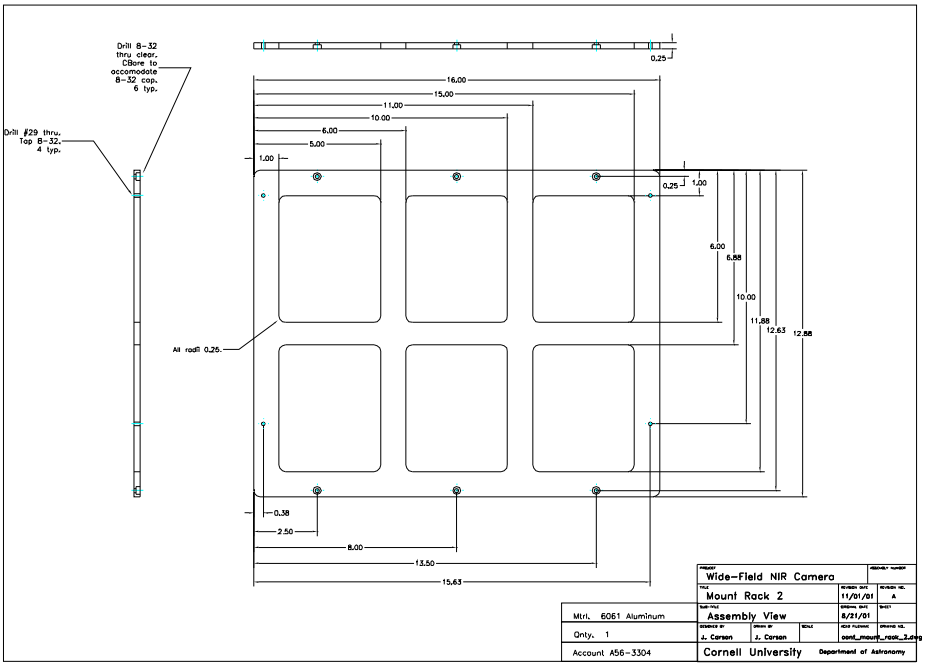

Figure 6.26: Motor Controller Box Support Rack. This piece provides the interface between the Dewar Support Yokes and the Motor Controller Box Adaptor Plate.

- 2 parts Aeroglaze 9958 Thinner

Underneath a fume hood, we measured 5 parts Aeroglaze 9924A in a clean beaker. Next we mixed in 1/3 of the Aeroglaze 9924B and continued mixing to ensure a uniform consistency. We added the remaining Aeroglaze 9924B in two additions, mixing thoroughly after each addition. Finally, we slowly mixed in the Aeroglaze 9958 Thinner to create a less viscous consistency, which eased the application process. After mixing thoroughly, we covered the mixing container to avoid reactions with the outside air.

We made our paint from a mixture of the following ingredients:

- 25 parts Z306 Black Paint
- 1 part Carbon Black, Acetylene Beads
- 2 parts Aeroglaze 9958 Thinner

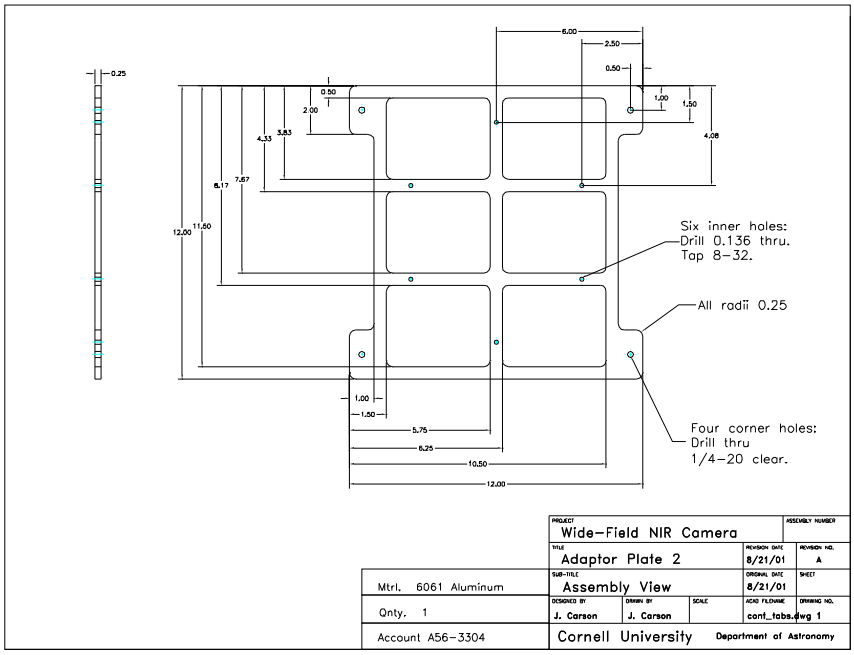

Figure 6.27: Motor Controller Box Adaptor Plate. This piece provides the interface between the Motor Controller Box Support Rack and the Motor Controller Box Supports.

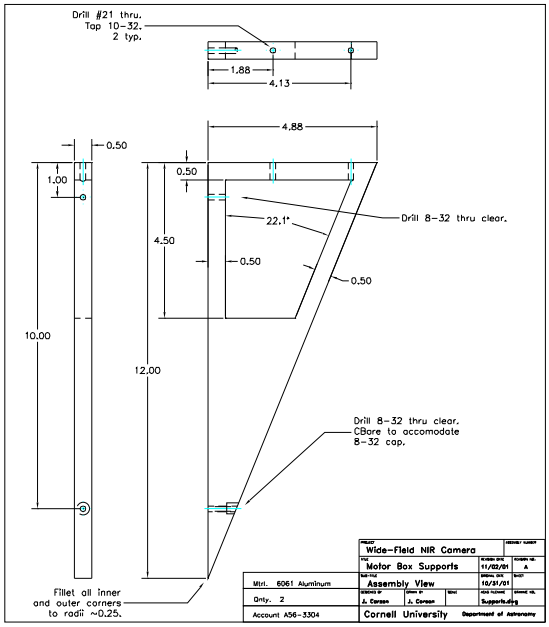

Figure 6.28: Motor Controller Box Supports. These pieces provide a support interface between the Motor Controller Box Adaptor Plate and the Motor Controller Box.

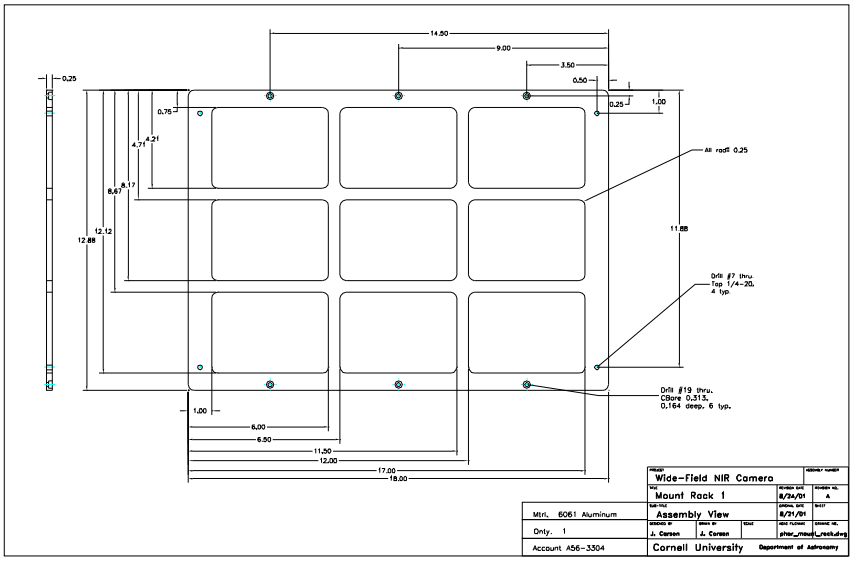

Figure 6.29: PHARO Electronics Box Support Rack. This piece provides the interface between the Dewar Support Yokes and the PHARO Electronics Box Adaptor Plate.

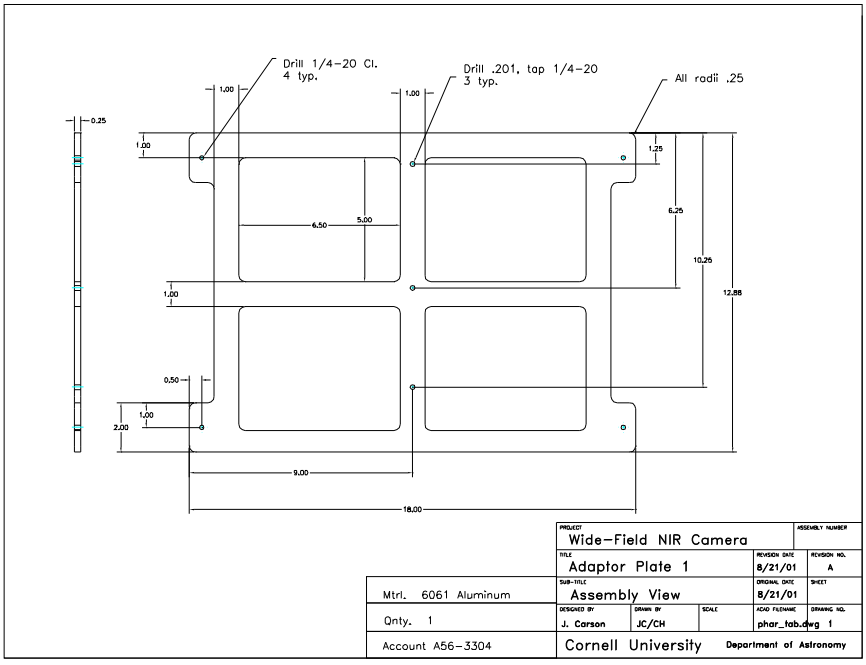

Figure 6.30: PHARO Electronics Box Adaptor Plate. This piece provides the interface between the PHARO Electronics Box Support Rack and the PHARO Electronics Box.

Underneath a fume hood, we measured out half of the Z306 Black Paint. We slowly added the Carbon Black, Acetylene Beads and continued mixing until we achieved a uniform consistency. Next we mixed in the rest of the Z306 Black Paint. Finally we mixed in the Aeroglaze 9958 Thinner to reduce the viscosity and ease the application process. Once completed, we covered the container to minimize contact with the air.

Before applying the primer, we gently scuffed all painting surfaces with a piece of Scotch Brite. Next we cleaned all of our scuffed surfaces with an acetone solution. After our acetone dried, we moved to a fume hood and applied a thin layer of primer using a clean paintbrush. We allowed the primer to dry underneath the fume hood for eight hours or more. Once the surfaces dried, we painted on a layer of our black paint. We allowed approximately four hours or more for the paint to dry underneath the fume hood. We repeated the painting process until we had three coats of black paint on every surface.

Bibliography

Albert, L., Doyon, R., & Nadeau, D. 2003, IAUS, 211, 287

Allard, F., Hauschildt, P. H., Baraffe, I., & Chabrier, G. 1996, ApJ, 465, L123

Allard, F., Hauschildt, P. H., Alexander, D. R., Starrfield, S. 1997, ARA&A, 35, 137

Basri, G., Marcy, G. W., & Graham, J. R. 1996, ApJ, 458, 600 Q

Basri, G. 2000, ARA&A, 38, 485

Bate, M. R., Bonnell, I. A., & Bromm, V. 2002, MNRAS, 332L, 65

Bergeron, P., Leggett, S. K., & Ruiz, M. T. 2001, ApJS, 133, 413

Becklin, E. E. & Zuckerman, B. 1988, Nature, 336, 656

Boss, A. P. 2001, ApJ, 551, 167

Bryja, C., Jones, T. J., Humphreys, R. M., Lawrence, G., Pennington, R. L., & Zumach, W. 1992, ApJ, 388, 23

Bryja, C., Humphreys, R. M., & Jones, T. J. 1994, AJ, 107, 246

Bucciarelli, B., Daou, D., Lattanzi, M. G., & Taff, L. G. 1996, VizieR On-line Data Catalog, 1176

Burgasser, A. J., et al. 1999, ApJ, 522, 65

———. 2000a, ApJ, 531, 57

———. 2000b, AJ, 120, 1100

Burgasser, A. 2002, Ph.D. thesis, Cal. Inst. Tech.

Burgasser, A. J. et al., 2002a, ApJ, 564, 421

———. 2002b, ApJ, 571L, 151

Burgasser, A. J., McElwain, M. W., & Kirkpatrick, D. J., 2003a, AJ, 126, 2487

Burgasser, A. J., Kirkpatrick, J. D., Reid, I. N., Brown, M. E., Miskey, C. L., & Gizis, J. E. 2003b, 586, 512

Burgasser, A. J., Kirkpatrick, J. D., McElwain, M. W., Cutri, R. M., Burgasser, A. J., & Skrutskie, M. F., 2003c, AJ, 125, 850

Burrows, A. & Liebert, J. 1993, Reviews of Modern Physics, 65, 301

Burrows, A., Hubbard, W. B., Lunine, J. I., & Liebert, J. 2001, Reviews of Modern Physics, 73, 719

Cayrel de Strobel, G., Soubiran, C., Friel, E. D., Ralite, N., & Francois, P., 1997, A&AS, 124, 299

Cayrel de Strobel, G., Soubiran, C., & Ralite, N., 2001, A&A, 373, 159

Chabrier, G., Baraffe, I., Allard, F., & Hauschildt, P. 2000, ApJ, 542, 119

Chabrier, G. 2001, ApJ, 554, 1274

Cuby, J. G., Saracco, P., Moorwood, A. F. M., D'Odorico, S., Lidman, C., Comerón, F., & Spyromilio, J. 1999, A&A, 349, L41

D'Antona, F. & Mazzitelli, I. 1994, ApJS, 90, 467

Dahn, C. C. et al., 2002, AJ, 124, 1170

De Jager, C. & Nieuwenhuijzen, H. 1987, A&A, 177, 217

Drilling, J. S. & Landolt, A. U. 2000, in Allen's Astrophysical Quantities, ed. A. N. Cox (New York: Springer-Verlag), 388

Duquennoy, A., & Mayor, M. 1991, A&A, 248, 485, 91

Els, S. G., Sterzik, M. F., Marchis, F., Pantin, E., Endl, M., & Kūrster, M. 2001, A&A, 370L, 1

Enoch, M. L., Brown, M. E., & Burgasser, A. J. 2003, AJ, 126, 1006

Epchtein, N., 1997, in The Impact of Large-Scale Near-IR Sky Surveys, ed. F. Garzon (Dordrecht: Kluwer), 15

Farihi, J., Becklin, E. E., & Zuckerman, B. 2003, IAUS, 211, 289

Fegley, B., Jr. & Lodders, K., 1996, ApJ, 472, 37

Fischer, D. A. & Marcy, G. W., 1992, ApJ, 396, 178

Geballe et al. 2002, ApJ, 564, 466

Gilmore, G. F. & Zeilik, M. 2000, in Allen's Astrophysical Quantities, ed. A. N. Cox (New York: Springer-Verlag), 489

Gizis, J. E., Kirkpatrick, J. D., Burgasser, A., Reid, I. N., Monet, D. G., Liebert, J., & Wilson, J. C. 2001a, ApJ, 551, 163

Gizis, J. E., Kirkpatrick, J. D., & Wilson, J. C. 2001b, AJ, 121, 2185

Gliese, W. & Jahreiss, H. 1995, VizieR On-line Data Catalog, 5070

Goldman, B. et al. 1999, A&A, 351, L5

Gunn, J. & Weinberg, D. 1995, WFSD Conf, 3

Hawarden, T. G., Leggett, S. K., Letawsky, M. B., Ballantyne, D. R., & Casali, M. M. 2001, MNRAS, 325, 563

Hayward, T. L., Brandl, B., Pirger, B., Blacken, C., Gull, G. E., Schoenwald, J, & Houck, J. 2001, PASP, 113, 105

Henry, T. J. & McCarthy, D. W., Jr. 1990, ApJ, 350, 334

———. 1992, ASP Conf. Ser., 32, 10

Hinz, J. L., McCarthy, D. W., Jr., Simons, D. A., Henry, T. J., Kirkpatrick, J. D., & McGuire, P. C. 2002, AJ, 123, 2027

Irwin et al. 1998, JGR, 10323001l

Itoh, Y. et al. 2003, IAUS, 211, 293

Jameson, R. F., Sherrington, M. R., & Giles, A. B. 1983, MNRAS, 205, 39

Jayawardhana, R., Mohanty, S., & Basri, G. 2002, ApJ, 578L, 141

———. 2003, ApJ, 592, 282

Jeffries, R. D., 1992, MNRAS, 288, 585

Kirkpatrick, J. D. et al. 1999, ApJ, 519, 802

Kirkpatrick, J. D., 2001, ASP Conf. Ser., 231, 17

Kirkpatrick, J. D., Dahn, C. C., Monet, D. G., Reid, I. N., Gizis, J. E., Liebert, J., & Burgasser, A. J. 2001, AJ, 121, 3235

Krasnopolsky, V. A., Bjoraker, G. L., Mumma, M. J., & Jennings, D. E. 1997, JGR, 102, 6525

Krishna Kumar, C. 1985, PASP, 97, 294

———. 1987, AJ, 94, 158

Kroupa, I., Tout, C., & Gilmore, G. 1993, MNRAS, 262, 545

Lançon, A. & Rocca-Volmerange, B. 1992, A&AS, 96, 593

Latham, D. W., Stefanik, R. P., Mazveh, T., Mayor, M, & Burki, G. 1989, Nature, 339, 38

Laustsen, S. 1996, VizieR On-line Data Catalog, 1099

Leggett, S. K. & Hawkins, M. R. S., 1988, MNRAS, 234, 1065

———. 1989, MNRAS, 238, 145

Leggett, S. K., Ruiz, M. R., & Bergeron, P., 1998, ApJ, 497, 294

Leggett, S. K. et al. 2000, ApJ, 536, 35

Leggett, S. K., Allard, F., Geballe, T. R., Hauschildt, P. H., & Schweitzer, A. 2001, ApJ, 548, 908

Leggett, S. K. et al., 2002, ApJ, 564, L452

Leinert, Ch., Weitzel, N., Richichi, A., Eckart, A., & Tacconi-Garman, L. E., 1994, A&A, 291, 47

Liu, M. C., Najita, J., & Tokunaga, A. T. 2003, ApJ, 585, 372

Low, C. & Lynden-Bell, D. 1976, MNRAS, 176, 367

Lowrance, P. J. 2003, IAUS, 211, 295

Macintosh, B., Zuckerman, B., Becklin, E., & McClean, I. S. 1996, Bull. Amer. Astron., 29, 730

Marcy, G. W. & Butler, R. P. 2000, PASP, 112, 137

Marois, C., Nadeau, D., Doyon, R., Racine, R., & Walker, G. A. H. 2003, IAUS, 211, 275

Martín, E. L., Barrado y Navascués, D., Baraffe, I., Bouy, H., & Dahm, S. 2003, ApJ, 594, 525

McCarthy, D. W., Jr., Probst, R. G., & Low, F. J. 1985, ApJ, 290L, 9

McCarthy, C. 2001, Ph.D. thesis, UCLA

McCarthy, C. & Zuckerman, B. 2004, AJ, 127, 2871

Mikami, T. & Ishida, K. 1981, PASJ, 33, 135

Monet, D. et al. 1998, A Catalogue of Astrometric Standards, USNO-A2.0, (U.S. Naval Observatory, Washington D.C.)

Muzerolle, J., Hillenbrand, L., Calvet, N., Briceño, C., & Hartmann, L. 2003, ApJ, 592, 266M

Nakajima, T., Oppenheimer, B. R., Kulkarni, S. R., Golimowski, D. A., Matthews, K., & Durrance, S. T., 1995, Nature, 378, 463

Noll, K. S. 1993, in Astronomical Infrared Spectroscopy, ed. S. Kwok (ASP Conf Series), 29

Noll, K. S., Geballe, T. R., Leggett, S. K., & Marley, M. S., 2000, ApJ, 541, 75

Ochsenbein, F. 1980, Bulletin D'Inf. Cent. Donnees Stellaires, 19, 74

Oppenheimer, B. R., Kulkarni, S. R., & Stauffer, J. R. 1999, in Protostars and Planets IV, ed. V. Mannings, A. Boss, & S. Russell (Tucson: University of Arizona Press), 1999

Oppenheimer, B. R., Dekany, R. G., Hayward, T. L., Brandl, B., Troy, M., & Bloemhof, E. E. 2000, SPIE, 4007, 899

Oppenheimer, B. R., Golimowski, D. A., Kulkarni, S. R., Matthews, K., Nakajima, T., Creech-Eakman, M., & Durrance, S. T. 2001, AJ, 121, 2189

Oswalt, T. D. et al. 1990, in Proc. 7th European Workshop on White Dwarfs, ed. G. Vauclair & E. Sion (NATO ASI Ser. C, 336)(Dordrecht: Kluwer), 379

Patience, J., Ghez, A. M., Reid, I. N., Weinberger, A. J., & Matthews, K. 1998, AJ, 115, 1972

Perryman, M. A. C. et al. 1997, A&A, 323, 49

Potter, D., Martín, E. L., Cushing, M. C., Baudoz, P., Brandner, W., Guyon, O., & Neuhāuser, R. 2002, ApJ, 567L, 133

Probst, R. G., & O'Connell, R. W. 1982, ApJ, 252L, 69

Probst, R. G. 1983a, ApJS, 53, 335

———. 1983b, ApJ, 274, 237

Rebolo, R., Martín, E. L., & Magazzú, A. 1992, ApJ, 389, 83

Rebolo, R., Zapatero Osorio, M. R., Madruga, S., Bejar, V. J. S, Arribas, S., & Licandro, J. 1998, Science, 282, 1309

Reid, I. N. & Gizis, J. E. 1997, AJ, 114, 1992

Reipurth, B. & Clarke, C. 2001, AJ, 122, 432

Renzini, A., et al. 1996, ApJ, 465, 23

Rocha-Pinto, H. J., Maciel, W. J., Scalo, J., & Flynn, C. 2000, A&A, 358, 850

Rosenthal, E. D., Gurwell, M. A., & Ho, P. T. P. 1996, Nature, 384, 243

Schaller, G., Schaerer, D., Meynet, G., & Maeder, A. 1992, A&AS, 96, 269

Schmidt-Kaler, Th. 1982, Landolt-Börnstein Numerical Data and Functional Relationships in Science and Technology, Group VI, Vol. 2b (New Series; Berlin: Springer-Verlag)

Scholz, R. D., McCaughrean, M. J., Lodieu, N., & Kuhlbrodt, B. 2003, A&A, 398L, 29

Shipman, H. L. 1986, in Astrophysics of Brown Dwarfs: Proceedings of the Workshop (Cambridge, England, and New York: Cambridge University Press), 71

Shu, F. H., Adams, F. C., & Lizano, S. 1987, ARA&A, 25, 23

Silvestri, N. M., Oswalt, T. D., Wood, M. A., Smith, J. A., Reid, I. N., & Sion, E. M. 2001, AJ 121, 503

Simons, D. A., Henry, T. J., & Kirkpatrick, J. D. 1996, AJ, 112, 2238

Simons, D. A. & Tokunaga, A. 2002, PASP, 114, 169

Skrutskie, M. F., Forrest, W. J., & Shure, M. 1989, AJ, 98, 1409

Skrutskie, M. F., et al. 1997, in The Impact of Large-Scale Near-IR Sky Surveys, ed. F. Garzon (Dordrecht: Kluwer), 25

Stahler, S. W. 1988, PASP, 100, 1474

Stauffer, J. R., Liebert, J., Giampapa, M., Macintosh, B., Reid, N., & Hamilton, D. 1994, AJ, 108, 160S

Strauss, M. A. et al. 1999, ApJ, 522, 61

Tokovinin, A. A. 1992, A&A, 256, 121

Tokunaga, A. T., 2000, in Allen's Astrophysical Quantities, Fourth Edition, ed. A. N. Cox (New York: Springer-Verlag)

Tokunaga, A. T., Simons, D. A., & Vacca, W. D. 2002, PASP, 114, 180

Troy et al. 2000, SPIE, 4007, 31

Tsuji, T., Ohnaka, K., Aoki, W., & Nakajima, T. 1996, A&A, 308, L29

Tsuji, T. 2001, in Ultracool Dwarfs: Surveys, Properties and Spectral Classification, ed. H. R. A. Jones & I. Steele, (Berlin Heidelberg: Springer-Verlag)

Tsuji, T. 2002, ApJ, 575, 264

Tsuji, T., & Nakajima, T. 2003, ApJ, 585L, 151

Tsvetanov, Z. I. et al. 2000, ApJ, 531, 61

van Altena, W. F., Lee, J. T., & Hoffleit, E. D. 2001, VizieR Online Data Catalog, 1238

Wilson, J. C., Kirkpatrick, J. D., Gizis, J. E., Skrutskie, M. F., Monet, D. G., & Houck, J. R. 2001, AJ, 122, 1989

Wilson, J. C. et al., 2003, SPIE, 4841, 451

Winglee, R. M., Dulk, G. A., & Bastian, T. S. 1986, ApJ, 309L, 59

Wood, M. A., 1992, ApJ, 386, 539

Zapatero Osorio, M. R., Béjar, J. S., Martín, E. L., Rebolo, R., Barrado y Navascués, D., Mundt, R., Eislöffel, J. & Caballero, J. A. 2002, ApJ, 578, 536

Zboril, M., Byrne, P. B., & Rolleston, W. R. J. R. 1997, MNRAS, 284, 685